

NONINVASIVE ASSESSMENT OF TUMOR HYPOXIA USING MRI IN
PRECLINICAL TUMOR MODELS AND PATIENTS

APPROVED BY SUPERVISORY COMMITTEE

Ralph P. Mason, Ph.D.

Roderick W. McColl, Ph.D.

Qing Yuan, Ph.D.

Dawen Zhao, M.D., Ph.D.

Robert D. Sims, M.D.

DEDICATION

This research project would not have been possible without the support of many people. To all of them, named or unnamed, I would like to express my gratitude and deepest appreciation.

First and foremost, I would like to thank my mentor and supervisor, Professor Ralph P. Mason for the invaluable guidance and advice. He serves as a mentor in knowledge, honor, patience, and kindness. Deepest gratitude is also due to the members of the supervisory committee, Dr. Qing Yuan, Dr. Robert Sims, Dr. Roderick McColl and Dr. Dawen Zhao for stimulating discussions and guidance.

I am indebted to every member of the Laboratory of Prognostic Radiology, especially Heling Zhou and Dr. Zhongwei Zhang, and staff members of the Radiology department who rendered their help during the period of my project work.

Lastly, and most importantly, I wish to avail myself of this opportunity, to express a sense of gratitude and love to my parents, brother Ramzi, his wife Tamara and daughter Celine, my sister Ranya, my uncles, my aunts, and cousins for their endless patience and encouragement when it was most required.

NONINVASIVE ASSESSMENT OF TUMOR HYPOXIA USING MRI IN
CLINICAL AND PRECLINICAL TUMOR MODELS

by

RAMI R. HALLAC

DISSERTATION

Presented to the Faculty of the Graduate School of Biomedical Sciences

The University of Texas Southwestern Medical Center at Dallas

In Partial Fulfillment of the Requirements

For the Degree of

DOCTOR OF PHILOSOPHY

The University of Texas Southwestern Medical Center at Dallas

Dallas, Texas

December, 2012

Copyright

by

RAMI R. HALLAC, 2012

All Rights Reserved

NONINVASIVE ASSESSMENT OF TUMOR HYPOXIA USING MRI IN
CLINICAL AND PRECLINICAL TUMOR MODELS

RAMI R. HALLAC, Ph.D.

The University of Texas Southwestern Medical Center at Dallas, 2012

Mentor: RALPH P. MASON, Ph.D.

Tumor oxygenation influences response to radiation and plays important roles in malignant progression, angiogenesis and metastasis. While methods are available to quantitatively map pO_2 dynamics in preclinical studies, new techniques are needed to noninvasively characterize tumor hypoxia and response to interventions in patients. Blood Oxygen Level Dependent (BOLD) MRI based on T_2^* contrast induced by deoxyhemoglobin concentration [dHb] is sensitive to tumor vascular oxygenation and blood flow. Meanwhile TOLD (Tissue Oxygen Level Dependent) MRI is sensitive to tissue oxygenation based on the shortening

of the tissue water T_1 due to molecular oxygen [O_2]. In this study, I investigate the utility of BOLD and TOLD to evaluate tumor hypoxia in response to breathing hyperoxic gas in rats and test the feasibility of such measurements in patients.

All MRI experiments were performed on either a 4.7T small animal Varian or a 3T clinical Philips scanner. Variation in BOLD and TOLD signal response observed in two syngeneic prostate tumor models: Dunning R3327-AT1 and -HI, with respect to oxygen and carbogen breathing were compared with quantitative change in pO_2 measured using Fluorocarbon Relaxometry using Echo Planar Imaging for Dynamic Oxygen Mapping (FREDOM). In addition, BOLD and TOLD MRI measurements were used to predict radiation treatment outcome following a single dose of 30 Gy. BOLD MRI was also assessed in cervical cancer patients in response to breathing oxygen ($15dm^3/min$). Two sequences were tested, multiple-shot EPI and multi echo gradient echo, to allow comparison.

Significant correlations were found between BOLD and TOLD MRI and quantitative pO_2 measurements for both oxygen and carbogen breathing. However, both gases had similar effect on modulating tumor hypoxia with no significant difference observed. The AT1 tumors showed a correlation between tumor growth delay for the animals breathing O_2 during radiation and pre-irradiation TOLD responses to oxygen challenge. Finally, BOLD MRI at 3T was feasible for examining the potentially valuable biomarker of oxygenation seen in cervical cancer. Further parameters such as vascular perfusion and permeability

based on DCE, cellularity based on diffusion, and TOLD response to oxygen challenge may also be readily incorporated into a dynamic evaluation.

TABLE OF CONTENTS

1	CHAPTER ONE Introduction	1
1.1	Tumor Biology	1
1.1.1	Characteristics of Tumor	1
1.1.2	Stage of Neoplasm.....	2
1.1.3	The Tumor and its Microenvironment.....	3
1.2	Tumor Hypoxia	5
1.2.1	Types of Tumor Hypoxia	5
1.2.2	The Role of Oxygen in Radiation Therapy	8
1.2.3	Methods for Assessing Tumor Hypoxia.....	11
1.3	Magnetic Resonance Imaging	13
1.3.1	Overview	13
1.3.2	NMR Relaxation.....	15
1.3.3	MRI Pulse Sequences and Image Contrast.....	16
1.3.4	Blood and Tissue Oxygen Level Dependent MRI.....	18
1.3.5	Dynamic Contrast Enhanced MRI.....	26
1.4	Perfluorocarbons	28
1.4.1	Background.....	28
1.4.2	Quantitative MR Oximetry Using PFCs.....	30

2	CHAPTER TWO Evaluating BOLD and TOLD Contrast MRI in Syngeneic Dunning Prostate Tumors	34
2.1	Abstract	34
2.2	Introduction	35
2.3	Materials and Methods	36
2.3.1	Animal Model.....	36
2.3.2	Tumor Oximetry	37
2.3.3	Data Analysis.....	39
2.3.4	Statistical Analysis	41
2.4	Results	41
2.5	Discussion	57
2.6	Conclusion.....	61
3	CHAPTER THREE Predicting Radiation Response Using Noninvasive ^1H Imaging	62
3.1	Abstract	62
3.2	Introduction	63
3.3	Methods.....	64
3.3.1	Oxygen Sensitive MRI	64
3.3.2	Dynamic Contrast Enhanced MRI (DCE).....	65
3.3.3	Radiation Treatment	65
3.3.4	Statistical Analysis	67

3.4	Results	67
3.5	Discussion	78
3.6	Conclusion.....	82
4	CHAPTER FOUR Oxygenation in Cervical Cancer and Normal Uterine Cervix Assessed Using BOLD MRI at 3 T.....	83
4.1	Abstract	83
4.2	Introduction	84
4.3	Experimental	85
4.3.1	Data Analysis.....	87
4.3.2	Statistical Analysis	88
4.4	Results	89
4.5	Discussion	98
4.6	Conclusion.....	104
5	CHAPTER FIVE: Extended Applications- Preliminary Studies of Oxygenation in Head and Neck, Lung, and Prostate Cancers Assessed Using BOLD MRI.....	108
5.1	Introduction	108
5.1.1	Head and Neck (H&N) Cancer.....	108
5.1.2	Non-Small Cell Lung Cancer (NSCLC).....	110
5.1.3	Prostate cancer	114
5.1.4	Conclusion.....	115

6	CHAPTER SIX Conclusions and Recommendations.....	117
	Bibliography	121

PRIOR PUBLICATIONS

- Hallac, R. R.**, Ding, Yao, Yuan, Qing, McColl, Roderick W., Lea, Jayanthi, Sims, Robert D., Weatherall, Paul T. & Mason, Ralph P. Oxygenation in cervical cancer and normal uterine cervix assessed using blood oxygenation level-dependent (BOLD) MRI at 3T. *NMR in Biomedicine*, doi:10.1002/nbm.2804, (2012).
- Kucejova, B., Sunny N. E., Nguyen A. D. , **Hallac R. R.**, Fu X. , Peña-Llopis S., Mason R. P., DeBerardinis R. J., Xie X-J. , DeBose-Boyd R., Kodibagkar V.D , Burgess S. C. & Brugarolas J. Uncoupling hypoxia signaling from oxygen sensing in the liver results in hypoketotic hypoglycemic death. *Oncogene* 30, 2147-2160, doi: 10.1038/onc.2010.587, (2011).
- Yu, J.-X., Kodibagkar, V. D., **Hallac, R. R.**, Liu, L. & Mason, R. P. Dual $^{19}\text{F}/^1\text{H}$ MR Gene Reporter Molecules for *in Vivo* Detection of β -Galactosidase. *Bioconjugate Chemistry* 23, 596-603, doi:10.1021/bc200647q (2012).
- Kodibagkar, V., **Hallac, R. R.**, Zhao, D., Yu, J.-X. & Mason, R. P. *^{19}F NMR: Clinical and Molecular Imaging Applications* Vol. 6. Chapter 12. Eds. V. Gouverneur & K. Muller World Scientific Publishing Company (World Scientific Publishing Company, London, 2012).
- Yu, J.-X., **Hallac, R. R.**, Chiguru, S. & Mason, R. P. New Frontiers and Developing Applications in ^{19}F NMR. *Progress in NMR Spectroscopy* (In Press).

CONFERENCE ABSTRACTS

Rami R. Hallac, Heling Zhou, Marisela Aguilera, Dawen Zhao, Vikram D. Kodibagkar, Ralph P. Mason. Evaluating BOLD and TOLD contrast MRI in tumors. World Molecular Imaging Congress (WMIC), San Diego, CA, 2011

Rami R. Hallac, Yao Ding, Qing Yuan, Roderick W. McColl, Jayanthi Lea, Robert D. Sims, Paul T. Weatherall, and Ralph P. Mason. Optimizing BOLD MRI for assessing oxygenation in cervical cancer. World Molecular Imaging Congress (WMIC), San Diego, CA, 2011

Rami R. Hallac, Yao Ding, Qing Yuan, Roderick W. McColl, Jayanthi Lea, Robert D. Sims, Paul T. Weatherall, and Ralph P. Mason. Oxygenation in Cervical Cancer and Normal Uterine Cervix assessed using BOLD MRI : Initial Experiences. The Society of Gynecologic Oncologists (SGO), Orlando, Florida, 2011.

Ralph. P. Mason, Dawen Zhao, Jesús Pacheco-Torres, **Rami Hallac**, Yao Ding, Qing Yuan, Vikram Kodibagkar, Kurt Parten, P. Peschke, Robert Sims, Jayanthi Lea, Debu Tripathy, Baran Sumer, Ganesh Raj, Robert Timmerman, and Paul Weatherall. DOCENT (Dynamic Oxygen

Challenge Evaluated by NMR T₁ and T₂*): a potential test to reveal tumor hypoxia. Cancer Prevention & Research Institute of Texas (CPRIT). Austin, TX, 2010

Ralph. P. Mason, Dawen Zhao, Jesús Pacheco-Torres, **Rami R. Hallac**, Yao Ding, Qing Yuan, Vikram D. Kodibagkar, Peter Peschke, R. Doug Sims, Jayanthi Lea, Ganesh Raj, Robert D. Timmerman, and Paul T. Weatherall. DOCENT (Dynamic Oxygen Challenge Evaluated by NMR T₁ and T₂*): applications from rats to diverse tumors in man". Radiation Research Society, Maui, HI. 2010

Rami R. Hallac, Yao Ding, Qing Yuan, Roderick W. McColl, Jayanthi Lea, Robert D. Sim, Paul T. Weatherall, and Ralph P. Mason. Oxygenation in Cervical Cancer and Normal Uterine Cervix assessed using BOLD MRI at 3 Tesla: Initial Experiences. International Society for Magnetic Resonance in Medicine (ISMRM), Stockholm, Sweden, 2010

Rami R. Hallac, Vikram D. Kodibagkar, Jian-Xin Yu, and Ralph P. Mason. Dual ¹H and ¹⁹F MR LacZ Gene Reporter Molecule Frontiers of biomedical imaging science, International Society for Magnetic Resonance in Medicine (ISMRM), Stockholm, Sweden, 2010

Qing Yuan, Yao Ding, **Rami R. Hallac**, Paul T. Weatherall, Robert D. Sim, Thomas Boike, Robert Timmerman, and Ralph P. Mason. Feasibility of BOLD Magnetic Resonance Imaging of Lung Tumors at 3T. International Society for Magnetic Resonance in Medicine (ISMRM), Stockholm, Sweden, 2010

Yao Ding, Robert P. Mason, Qing Yuan, **Rami R. Hallac**, Roderick W. McColl, Robert D. Sim, and Paul T. Weatherall. Interleaved T₁- and T₂*-weighted Imaging Can Evaluate Dynamic Oxygen Challenge: A Feasibility Study. International Society for Magnetic Resonance in Medicine (ISMRM), Stockholm, Sweden, 2010

Rami Hallac, C. D. Maroules, P. Khandheria, Yao Ding, Qing Yuan, Roderick W. McColl, Jayanthi Lea, Robert Sims, Paul Weatherall, and Ralph P. Mason. Oxygenation in Cervical Cancer and Normal Uterine Cervix assessed using BOLD MRI at 3 Tesla: Initial Experiences. Frontiers of Biomedical Imaging Science, Nashville, USA, 2009

LIST OF FIGURES

Figure 1-1 Scanning electron microscopic images of vascular casts.....	6
Figure 1-2 Diffusion related hypoxia.....	7
Figure 1-3 Direct and indirect action of radiation	10
Figure 1-4 Pulse sequence diagram (PSD)	20
Figure 1-5 Schematics showing the effect of a stimulus on R_2^* and R_1 contrast imaging.....	21
Figure 1-6 <i>In Vitro</i> studies showing the relation between blood saturation level, pO_2 and R_2^* contrast	22
Figure 1-7 Effect of TE on changes in SI in T_2^* W images during an oxygen challenge.....	24
Figure 1-8 Accumulation of short acylcarnitines and inhibition of oxygen consumption in <i>Vhl</i> -deficient livers.....	32
Figure 1-9 FREDOM technique.....	33
Figure 2-1 Automated acquisition of interleaved BOLD and TOLD.....	39
Figure 2-2 Oxygen sensitive MRI.....	44
Figure 2-3 Oxygen dynamics assessed by MRI.....	45
Figure 2-4 Correlation between BOLD, TOLD, and pO_2 for 9 AT1 tumors.	48
Figure 2-5 Comparison of response to oxygen and carbogen for 9 AT1 tumors.	49

Figure 2-6 Comparison of hypoxic fraction residual to oxygen and carbogen for 9 AT1 tumors.....	50
Figure 2-7 Correlations between responses of individual voxels in ¹⁹ F MRI oximetry maps of a single tumor	50
Figure 2-8 Changes in tumor oxygenation in response to oxygen breathing.	52
Figure 2-9 Correlations between pO ₂ responses of individual voxels in ¹⁹ F MRI oximetry maps of a single AT1 tumor	53
Figure 2-10 Tumor oximetry using ¹⁹ F MRI.	54
Figure 2-11 Histogram comparing ΔT_2^* and FREDOM	55
Figure 3-1 Raw T ₂ *W images and fitting quality	69
Figure 3-2 Raw T ₁ W images and fitting quality.....	70
Figure 3-3 Oxygen sensitive MRI.....	71
Figure 3-4 Oxygen sensitive MRI.....	72
Figure 3-5 Influence of radiation on Dunning prostate R3327-AT1 tumor growth.....	73
Figure 3-6 Tumor growth delay for 13 AT1 tumors.....	74
Figure 3-7 Tumor volume quadrupling time (T ₄).	76
Figure 3-8 Influence of radiation on Dunning prostate R3327-HI tumor growth.....	77
Figure 3-9 Tumor volume quadrupling time (T ₄) for AT1 tumors.....	78

Figure 4-1 Blood oxygen level-dependent (BOLD) MRI of cervical tumor in the axial plane.....	91
Figure 4-2 Sagittal imaging in a healthy volunteer with respect to oxygen challenge.	92
Figure 4-3 Changes in R_2^* in a healthy volunteer.	94
Figure 4-4 BOLD response to oxygen challenge based on changes in signal intensity (SI) and R_2^*	95
Figure 4-5 Comparison of semi-quantitative and quantitative BOLD response measurements.....	97
Figure 5-1 H&N cancer patient.....	110
Figure 5-2 MRI of patient with large lung tumor	113
Figure 5-3 BOLD kinetics in lung tumor from the same patient in Figure 1.	113
Figure 5-4 T_2^* maps of tumor ROI.....	114
Figure 5-5 Quantitative BOLD in human prostate cancer with a Gleason score 9.	116

LIST OF TABLES

Table 1-1 Human tissue values for the time constants T_1 and T_2 at field strengths of 1.5T and 3T [43]	16
Table 2-1 Transverse relaxation rates and pO_2 of Dunning prostate R3327-AT1 tumors	56
Table 2-2 Transverse relaxation rates and pO_2 of Dunning prostate R3327-HI tumors	56
Table 2-3 Effect of oxygen breathing on BOLD and TOLD MRI of Dunning prostate R3327-AT1 tumors.	57
Table 4-1 BOLD response of cervical tumor, uterus, and iliacus muscle observed in EPI images based on T_2^* -weighted signal response to breathing oxygen.....	106
Table 4-2 BOLD response of cervical tumor, normal cervix, and uterus observed in the sagittal GRE images based on R_2^* and T_2^* -weighted signal response to breathing oxygen	107

LIST OF ABBREVIATIONS

BOLD – Blood Oxygen Level Dependent

CB – Carbogen

DCE – Dynamic Contrast Enhanced

dHbO₂ – Deoxyhemoglobin

EPI – Echo Planar Imaging

EPR – Electron Paramagnetic Resonance

FFE – Fast Field Echo

fMRI – Functional Magnetic Resonance Imaging

FREDOM – Fluorocarbon Relaxometry Using Echo Planar Imaging for Dynamic .

Oxygen Mapping

FSEMS – Fast Spin Echo Multi Slice

HbO₂ – Oxyhemoglobin

HF – Hypoxic Fraction

HFB – Hexafluorobenzene

IAUC – Initial Area under the Curve

IBT– Interleaved BOLD and TOLD

k^{trans} – Blood Perfusion-Vessel Permeability

MGEMS – Multi Gradient Echo Multi Slice

MRI – Magnetic Resonance Imaging

OMRI – Overhauser Magnetic Resonance Imaging

PFC – Perfluorocarbon

pO_2 – Partial Pressure of Oxygen

ROI – Region of Interest

SEMS – Spin Echo Multi Slice

SI – Signal Intensity

T_1 – Spin-Lattice Relaxation

T_2 – Spin-Spin Relaxation

T_2^* – Apparent Spin-Spin Relaxation

T4 – Time to Quadruple in Volume

TE – Echo Time

TME – Tumor Microenvironment

TOI – Tissue of Interest

TOLD – Tissue Level Dependent

TR – Repetition Time

v_e – Extravascular-Extracellular Volume Fraction

Vhl – von Hippel-Lindau

CHAPTER ONE

Introduction

1.1 TUMOR BIOLOGY

1.1.1 Characteristics of Tumor

Cancer remains a serious disease resulting in premature death in a significant number of patients who present at advanced stages. It is a complex family of diseases that alter normal cells into malignant neoplasm or cancer. These “diseased” cells are characterized by rapid and uncontrolled proliferation caused by multiple changes in gene expression, which leads to either solid or dispersed tumor formation [1, 2].

The term “neoplasm”, meaning new growth, has been generally used to describe “tumor” to indicate a cancerous growth. However, it is important to point out that tumors can be of two types: benign and malignant. Identifying these two types of tumors is crucial in determining the treatment and prognosis of a patient. Below are the features of both tumors [2]:

- Benign tumors are often harmless. They are characterized by slow, encapsulated and localized growth. They generally do not spread to other

parts of the body or invade other tissues. They are often treated surgically and have low recurrence rate.

- Malignant tumors, on the other hand, are more aggressive and highly proliferative. They invade and destroy adjacent normal tissue. Under certain circumstances, such as stress, they metastasize through the blood stream and lymphatic channels to other organs. Malignant tumors are less well differentiated (anaplastic) than normal tissue in which they arise. Individual or combined treatment plans, such as radiation, chemotherapy and/or surgical procedures, are often used to control malignant tumor growth; however, prognosis is often poor at advanced stages.

1.1.2 Stage of Neoplasm

Tumor staging helps oncologists in planning the treatment course and in determining the patient's prognosis. Two major agencies, the Union for International Cancer Control (UICC) and the American Joint Committee for Cancer Staging and End Results Reporting (AJCCS), help in standardizing this technique worldwide. Both agencies follow the TNM (Tumor, Node, and Metastasis) staging system, where T1, T2, T3, T4 represent the size and/or extent of the primary tumor, N0, N1, N2, N3 represent the number of involved regional lymph nodes, M0 and M+ indicate whether or not distant metastasis is present.

1.1.3 The Tumor and its Microenvironment

Tumor growth and progression is not only supported by the tumor itself, but also by its surrounding microenvironment: the normal cells and molecules that surround tumor cells. Studying the tumor microenvironment (TME) helps expand our understanding of the tumor development.

The TME consists of normal epithelial cells (not cancerous yet), fibroblasts that help to maintain the structural integrity of connective tissues, infiltrating immune cells migrating from the blood stream, and the extracellular matrix that consists of structural components comprised of proteins that hold the cells together. In addition, molecules, such as chemokines and cytokines, are chemical activators and cellular activators make up the TME.

Hanahan and Weinberg defined ten hallmarks of cancer that enable tumor proliferation and invasion [2, 3]. These hallmarks involve cell autonomous genetic and metabolic alterations. Most cancer cells develop these functional capabilities during their development [4]. Two of the key hallmarks of cancer depend on the surrounding TME: inducing angiogenesis and activating invasion and metastasis.

In order for the tumor to sustain sufficient oxygen and nutrition, a rapid proliferation of tumor-associated neovascularization is generated by the angiogenic process. In fact, tumors cannot sustain growth beyond 1mm in diameter without

angiogenesis [5]. These biochemical signals have been seen as important biomarkers for tumor therapy [6]. For example, the vascular endothelial growth factor (VEGF) is a signal protein made by the tumor cells to stimulate angiogenesis. Several drugs have been successfully developed to target the VEGF receptors in order to inhibit and block their activity. Several of these drugs, such as Avastin (Bevacizumab), have shown great promise in the treatment of colon cancer.

Delivering chemotherapeutic drugs to the tumor is hindered by the abnormal/immature vasculature of the tumor, which is caused by the rapid vascular proliferation. These abnormal vessels are characterized by increased permeability, vessel diameter and length, resulting mainly from incomplete endothelium and lack of pericytes [7]. In addition, the lack of lymphatic vessels increases the interstitial pressure causing the tumor blood vessels to collapse, thus reducing the blood supply and preventing efficient drug delivery.

The abnormal vasculature and high interstitial fluid pressure lead to an impaired oxygen supply to tumor cells. This reduction in supply compounded by the increase in consumption leads to hypoxic (partial pressure of oxygen (pO_2) < 10 mmHg) regions in tumors.

1.2 Tumor Hypoxia

1.2.1 Types of Tumor Hypoxia

Tumor has to go through several metabolic alterations to adapt to its microenvironment. One of the most important alterations is the adaptation to hypoxia (low oxygenation). Tumors, as other normal tissues, require oxygen and nutrients to sustain cell growth. However, due to the rapid and uncontrolled tumor proliferation, the oxygen consumption rate may exceed the oxygen supply, causing hypoxia [1, 4]. This, in turn, alters the tumor progression by inducing angiogenesis and elevated glucose uptake. There are three types of hypoxia: acute, chronic and anemic hypoxia. Each is caused by several factors, which are mainly related to perfusion, diffusion, or anemia as described in detail below [8].

Perfusion related (acute) hypoxia is caused by insufficient blood flow to the tissue. The tumor microvasculature often has severe structural and functional abnormalities as a result of rapid proliferation due to angiogenesis. These abnormalities include disorganized vascular network (Figure 1.1), incomplete endothelial lining, elongated and tortuous shape, dilations, and absence of flow regulators. These combined cause low intravasculature pressure, which prevent the blood whether oxygenated or not, from reaching the tumor. This causes perfusion related hypoxia that leads to ischemic hypoxia, which is transient [9].

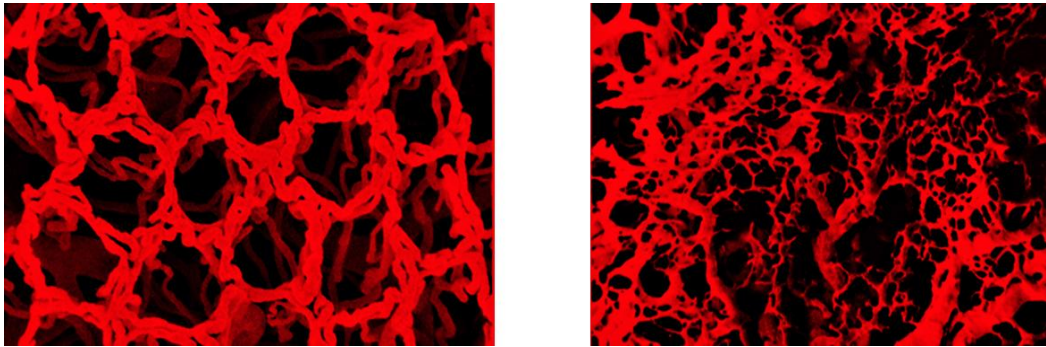


Figure 1-1 Scanning electron microscopic images of vascular casts. (A) Organized vasculature network in normal ascending colon compared to a disorganized vasculature in an adjacent colonic carcinoma (B). Figure modified from [10].

Diffusion related (chronic) hypoxia is a result of the increased diffusion distance between the blood supply and tissue. This occurs due to the rapid uncontrolled tumor proliferation, which exceeds blood supply of oxygen and nutrition. Cells that are more than 70 μ m away from the nutritive blood vessels have an inadequate oxygen supply (Figure 1.2) [9]. In addition, diffusion geometry (concurrent versus countercurrent blood flow within the tumor microvessel network), and declining oxygen tension due to leaky vasculature exacerbate this effect [8, 9].

Anemic hypoxia is caused by reduced oxygen transport capacity. Several studies indicate that the oxygen transport capacity to tumor is greatly reduced. A hemoglobin level below normal (10-12 g/dl) for the subject can contribute to tumor hypoxia. This effect is intensified especially when anemic hypoxia coincides with low perfusion rate [9, 11].

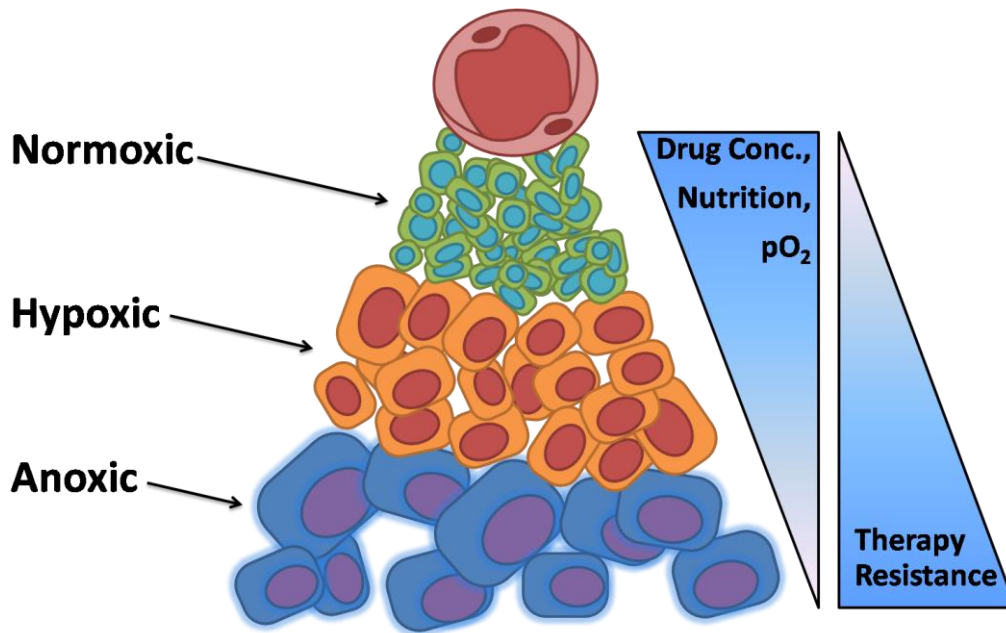


Figure 1-2 Diffusion related hypoxia. Cells in the inner core are cut off from vascular sources.

Tumor cells adapt to survive and grow under a hypoxic condition by a transcription factor, HIF1 α . In normoxic tissues, HIF1 α is continuously degraded. In a tumor cell, HIF1 α has a modified receptor that can bind to the von Hippel-Lindau (VHL), a tumor suppression factor which prevents its degradation. Under hypoxic conditions, HIF1 α is further modified to bind to specific hypoxic response elements. The end result of this modulation is stimulating the increased expression of VEGF and erythropoietin [12].

Hypoxic tumors are known to be more aggressive, resistant to radiation and some chemotherapy drugs, and have higher incidence of distant metastasis [1, 13,

14]. Therefore, assessment of tissue oxygen tension (pO_2) in the tumor microenvironment and the ability to image it *in vivo* could provide useful prognostic information.

1.2.2 The Role of Oxygen in Radiation Therapy

Radiation is a commonly used method for tumor therapy. It involves different types of high energy radiation, such as X-rays, γ -rays, or charged particles. These high energy photons or particles penetrate through the tissue and cause damage to the DNA, which is the critical target in the tumor. If the cell cannot repair the DNA damage, then the tumor shrinks and dies [11].

Radiation can be classified as directly or indirectly ionizing. If the radiation is absorbed by the biologic material, the atoms of this material will be ionized causing a biological change. This process of radiation interaction with tissue is called direct ionization (Figure 1.3). It is more dominant in radiation with high linear energy transfer (LET) such as particles. In the case of indirect ionization, a free radical is produced by interaction of radiation with other atoms or molecules in the cell (mainly water). This free radical then travels to reach the critical target causing damage as illustrated in Figure 1.3. Indirect ionization is more dominant in radiation with low LET such as x-ray [11, 15].

During the indirect ionization, the x -ray or γ -ray photon interacts with water producing an ion radical ($H_2O \xrightarrow{IR} H_2O^+ + e^-$). This ion radical will soon encounter another water molecule to form a hydroxyl radical (OH^\bullet), which is highly reactive. This hydroxyl radical may then react with the DNA to cause biological damage by breaking its double strand. The bound radical has a short half life of 10^{-5} sec [16]. Oxygen plays an important role in this step to cause permanent DNA damage. If the tumor lacks oxygen molecules, as in the case of hypoxia, the cell can repair the DNA damage preventing effective radiation treatment [11]. The ratio of hypoxic to aerated doses needed to achieve the same biological effect is called the oxygen enhancement ratio (OER).

Hypoxia is increasingly regarded as an important factor and potential prognostic biomarker for tumor progression [4], malignancy [17], and response to therapy [18, 19]. In addition, hypoxia has been regarded as a physiological stimulus for anti cancer drug activation [20] or hypoxia-regulated gene therapy [21]. There have been many attempts to assess tumor hypoxia and alter the tumor hypoxia prior to radiation or chemotherapy to enhance therapeutic efficacy. Therefore, assessment of tumor hypoxia and the ability to perform *in vivo* imaging can provide useful prognostic information.

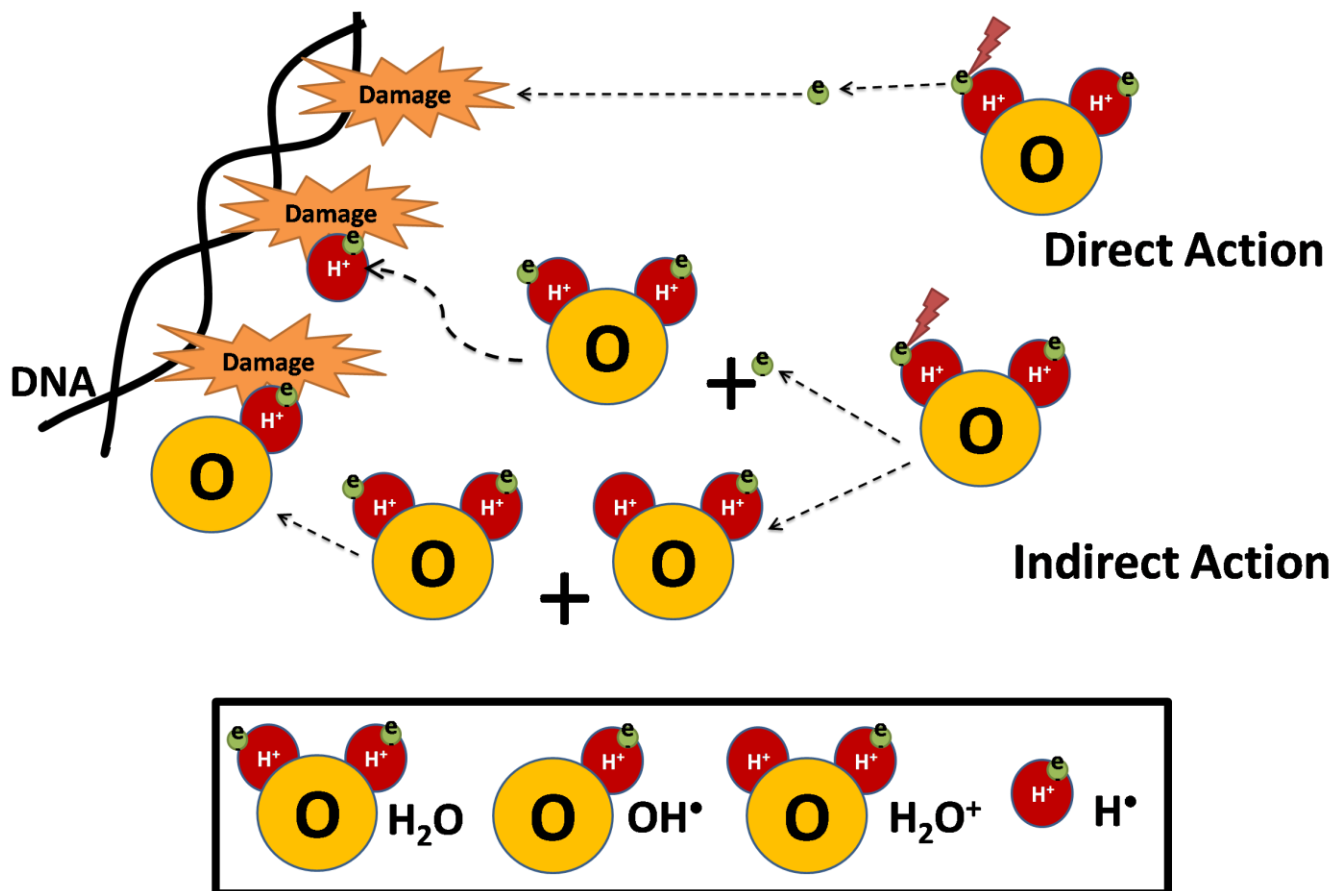


Figure 1-3 Direct and indirect action of radiation. Direct action: DNA damage is caused by a secondary electron (from absorption of an x-ray photon) interaction with DNA. Indirect action: damaged caused to DNA by the hydroxyl radical (OH[•]) or other highly reactive radicals.

1.2.3 Methods for Assessing Tumor Hypoxia

The present “gold standard” technique is the intratumoral polarographic measurement of pO_2 . Several studies using invasive needle electrodes for various disease sites have shown that tumor hypoxia is associated with poor prognosis, notably for head and neck cancer, prostate, lung, and breast [22-24]. In addition, Positron Emission Tomography (PET) contrast agents, such as [^{18}F]fluoromisonidazole, 3-fluoro-1-(2'-nitro-1'-imidazolyl)-2-propanol or (^{18}F -MISO) [25, 26], have been used to detect tumor hypoxia. Studies showed correlation between ^{18}F -MISO uptake and therapy outcome [27]. However, these techniques are not widely available and expensive [28].

Many diverse MR approaches have been demonstrated for the assessment of tumor oxygenation and hypoxia based on NMR (Nuclear Magnetic Resonance), EPR (Electron Paramagnetic Resonance) or hybrid OMRI (Overhauser Magnetic Resonance Imaging) [29]. While these methods often provide quantitative measurements of pO_2 , they require administration of reporter molecules and are largely restricted to pre-clinical investigations. In fact, several ^{19}F and 1H MR oximetry methods have been developed for pre-clinical studies based on perfluorocarbon (discussed later) and siloxane reporter molecules [19, 28, 30, 31]. A number of studies have demonstrated changes in regional pO_2 accompanying hyperoxic gas breathing and administration of vasoactive drugs [32]. However,

application of the highly hydrophobic reporter molecules would be difficult in patients. It has been reported that emulsions suitable for systemic delivery tend to accumulate in the liver and spleen and well vascularized regions of tumor [30], while direct intratumoral injection is invasive [33]. Fluoronitroimidazoles have been detected in tumors by ^{19}F MRI following systemic delivery and uptake has been correlated with hypoxia [34, 35]. Indeed, a 2-nitroimidazole agent designed as a noninvasive probe of tumor hypoxia, known as SR4554, was examined in a clinical trial [36]. However, the signal to noise ratio was generally poor, limiting studies to spectroscopy. In addition, ^{19}F detection capabilities remain esoteric on human clinical MRI scanners.

Noninvasive methods, low radiation exposure, resolution and availability are still particularly attractive. Oxygen sensitive proton MRI of the natural water signal is an attractive approach for evaluating tumor hypoxia [19]. In this regard, proton MRI exploiting BOLD (Blood Oxygen Level Dependent) contrast has attracted increasing interest as a non-invasive indicator of hypoxia based on intrinsic effective transverse relaxation rate (R_2^*) or response to breathing hyperoxic gas (ΔSI or ΔR_2^*) [37]. Paramagnetic deoxyhemoglobin in blood induces transverse relaxation [38, 39] exploited widely to assess neuronal activation. It has been suggested that a fast R_2^* may be directly indicative of tumor hypoxia (extensive deoxyhemoglobin) [40].

1.3 MAGNETIC RESONANCE IMAGING

1.3.1 Overview

Magnetic Resonance Imaging (MRI) is an imaging modality that is widely used in the clinic to visualize internal structure of the body. It uses the nuclear spin property of nuclear magnetic resonance (NMR) to image nuclei of atoms, mainly ^1H , inside the body. The fundamental discovery of the Nobel laureates Felix Block and Edward Purcell found that certain nuclei absorb energy in the radiofrequency range of the electromagnetic spectrum when placed in a magnetic field and reemit the energy when transferred to the original state. In the late 1960s, Damadian hypothesized that tissue had different NMR properties and found that cancerous tissue had longer relaxation times than normal tissue. However, the MR imaging was not feasible until Paul Lauterbur invented the idea of measuring the frequency and phase shifts by inducing spatial gradients (G) [41].

MRI consists of three important components: superconducting magnet, radiofrequency coils and gradient coils. The superconducting magnets are made of metal alloys that have no resistance to electricity at extremely low temperature. These superconducting coils are immersed in cryogen (liquid helium) to reduce wire resistance. Therefore, strong magnetic field can be generated with minimal

electric power when temperature approaches absolute zero. These magnets are designed with very uniform field to reduce the body position and magnet dependence. This can be achieved by using a Helmholtz coil, which is a pair of circular wire loops that are separated by a distance that equals the radius, or long solenoids. Another important factor of a superconducting magnet is the field strength (B_0). The field strength of current MRI scanners ranges from 0.5 Tesla (T) to 20T (1T to 9T for human scanners) [41, 42].

The MR signal is generated by radiofrequency (RF) coils, which consist of the transmitter and receiver coils. These coils have to match the resonance frequency of the imaged nuclei. Therefore, they are designed with tunable capacitors to allow the RF coils to be tuned and matched to a resonance frequency. Several types of coil may be designed for specific applications. Surface coils are characterized with high signal sensitivity. However, they have low global coverage and poor spatial homogeneity. On the other hand, birdcage/volume coils and solenoid coils have better field homogeneity but are less sensitive. A new class of RF coils consists of overlapping surface coils. These, so called phased arrays, improve the surface coverage while maintaining good sensitivity [41].

The signal (current) that is obtained in the RF receiver coils has no inherent spatial localization information and it is not feasible to reconstruct an image. However, spatial localization can be generated by applying a magnetic gradient,

generated by the gradient coils, in three orthogonal planes. Therefore, a spatial identity can be generated, which is later resolved by the Fourier Transform.

1.3.2 NMR Relaxation

Placing a water sample into a magnetic field, B_0 , causes the nuclear spins to precess about B_0 along the field direction. Applying an electromagnetic pulse (excitation pulse) causes the nuclear spins to change from low to high energy state. After this short excitation pulse, the spins will spontaneously return to the low energy (i.e. equilibrium). During the period of free precession, the magnetization returns to its original equilibrium state by a process called relaxation. During this relaxation process, RF energy is emitted, which can be detected by the RF coil.

The relaxation can be characterized by two processes: the spin-lattice relaxation (longitudinal, T_1) and the spin-spin relaxation (transverse, T_2). Macroscopically, T_1 relaxation is described by the return of the longitudinal magnetization to its ground state (i.e, low energy), whereas T_2 relaxation is the decay of the transverse magnetization when high and low energy states exchange energy, but do not lose energy to the surrounding lattice. T_1 and T_2 are inherent properties of molecules and tissues, whereas T_2^* depends also on inhomogeneities

in the magnetic field. Examples of T_1 and T_2 relaxation times are given in Table 1.1 [41, 42].

Table 1-1 Human tissue values for the time constants T_1 and T_2 at field strengths of 1.5T and 3T [43]

<i>Tissue</i>	<i>1.5T</i>		<i>3T</i>	
	T_1(ms)	T_2(ms)	T_1(ms)	T_2(ms)
Skeletal muscle	1060	35	1420	32
Liver	576	46	812	42
White matter	778	79	1110	56
Gray matter	1086	85	1470	71
Blood	1441	290	1932	275

1.3.3 MRI Pulse Sequences and Image Contrast

An MR pulse sequence is a series of events that consists of RF pulses, gradient waveforms, and data acquisition. The main purpose of the pulse sequence is to manipulate the magnetization in order to produce a desired signal. There are many basic and advanced MRI sequences. In this section, I will focus only on two basic sequences which are later used in my studies: spoiled gradient echo and spin echo sequences.

- **Spoiled Gradient Echo Sequence**

Gradient echo (GRE) sequence consists of only one excitation pulse. It tilts the magnetization by a flip angle (α) that can range from 0° to 90° . If the transverse magnetization is assumed to be zero just before each excitation pulse, then the GRE pulse sequence is said to be spoiled. If, however, the transverse magnetization reaches a (nonzero) steady state just before the application of each excitation pulse, then the pulse sequence is said to produce steady-state free precession (SSFP). As shown in Figure 1.4A, the gradient echo sequence uses gradient reversal on the frequency-encoded axis to form an echo. First, a readout prephasing gradient lobe dephases the spin isochromats, and then they are rephased with a readout gradient that has an opposite polarity. The spoiled gradient echo signal intensity can be described as [42]:

$$S = \frac{M_0 \sin \theta (1 - e^{-TR/T_1})}{1 - \cos \theta e^{-\frac{TR}{T_1}}} e^{-TE/T_2^*} \quad \text{Equation 1.1}$$

Where M_0 is proton density, TR is repetition time, TE is echo time, θ is flip angle.

The image contrast can be determined by varying the TR, TE and flip angle.

- **Spin Echo Sequence**

The standard spin echo sequence consists of two RF pulses, one 90° to excite the magnetization and one 180° to refocus the spins to generate the signal echo (Figure 1.4B). The spin echo sequence has been developed into many other variants such as fast spin echo sequence. The contrast that can be generated from

the spin echo sequence is a T_1W image (short TR and short TE) and T_2W images (long TR and long TE). Because of the refocusing 180° pulse, T_2^*W images cannot be generated using a spin echo sequence [42].

1.3.4 Blood and Tissue Oxygen Level Dependent MRI

Under normal physiological conditions, oxygen (O_2) is carried in the blood from lung to tissues either combined with hemoglobin (98.5% of all oxygen in the blood), or dissolved in the blood plasma (1.5%). Due to the paramagnetic properties of both deoxyhemoglobin (dHb) and dissolved oxygen and the diamagnetic property of oxygenated hemoglobin (Hb), blood has been used as an endogenous agent to evaluate oxygenation noninvasively using MRI. The paramagnetic dHb has a strong effect on T_2^* relaxation and a weaker effect on T_1 . The dissolved oxygen in plasma plays a negligible role in oxygen transport under physiological conditions, but the T_1 -shortening effect of molecular oxygen or dissolved oxygen in tissue provides a mechanism for monitoring tissue oxygenation status during hyperoxic or hyperbaric gas challenge. Therefore, quantitative MRI measurements of T_1 and T_2^* relaxation times offer a noninvasive means to evaluate tissue oxygenation.

In the early 1990s, Ogawa and colleagues noticed that BOLD MRI contrast can be a useful technique for functional brain mapping. BOLD signal relies on the

change in the magnetic properties of hemoglobin when it converts between the oxygenated and the deoxygenated forms, which in turn influences the magnetic properties of neighboring water molecules to change signal intensity [38, 39].

BOLD imaging has attracted increasing interest as a non-invasive indicator of hypoxia because of its high sensitivity, high spatial and temporal resolution easy implementation and lack of exogenous reporters. The changes in tumor BOLD-MRI are based on intrinsic effective transverse relaxation rate (R_2^* , $1/T_2^*$) or response to breathing hyperoxic gas (ΔSI or ΔR_2^*), which was first demonstrated by the pioneering studies of the groups of Karczmar and Griffiths [44, 45]. It has been suggested that a large R_2^* value may be directly indicative of tumor hypoxia (extensive deoxyhemoglobin). However, R_2^* is also highly dependent on vascular structure or extent [46, 47], local hematocrit, hemorrhage, calcification, and iron deposition in tissue as well as B_0 field inhomogeneity at tissue interfaces [48, 49]. In addition, changes in blood flow (BF) and blood volume (BV) can affect the changes in R_2^* , as illustrated in Figure 1.5.

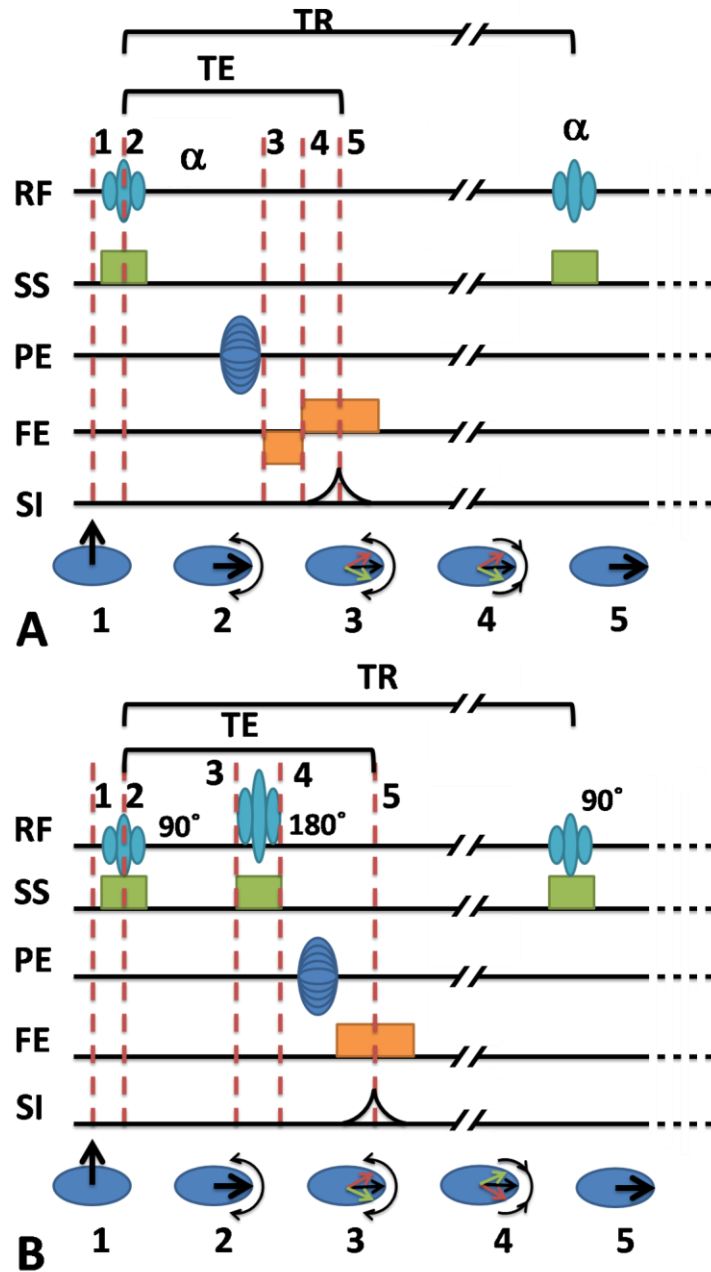


Figure 1-4 Pulse sequence diagram (PSD). A timing diagram of (A) gradient echo sequence and (B) spin echo sequence showing the different RF pulses, gradients, and spins. (RF: radiofrequency; SS: slice selection; PE: phase encoding; FE: frequency encoding; SI: signal intensity)

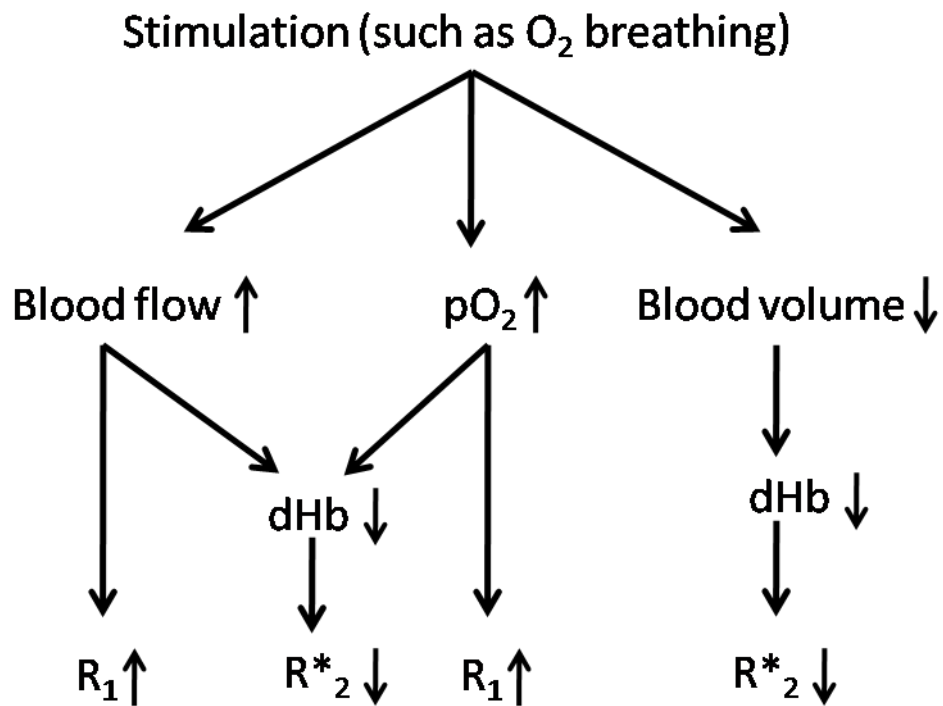


Figure 1-5 Schematics showing the effect of a stimulus on R_2^* and R_1 contrast imaging. Breathing oxygen can cause several physiological changes that can be detected by MRI. Here is an example of changes on blood flow, blood volume and pO_2 and their effect on R_1 and R_2^* contrast.

Response to a hyperoxic gas breathing challenge provides further insight into tumor vascular oxygenation as revealed by changes in R_2^* , local linewidth or contrast in T_2^* -weighted images [46, 47, 50-54]. In fact, most human cancer studies have employed a hyperoxic gas breathing challenge to induce BOLD contrast, as demonstrated in diverse [37] or specific disease sites, such as prostate [55-57], head and neck [58], brain [59, 60] or breast [61]. Multiple preclinical studies have explored response to interventions and sometimes compared BOLD

contrast with pO_2 measurements [46, 47, 51-55, 62-70]. A recent report showed that a large BOLD response ($\Delta SI > 3\%$) in the 13762NF rat breast tumor corresponded with elimination of tumor hypoxia ($HF_{10} < 5\%$; HF_{10} is the fraction of tumor with pO_2 less than 10 torr) accompanying oxygen breathing [53]. In addition, Baudelet et al. [63] found a positive correlation between R_2^* and the fraction of oxygenated hemoglobin in blood (Y) and pO_2 with an *in vitro* study using aliquots of human blood (Figure 1.6).

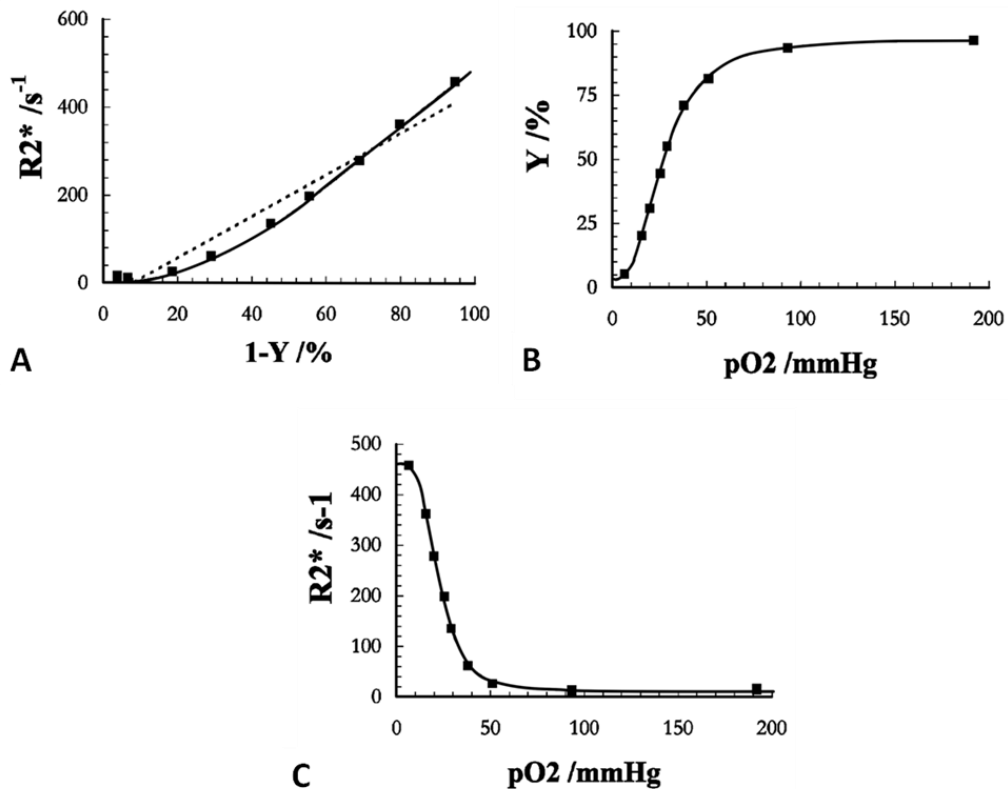


Figure 1-6 *In Vitro* studies showing the relation between blood saturation level, pO_2 and R_2^* contrast. Changes in oxygen saturation level (Y) and its effect on R_2^* MR contrast (A) and pO_2 (B). C) Correlation between R_2^* contrast and pO_2 . Adapted with permission from [63].

The degree of change in T_2^* W signal intensity (ΔSI) during an intervention can be affected by the sequence parameters. Figure 1.7 shows that the sensitivity of change can be maximized at $TE=T_2^*$ based on human prostate data acquired at 3T. Therefore, quantitative R_2^* measurements are preferable.

BOLD imaging at higher magnetic field has been of great interest. Generally, higher magnetic fields provide greater signal to noise. However, larger B_0 and B_1 inhomogeneity and increased RF power are encountered. The B_1 inhomogeneity remains manageable with 3T magnets. At 7T, however, the severe B_1 inhomogeneity causes degradation of image quality [71]. Better shimming can help in addressing the B_0 inhomogeneity at higher fields. Several approaches can be undertaken either by performing multiple conventional 3D B_0 map shims [72] or by volume shimming [73]. Despite the better shimming, B_0 inhomogeneity in regions such as the prefrontal brain still remains challenging [71].

Another limitation of acquiring BOLD at higher field is the shortened T_2^* of tissue especially for venous blood. The shorter TE required for optimal sensitivity (Figure 1.7) results in limited echo train length. Also, this will require smaller matrix size and, hence, lower spatial resolution [71].

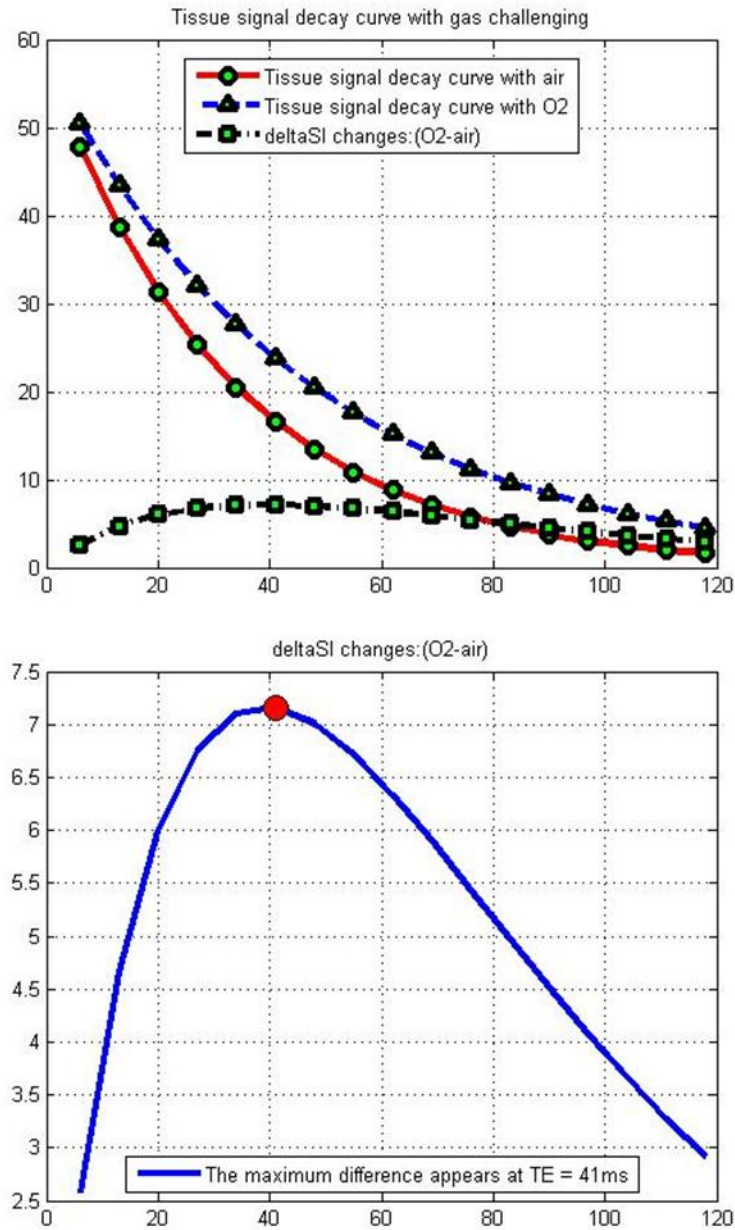


Figure 1-7 Effect of TE on changes in SI in T_2^* W images during an oxygen challenge. A) Decay curve of normal human prostate during air (red) and oxygen (blue) breathing at 3T human scanner. B) the degree of change in SI at each echo time indicating the maximum change at $TE=T_2^*$ (~41 ms).

Recently, TOLD (Tissue Oxygen Level Dependent) MRI has drawn attention in the assessment of tumor hypoxia [74]. It is based on spoiled GRE T_1 -weighted images or T_1 relaxation time measurements. T_1 oxygen dependence is primarily based on the presence of weakly paramagnetic molecular O_2 dissolved in the interstitial space and blood plasma, which is more directly related to tissue pO_2 compared to BOLD MRI. Previous studies showed [46, 75] that the difference of T_1 response to oxygen inhalation among various tissues depends on extent of the interstitial volume and regional blood flow and oxygen consumption (Figure 1.5). The quantitative explanation of T_1 change in tissues is more complicated than that in the pure blood, because the tissue oxygenation level is not readily predictable and varies significantly from one organ to another. Whereas, T_2^* oxygen dependence is based on the signal loss induced by local magnetic field inhomogeneities generated by paramagnetic dHb.

Combining BOLD and TOLD MRI is proposed to provide particularly robust insight into tumor hypoxia and potential modulation. Part of the present study is to determine the usefulness of quantitative and semi quantitative T_1 and T_2^* MRI to noninvasively predict tumor hypoxia in two syngeneic rat prostate tumor models and cervical cancer in patients.

1.3.5 Dynamic Contrast Enhanced MRI

Dynamic contrast enhanced (DCE) MRI is a routine clinical scan to examine various diseases including cancer. It requires the administration of paramagnetic contrast agents (usually based on gadolinium, Gd^{3+}) that can aid in delineating tumors by virtue of the highly fenestrated leaky vasculature [76]. Beyond the assessment of temporal and spatial variation in signal intensity following the administration of gadolinium, this technique has been widely used to reveal tumor pathophysiology [77-80]. In many cases, semi-quantitative approaches are used to characterize tumors based on simple changes in T_1 - or T_2 -weighted signal intensity, time to reach maximum change and rates of signal change. The most widely used measurement is probably IAUC (initial area under the curve) following infusion of contrast agent. Sophisticated analyses have been developed initially by direct analogy with radiotracer methods (e.g., Kety's classic approach) [79, 81]. However, drawing blood to provide absolute plasma concentrations of contrast agent is not routinely practical. Assessing the arterial input function (AIF) by imaging of a major blood vessel has been used as an alternative method, but a major vessel may not be readily visible in a given field of view. Moreover, effective characterization of the AIF normally requires very rapid imaging at the expense of high spatial resolution.

Relatively quantitative approaches require measurement of R_1 maps and the contrast agent concentration is often estimated based on changes in R_1 [82]. It has recently been shown that effective surrogates for AIF may be achieved by considering other tissues as reference regions. Indeed, this builds on the analogy to nuclear medicine, where, for instance, hypoxia is identified in tumors by relative signals from tumor (tissue of interest: TOI) versus adjacent muscle [25]. These quantitative measurements can provide multiple physiological measurements such as vascular and tissue volumes, the blood perfusion-vessel permeability product (k^{trans}) and extravascular-extracellular volume fraction (v_e), which have been correlated with tumor pathophysiology, prognostic indices and particularly as indicators of early response to therapy.

Some reports have suggested a correlation between pO_2 assessed by electrodes and DCE parameters [83-85], although others indicated a lack of correlation between DCE-MRI and changes in radiobiological hypoxic fraction [86]. Other investigators have sought correlations between BOLD and DCE. Rijpkema et al. found a correlation between BOLD and Gd-DTPA-BMA uptake in patients with meningiomas [87]. Franiel et al. found that DCE pharmacokinetic parameters aided in detecting utility in staging early prostate cancer [88].

Here, I sought to correlate quantitative DCE parameters with radiation outcome in two syngeneic rat tumor models following a single dose of 30 Gy.

1.4 PERFLUOROCARBONS

1.4.1 Background

Perfluorocarbons (PFC) are chemically inert, water insoluble, synthetic aromatic or aliphatic compounds with fluorine substituted for all hydrogen atoms [89-91]. These molecules exhibit high gas solubility due to their low intramolecular interaction and low surface tension caused by the electron-dense F atoms [90]. Their oxygen affinity linearly relates to pO_2 and obeys Henry's law. This makes PFC an excellent blood substitute product with 100 times more O_2 dissolution capacity per volume than plasma [90].

PFCs remain unmetabolized in the human body. They are either directly exhaled through the lungs or cleared by reticuloendothelial system (RES) phagocytosis and later excreted by exhalation. Therefore oximetry is particularly efficient in the liver and spleen with reports examining pO_2 response to oxygen breathing challenge [92]. In collaboration with Dr. James Brugarolas, I applied this approach to examine the influence of von Hippel-Lindau (VHL) expression and inactivation in transgenic mice (Figure 1.8) [92]. PFCs rapidly clear from the vasculature and have a reported half-life of 2-4 hours [91, 93], but can stay in tissue for weeks [94].

There are several side effects of PFCs that are not fully understood. Healthy volunteers reported a “flu-like” syndrome when PFC was administered as contrast agent, which include fever, back pain and malaise for several hours [90, 93, 95]. In addition, 30 to 40% reduction in platelet count was observed in these patients for up to 10 days following PFC administration [93, 96]; thus, preventing thrombocytopenic patients from receiving PFCs.

NMR exogenous pO_2 reporter molecules have been shown to be a useful, minimally invasive approach to quantitative assessment of tumor oximetry [31]. Reporter molecules, such as perfluorocarbons, are characterized by their high oxygen solubility and hydrophobicity, which both play important roles for *in vivo* oximetry. Molecular oxygen is paramagnetic and, therefore, shortens the nuclear longitudinal (spin-lattice) relaxation times. Most NMR oximetry applications utilize the linear dependence of R_1 of reporter molecules on pO_2 [97]. Hydrophobicity prevents the exchange of aqueous ions, which could otherwise affect the spin-lattice relaxation rate therefore calibration curves established *in vitro* may be used *in vivo* [98-100]. The sensitivity of R_1 to pO_2 is both field and temperature dependent, and thus, pertinent calibration curves are required [100-102]. The temperature dependence means that even a relatively small error in temperature estimate can introduce a sizable discrepancy into the apparent pO_2 . For example, a 1 °C error in temperature estimate would repeatedly lead to an 8 torr/°C error for perfluorotributylamine [100], 3 torr/°C for PFOB (perflubron)

[103] or 15-crown-5-ether [104] and 0.1 torr/°C for hexafluorobenzene (HFB) [101] when pO_2 is actually 5 torr.

1.4.2 Quantitative MR Oximetry Using PFCs

Several research groups have used PFC in rodent tumor studies to estimate pO_2 and it is becoming increasingly popular. Direct injection of PFC into tissue allows immediate interrogation of regions of interest without the need for vascular clearance or bias towards well vascularized regions. The use of a fine sharp needle and small volumes of reporter molecule is minimally invasive and have been reported in multiple tissues allowing measurement of oxygenation in retina [105-107], cerebral interstitial and ventricular spaces [108], brain, kidney, liver, gut, and muscle [31, 109, 110].

Dr. Mason's group favors HFB as the reporter molecule, since it has many attractive properties: a single ^{19}F NMR resonance, high R_1 sensitivity to pO_2 , minimal sensitivity to temperature, negligible toxicity and is readily available. Dr. Mason's group has previously identified the potential of HFB as a ^{19}F based pO_2 reporter molecule by *in vivo* spectroscopy and imaging [101, 111-113] using fluorocarbon relaxometry using EPI for Dynamic Oxygen Mapping (FREDOm) technique, Figure 1.9. As mentioned earlier, HFB (Figure 1.9a) has a single ^{19}F resonance and is very sensitive to changes in pO_2 with relatively little sensitivity

to temperature [33, 101]. Figure 1.9b shows the FREEDOM sequence, which consists of a train of saturation pulses followed by a recovery time τ and a spin echo EPI sequence.

FREEDOM is perfectly suited to measurements in pre-clinical animal studies and in the long term might become applicable for accessible tumors in the clinic. Clinical applications would require IND approval, which may ultimately be feasible, but time consuming. In addition, ^{19}F MRI currently is not widely available on clinical MR scanners.

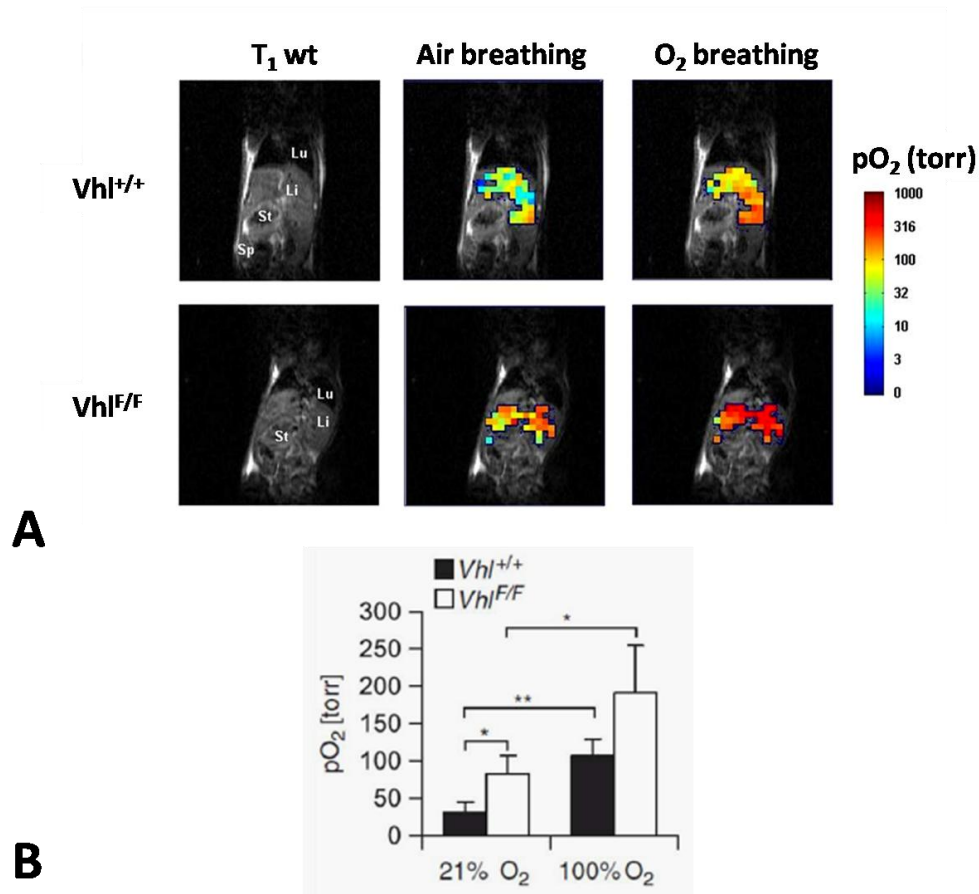


Figure 1-8 Accumulation of short acylcarnitines and inhibition of oxygen consumption in Vhl-deficient livers. A) Liver oximetry using ¹⁹F MRI of Oxypherol (perfluorobutylamine emulsion) in Vhl^{+/+} and Vhl^{F/F} mice on day 4 post injection of adenovirus coding for Cre recombinase. Representative T₁-weighted ¹H MRI coronal scans illustrating anatomy of mouse torso showing lung (Lu), liver (Li), stomach (St) and spleen (Sp) from a representative pair of animals. Overlay on anatomical images of pO₂ maps (logarithmic color scale) obtained while breathing air or 100% oxygen. B) Summary of *in vivo* pO₂ measurement (n=3 for each genotype). *P<0.05; **P<0.01, paired t test was used when comparing 21 vs 100% O₂. Data acquired by me and included in [92].

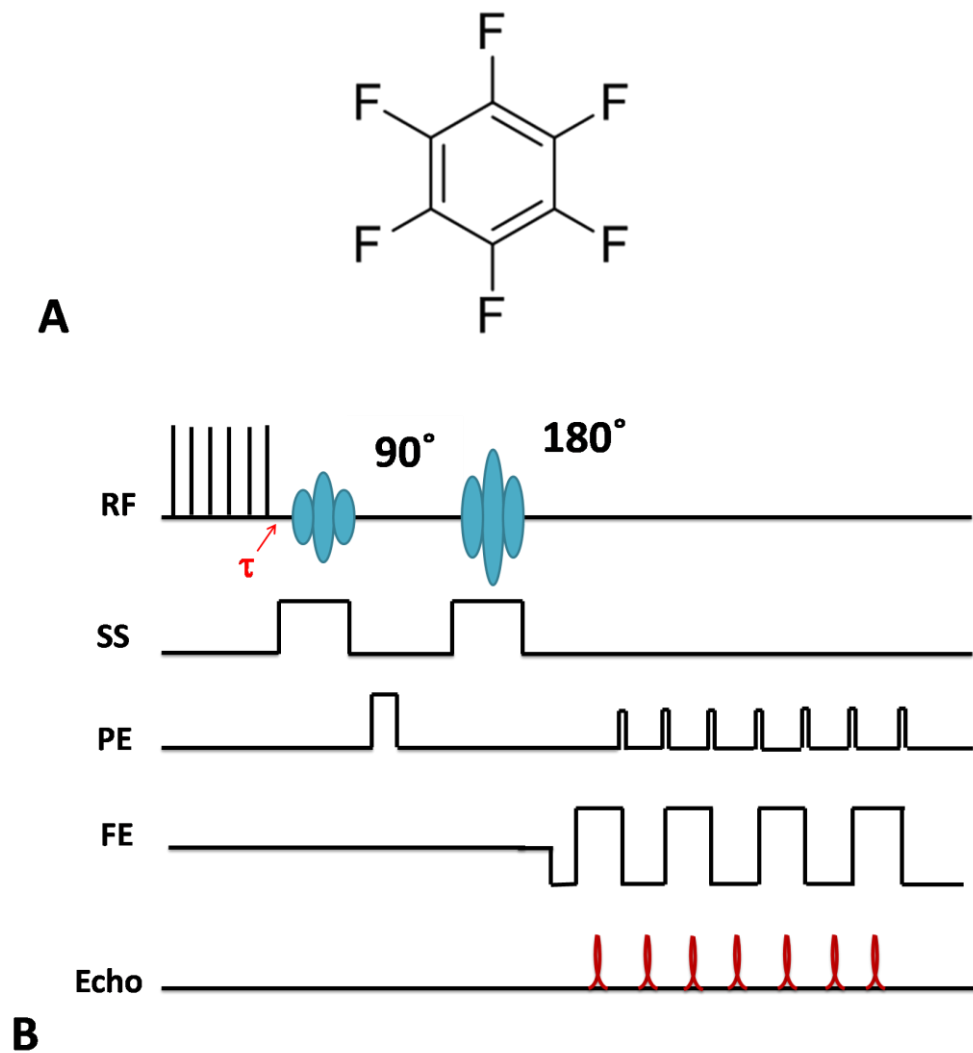


Figure 1-9 FREDOM technique A) Structure of hexafluorobenzene (HFB). B) Pulse sequence for FREDOM. RF: radiofrequency pulse; SS: slice selection; PE: phase encoding; FE: frequency encoding; τ : delay time.

CHAPTER TWO

Evaluating BOLD and TOLD Contrast MRI in Syngeneic Dunning Prostate Tumors

2.1 ABSTRACT

This study examined the potential use of BOLD and TOLD contrast MRI as non-invasive techniques to assess tumor oxygenation in tumor models. Oxygen sensitive MRI (proton BOLD and TOLD) were used to examine response of subcutaneous syngeneic Dunning R3327-AT1 and -HI prostate tumors growing subcutaneously in Copenhagen rats to hyperoxic gas breathing challenge at 4.7T. Subsequent ^{19}F MRI relaxometry based on intra tumoral injection of hexafluorobenzene (HFB) reporter molecule allowed quantitative oximetry for comparison. Tumors showed distinct heterogeneity in terms of baseline T_2^* and $p\text{O}_2$, while breathing air with higher $p\text{O}_2$ near the periphery. Both oxygen and carbogen breathing challenge elicited similar response. Strong correlations were observed between BOLD or T_2^* MRI response to hyperoxic gas challenge and quantitative ^{19}F $p\text{O}_2$ measurements. TOLD response showed a general trend, but with weaker correlation. Tumors exhibited a range of hypoxia: hypoxic tumors showed significantly smaller and more sluggish response to hyperoxic gas breathing challenge in terms of $p\text{O}_2$, T_2^* , BOLD and TOLD responses. The correlations between BOLD, TOLD and $p\text{O}_2$ measurements provide further

impetus for the use of non-invasive proton MRI with respect to a hyperoxic gas challenge as surrogate biomarkers for tumor oxygenation emphasizing potential value for clinical applications.

2.2 INTRODUCTION

Oxygen-sensitive proton MRI of water is attractive, since it is non-invasive and avoids the need for an exogenous reporter agent. Increasingly, reports suggest the feasibility of BOLD and TOLD contrast MRI in patients [37, 50, 55, 58, 60, 61, 114, 115]. BOLD effects have been evaluated in numerous animal models [46, 51, 53, 63-66, 68, 69, 116] and several studies have demonstrated a correlation with measurements of pO_2 [53, 63, 65, 66]. BOLD MRI has attracted increasing interest as a non-invasive indicator of hypoxia based on intrinsic effective transverse relaxation rate ($R_2^* = 1/T_2^*$) or response to breathing hyperoxic gas (ΔSI or ΔT_2^*). It provides an indication of tumor blood oxygenation, but is also sensitive to local hematocrit, vascular volume, pH, flow, and vessel density [46, 51, 117]. Meanwhile, TOLD MRI is based on T_1 -weighted contrast. The measured $R_1 (=1/T_1)$ is sensitive to tissue oxygenation and is distinct from BOLD imaging [74, 118, 119]. Hyperoxic gas breathing has also been evaluated in several disease sites using T_1W MRI [119]. I hypothesized that both techniques can provide complimentary information in assessing tumor oxygenation.

In this study, I explored the feasibility of using BOLD and TOLD measurements based on differences in signal intensity in T_1 - and T_2^* -weighted images, as well as relaxation rates (R_2^*) to predict tumor oxygenation. I chose ^{19}F MRI relaxometry based on the reporter molecule HFB as a correlative standard, since it provides quantitative assessment of partial oxygen pressure ($p\text{O}_2$) *in vivo*. The method is finding increasing use for assessing oxygen dynamics and is particularly convenient for correlation with proton MRI [53, 110, 120, 121]. The responses to oxygen challenge were tested by characterizing two prostate tumor lines: the Dunning prostate R3327- AT1 and -HI growing subcutaneously in syngeneic Copenhagen rats. I chose these tumor models to provide diverse patterns of hypoxia [97] and oxygenation [19], as models for tumors at any disease site. Here, I examined BOLD and TOLD MRI as surrogate biomarkers to assess tumor oxygenation, as correlated with quantitative $p\text{O}_2$ measurements.

2.3 MATERIALS AND METHODS

2.3.1 Animal Model

This study was approved by the Institutional Animal Care and Use Committee. Twenty two male Copenhagen rats (weight ~200g) were implanted with Dunning R3327-AT1 or -HI rat prostate tumors. The AT1 is an anaplastic

tumor with a volume doubling time of 5.2 days [122] and a TCD₅₀ (single radiation dose for 50% tumor control probability) of 75.7 Gy [123]. HI is a moderately differentiated, hormone-insensitive, non-metastatic and relatively slow growing subline with a tumor volume doubling time of 9 days. Tumor tissue fragments were surgically implanted subcutaneously in the thigh via a small incision. Tumor volume was calculated as $V = (\pi/6) * a * b * c$, where a, b, c, are the three orthogonal diameters and tumors were allowed to grow to 0.2 to 8 cm³.

2.3.2 Tumor Oximetry

MRI used a horizontal bore 4.7-T magnet (Varian, Palo Alto, CA) with homebuilt 2 or 3.5 cm single-turn solenoid coils, tunable to ¹H or ¹⁹F. Animals were anesthetized with isoflurane (1.5%) in air (1 L/min) and kept warm (37 °C) using a circulating warm water blanket. High resolution T₂-weighted images were acquired using a Fast Spin Echo (FSEMS) sequence: TR/TE_{eff} = 2000/48 ms, Echo Train Length (ETL) = 8, FOV = 40 × 40 mm with 128 × 128 acquisition matrix, NEX = 8, 1 mm slice thickness without gap, and 15 slices acquired in the axial orientation. Interleaved BOLD and TOLD (IBT) MR images were acquired during air breathing followed by oxygen in an automated fashion using a macro written by me as seen in Figure 2.1. To compare the effect of hyperoxic gas challenge, this was followed by re-equilibration breathing air for approximately

10 minutes followed by carbogen (CB, 95% O₂, 5% CO₂) for Group 1 rats (n=9). BOLD images were acquired using a multi-echo gradient echo sequence (MGEMS): TR =150 ms, 10 echo time values ranging from 6 ms to 69 ms with echo spacing of 7 ms, flip angle (FA) = 20°, acquisition time 21 s. TOLD images were acquired using a gradient echo sequence (GRE): TR/TE= 30/5 ms, FA=45°, acquisition time 3 seconds. The same FOV, matrix size and slice thickness were used for IBT and high resolution T₂W images. For Group 2 (the radiation study in Chapter 3, n=13 rats), similar measurements were obtained and some of those data are added here

For Group 1, quantitative pO₂ measurements were obtained using the FREDOM approach approximately 24 hours after IBT. Hexafluorobenzene (HFB, 50-100 µl, Lancaster, Gainesville, FL) was injected directly into the tumor with a custom-made fine sharp needle (32G). Injection was performed in a fan shape in a single plane as recommended [33], to ensure distribution of HFB throughout a plane of the tumor. Pulse burst saturation recovery echo planar imaging (EPI) was used to measure the spin-lattice relaxation rate, R₁, of HFB by arraying 14 delay times (τ), as described previously [33]. Five pO₂ measurements were obtained for each gas: baseline air, O₂, return to air and finally CB. The FREDOM parameters were: TR = 50 ms, TE = 21 ms, τ ranges from= 0.2 to 90 ms, NEX =1 to 12 (depending on τ), FOV=40 × 40 mm with 32 × 32 acquisition matrix, slice thickness 10 mm, giving a total acquisition time of 6½ minutes.

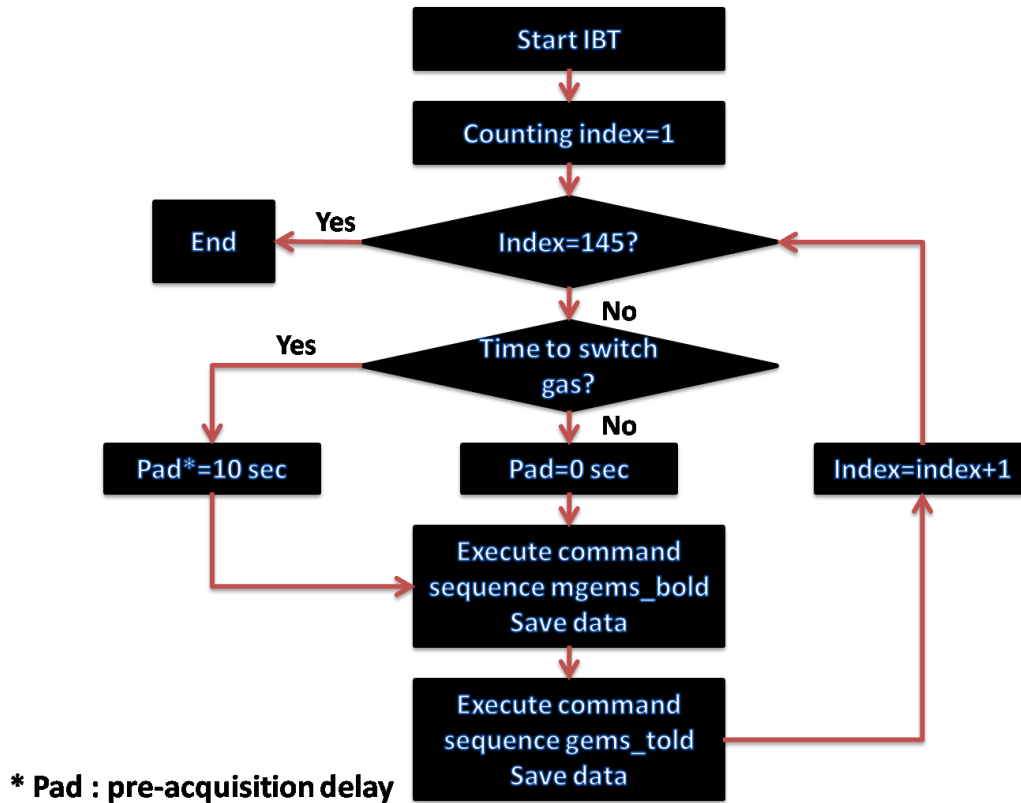


Figure 2-1 Automated acquisition of interleaved BOLD and TOLD. Flowchart of the marco written on the Varian system to acquire interleaved IBT using two different sequences MGEMS and GRE.

2.3.3 Data Analysis

MRI data were processed using Matlab (MathWorks Inc., Natick, MA) scripts written by me. Regions of interest (ROIs) were determined based on the high resolution T₂W images. Changes in signal intensity (%ΔSI) with respect to O₂ and CB challenge were calculated from the MGEMS and GRE sequences. For

BOLD images, a single TE = 20 ms was selected. Signal intensity change was calculated as:

$$\Delta SI = \frac{SI_t - SI_b}{SI_b} \cdot 100\% \quad \text{Equation 2.1}$$

where SI_b is the mean baseline signal intensity during air breathing and SI_t is the mean signal intensity with oxygen/carbogen inhalation excluding the first minute of transition to new gas.

R_2^* ($1/T_2^*$) maps were generated by fitting the multi-echo T_2^*W image signal intensity (MGEMS) to TE, as a single exponential function on a voxel-by-voxel basis:

$$SI = S_0 \cdot e^{-TE/T_2^*} + k \quad \text{Equation 2.2}$$

where SI is signal intensity at each echo time (TE), S_0 represents the original magnetization and k is a constant. Initial estimates for S_0 and T_2^* were calculated by first solving equation 2.2 based on SI at the first two TE values. The change of R_2^* or T_2^* due to oxygen/carbogen challenge was then calculated as:

$$\Delta R_2^* = R_2^*t - R_2^*b \quad \text{or} \quad \Delta T_2^* = T_2^*t - T_2^*b \quad \text{Equation 2.3}$$

where R_2^*b or T_2^*b represents mean baseline during air breathing, and R_2^*t or T_2^*t is the mean value with oxygen/carbogen inhalation.

Tumor pO_2 was measured using FREDOM and R_1 ($=1/T_1$) was estimated on a voxel-by-voxel basis using a monoexponential function:

$$SI = S_o \cdot (1 - e^{-\tau/T_1}) + k \quad \text{Equation 2.4}$$

where SI is signal intensity at tau, S_o represents the original magnetization and k is a constant. pO_2 (torr) was determined using the following relationship [33]:

$$pO_2 = \frac{R_1 - 0.0835}{0.001876} \quad \text{Equation 2.5}$$

Voxel-by-voxel measurements allowed calculation of HF₅ (hypoxia fraction of voxels with $pO_2 < 5$ torr). Only voxels with consistently reliable fitting (coefficient of determination, $R^2 > 0.95$) throughout the experiment were selected for further statistical analysis.

2.3.4 Statistical Analysis

Mean baseline SI of the T_2^*W images was calculated for each ROI and compared with O_2 and CB breathing. An average of all data points was used to determine the response to challenge excluding the first minute of transition to new gas. Significance of response to O_2 and CB challenge was assessed using Student's t-tests.

2.4 RESULTS

Tumors showed distinct heterogeneity in terms of baseline R_2^* and pO_2 while breathing air with higher pO_2 near the tumor periphery (Figure 2.2). Figure

2.3 shows mean change in SI (% Δ SI) for BOLD, TOLD, % ΔT_2^* , and pO_2 for the group of nine AT1 tumors (Group 1, Table 2.3). All measurements were quite stable during air breathing (8 minutes). Upon oxygen breathing, various changes were observed, with an average change in BOLD Δ SI = $4.4 \pm 6.2\%$, TOLD Δ SI = $0.8 \pm 2.5\%$, and $\Delta T_2^* = 1.3 \pm 2.0$ ms, or $\Delta R_2^* = -1.4 \pm 2.9$ (Figure 2.3). Following the oxygen challenge (~30 minutes), the gas was switched back to air (~15 minutes). BOLD and TOLD measurements returned to stable baseline. The measurements were repeated while switching the gas to CB (Figure 2.3). Similar responses were observed in BOLD (Δ SI $3.9 \pm 6.6\%$), TOLD (Δ SI $-0.1 \pm 3.9\%$), and ΔT_2^* (1.2 ± 2.9 ms), or ΔR_2^* (-0.9 ± 3.9 s⁻¹) upon CB breathing. FREDOM was performed on the second day to obtain corresponding pO_2 measurements on the same 9 animals. A range of pO_2 values are observed in the 9 tumors yielding a mean value of 5.5 ± 6.0 torr. Upon oxygen breathing the pO_2 increased to varying extents (mean $\Delta pO_2 = 11.1 \pm 13.0$ torr), followed by slow decrease to baseline during air breathing (~30 minutes). CB showed similar pO_2 enhancement.

Mean baseline pO_2 for individual AT1 tumors ranged from -0.5 ± 0.6 torr to 17.9 ± 1.3 torr for individual tumors with a mean of 5.8 ± 6.5 torr (median 4.1 torr) for the small tumors (< 1 cm³), while larger tumors were more hypoxic (-0.7 ± 1.6 torr to 10 ± 0.4 torr, mean = 3.1 ± 6.0 torr, median = 0.1 torr; size > 2.9 cm³, Table 2.1). Hypoxic fraction (HF₅) was more distinct and ranged from 40 to 80% for the small tumors and was over 95% for the larger tumors.

Although the concept of negative pO_2 values may appear impossible, it is perfectly reasonable, provided that errors and uncertainties are considered. These uncertainties are introduced by either curve fitting or calibration errors. The calibration curve used in my studies was introduced by Zhao et al. [33] and indicates errors in the pO_2 measurements. For example, from this calibration curve, a pO_2 value of about 75 torr has a wide range of R_1 measurement (from 0.20 to 0.25 s^{-1}). This R_1 range provides a pO_2 value of 62.1 to 88.8 torr introducing an error of about 17%. This error in R_1 measurements can be attributed to the low signal to noise in ^{19}F images, which is intensified during *in vivo* experiments. This, in turn, can provide negative pO_2 measurements if the actual pO_2 is close to 0 torr.

Some oximetry approaches ignore negative values or bin them all as zero. In my studies, I accept any value providing that the T_1 fitting is within a certain error range (coefficient of determination, $R^2 > 0.95$). The data summarized in my study (Table 2.1 and 2.2), indicate a pO_2 value \pm standard deviation of the repeated measurements during each gas. Thus the standard deviation in a pO_2 value of 1.5 ± 0.5 torr indicate a stable measurement over time.

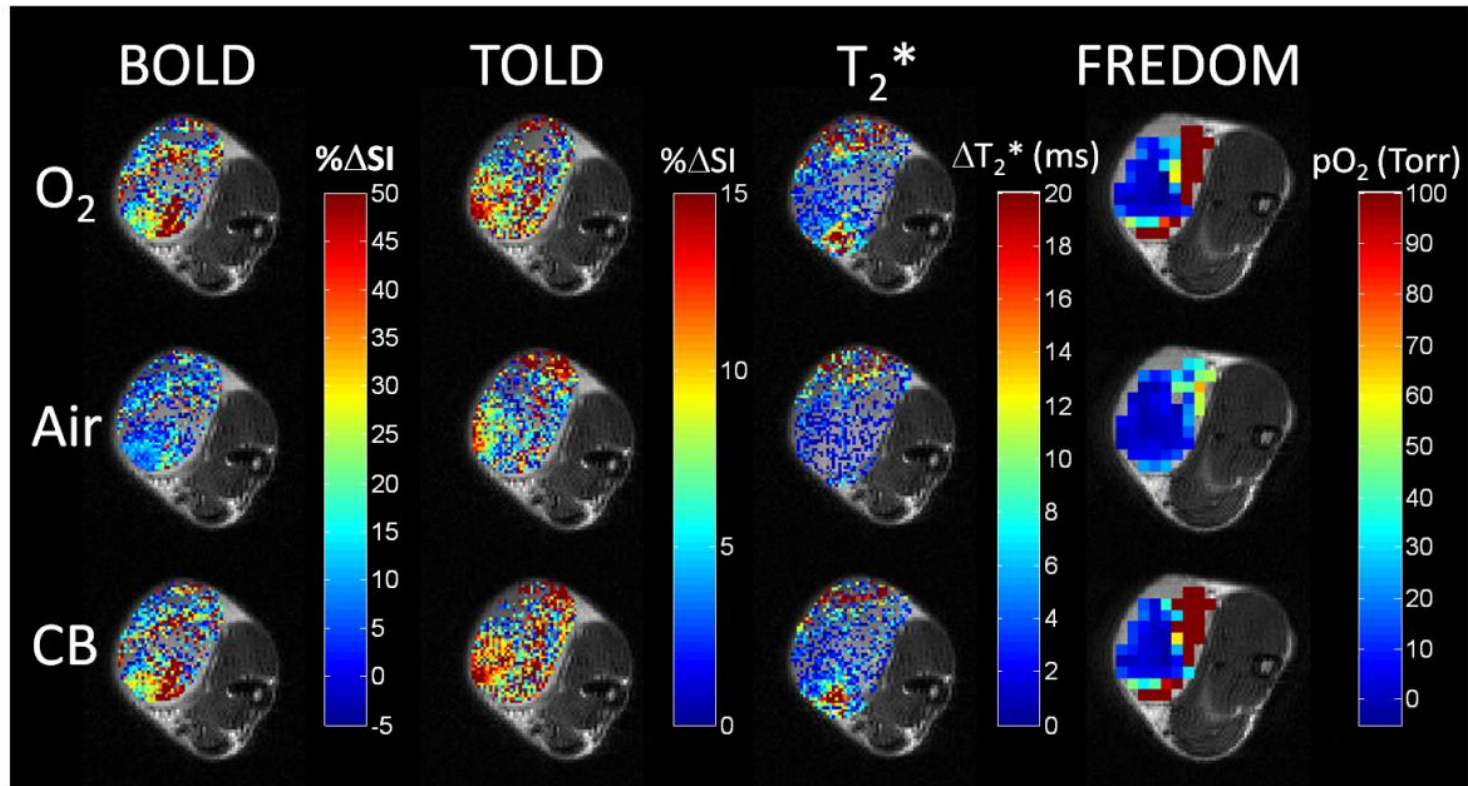


Figure 2-2 Oxygen sensitive MRI. BOLD, TOLD, T_2^* , and response maps and pO_2 maps overlaid on high resolution T_2W image of a small Dunning prostate R3327-AT1 tumor (#4, 0.5 cm^3) with respect to oxygen challenge, return to air and carbogen breathing. Response maps compare final image with each gas versus baseline. ^{19}F oximetry was performed following direct intratumoral injection of hexafluorobenzene reporter the next day.

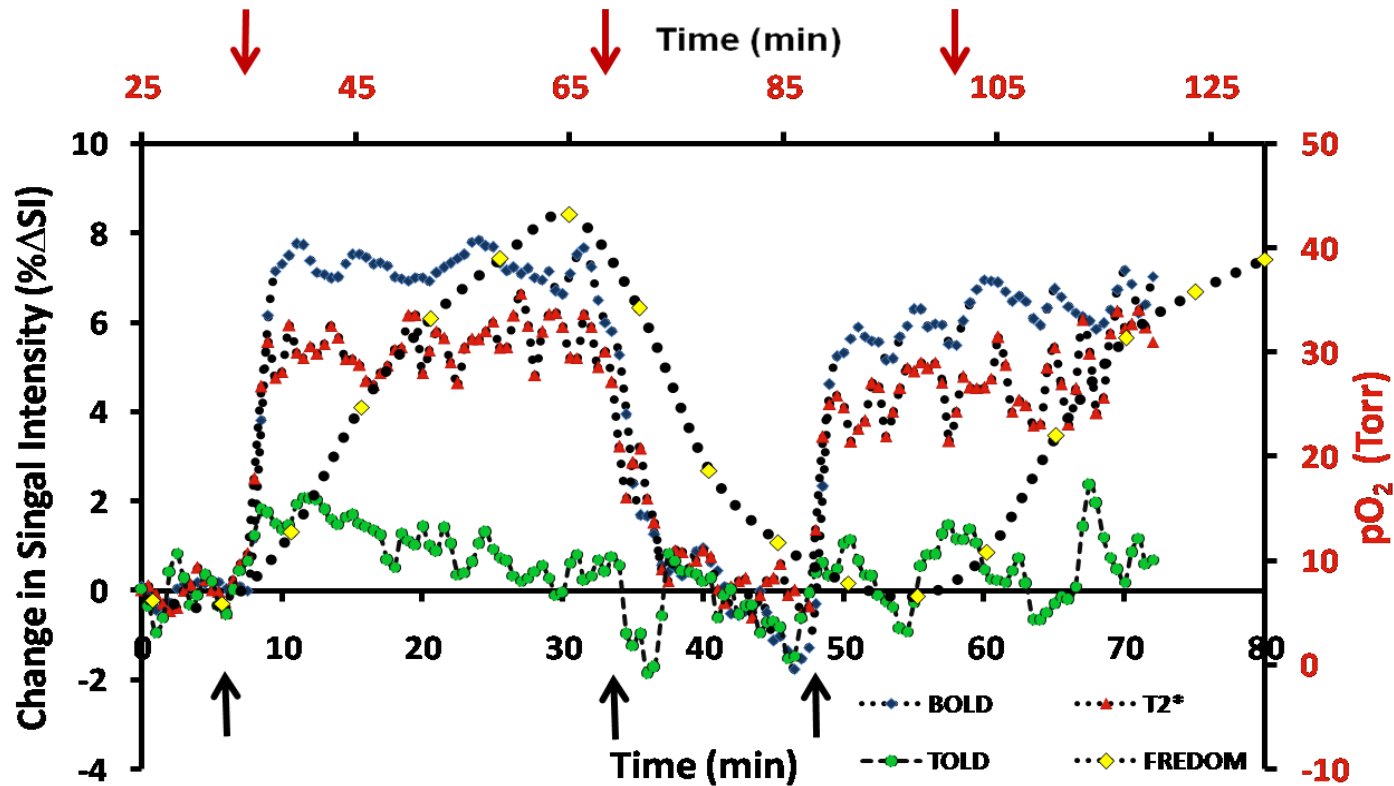


Figure 2-3 Oxygen dynamics assessed by MRI. Mean BOLD (T_2^*W % ΔSI , blue), TOLD (T_1W % ΔSI , green), and % ΔT_2^* (red) signal response to the hyperoxic gas challenge, together with pO_2 (yellow) for Group 1 tumors ($n=9$). Baseline measurements were quite stable during air breathing and changed to various extents in response to oxygen, or carbogen breathing. Arrows indicate the transition to each gas. Proton MRI measurements were observed in an interleaved manner and corresponding ^{19}F oximetry was performed following injection of hexafluorobenzene reporter the next day. Note that FREDOM has a delayed challenge for carbogen.

HI tumor sizes ranged from 0.2 to 2.0 cm³. Mean baseline pO₂ for all tumors ranged from -2.9±0.5 torr to 18.5±0.8 torr for individual tumors with a mean of 3.2±10.2 torr (median -1.4 torr) (Table 2.2). Hypoxic fraction (HF₅) ranged from 20 to 94%. All measurements were quite stable during air breathing (8 minutes). Upon oxygen breathing, various changes were observed, with an average change in BOLD $\Delta SI = 1.6 \pm 4.1\%$, TOLD $\Delta SI = 0.1 \pm 2.8\%$, and $\Delta R_2^* = -0.8 \pm 2.4 \text{ s}^{-1}$. Various responses were observed in BOLD ($\Delta SI -0.4 \pm 2.8\%$), TOLD ($\Delta SI -2.1 \pm 1.5\%$), and ΔR_2^* ($0.3 \pm 2.4 \text{ s}^{-1}$) upon CB breathing (rat#4 had no carbogen challenge). Upon oxygen breathing the pO₂ increased to varying extents (mean $\Delta pO_2 = 37.7$ torr), followed by slow decrease to baseline during air breathing (~15 minutes). CB showed similar pO₂ enhancement.

Comparing the various MR responses revealed strong correlation between ΔpO_2 and BOLD ($R^2 > 0.82$, $p < 0.001$) for eight AT1 tumors during CB and O₂ breathing (Figure 2.4A). One AT1 tumor (#9) was excluded from the analysis because the HFB was primarily injected into the center of this large tumor and therefore did not reflect the whole tumor (notably, responsive periphery). Somewhat weaker relationships were found between ΔpO_2 and ΔT_2^* ($R^2 > 0.58$, $p < 0.001$, Figure 2.4C) and ΔpO_2 and TOLD ($R^2 > 0.47$, $p < 0.004$, Figure 2.4B) for the AT1 tumors. HI had similar correlation between ΔpO_2 and ΔT_2^* ($R^2 > 0.51$, $p < 0.05$) and ΔpO_2 and TOLD ($R^2 > 0.69$, $p < 0.05$). No correlation was found between IBT and baseline pO₂.

For the AT1 tumors, ΔpO_2 tended to increase with baseline pO_2 ($R^2 > 0.47$, though for O_2 challenge alone $R^2 > 0.61$, Figure 2.4D). Correlations were also observed between ΔT_2^* and baseline T_2^* ($T_2^*_{air}$) ($R^2 > 0.4$, $p < 0.001$; Figure 2.4E, available for 22 AT1 tumors) and for semi-quantitative signal responses observed using BOLD and TOLD (Groups 1 and 2; $R^2 > 0.66$, $p < 0.001$, Figure 2.4F).

Oxygen and CB challenges caused very similar responses in AT1 tumors with mean changes for BOLD (ΔSI_{O_2} : $4.4 \pm 6.2\%$, CB: $3.8 \pm 6.6\%$), TOLD (ΔSI_{O_2} : $0.8 \pm 2.5\%$, CB: $-0.1 \pm 3.9\%$), ΔT_2^* (O_2 : 1.3 ± 2.0 ms, CB: 1.2 ± 2.9 ms) and ΔpO_2 (O_2 11.1 ± 12.9 torr, CB 10.7 ± 11.7 torr), none of which differed significantly. Likewise, strong correlations were observed between the response to the two gases for individual tumors (BOLD $\% \Delta SI$, TOLD $\% \Delta SI$, $\% \Delta T_2^*$; $R^2 > 0.83$, $p < 0.001$, Figure 2.5A) and ΔpO_2 ($R^2 > 0.75$, $p < 0.003$ Figure 2.5B). Moreover, strong correlation was observed in HF₅ during oxygen and CB breathing (HF₅ O_2 : 57%; CB: 54%, $R^2 > 0.96$; Figure 2.6A), which did not differ significantly ($p > 0.05$). Similarly, this observation was noticed when comparing responses of individual voxels in one AT1 tumor. No significant difference was shown between both gases ($R^2 > 0.98$, $p > 0.05$, Figure 2.7).

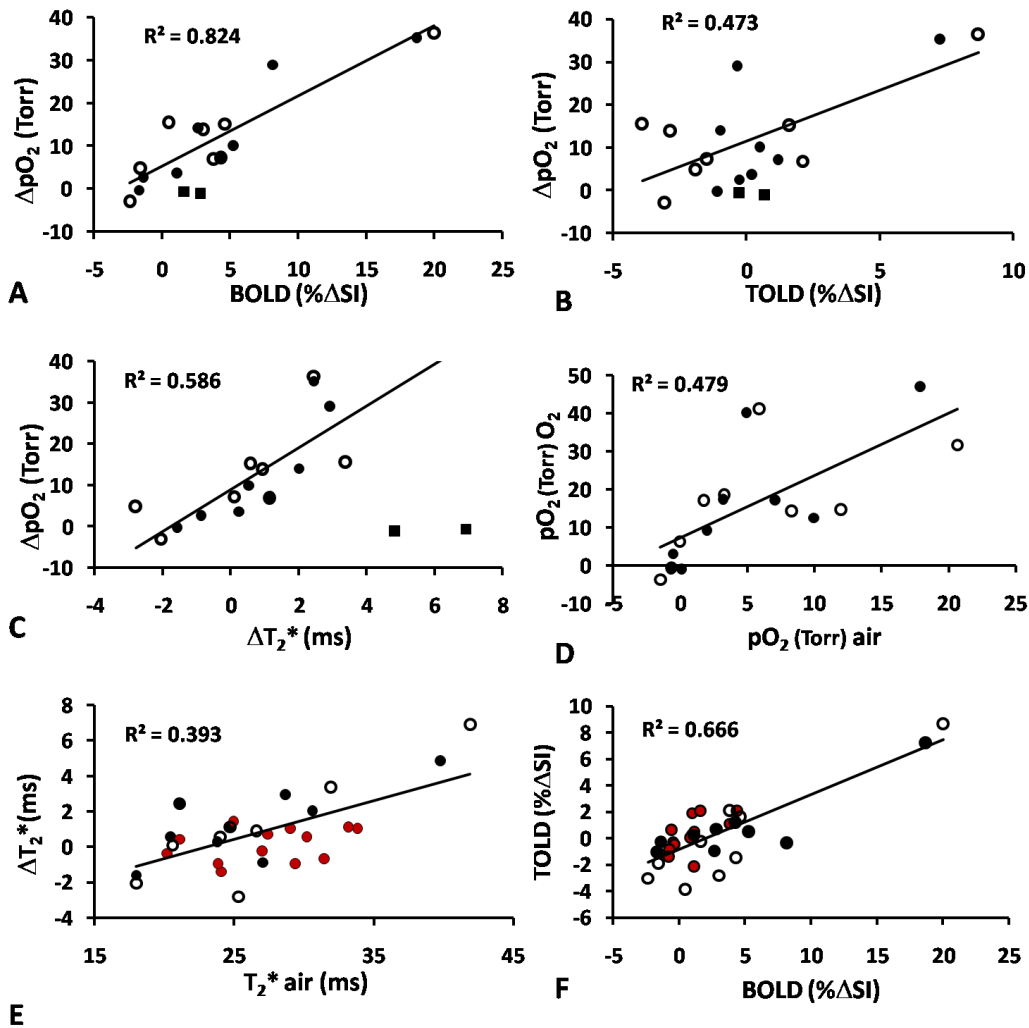


Figure 2-4 Correlation between BOLD, TOLD, and pO_2 for 9 AT1 tumors. A) Correlation between BOLD and ΔpO_2 , B) TOLD and ΔpO_2 , and C) ΔT_2^* and ΔpO_2 in response to oxygen (\bullet) and carbogen (\circ) challenges (Group 1 tumors). The HFB injection in one tumor (\blacksquare) was in the center and the data were excluded from the correlation, as being unrepresentative of the whole tumor; D) Correlation between mean pO_2 during oxygen breathing and baseline air-breathing pO_2 , E) Correlation between baseline T_2^* values (air breathing) and ΔT_2^* (red data represent Group 2 tumors); F) TOLD vs. BOLD response for all 22 tumors (Groups 1 and 2).

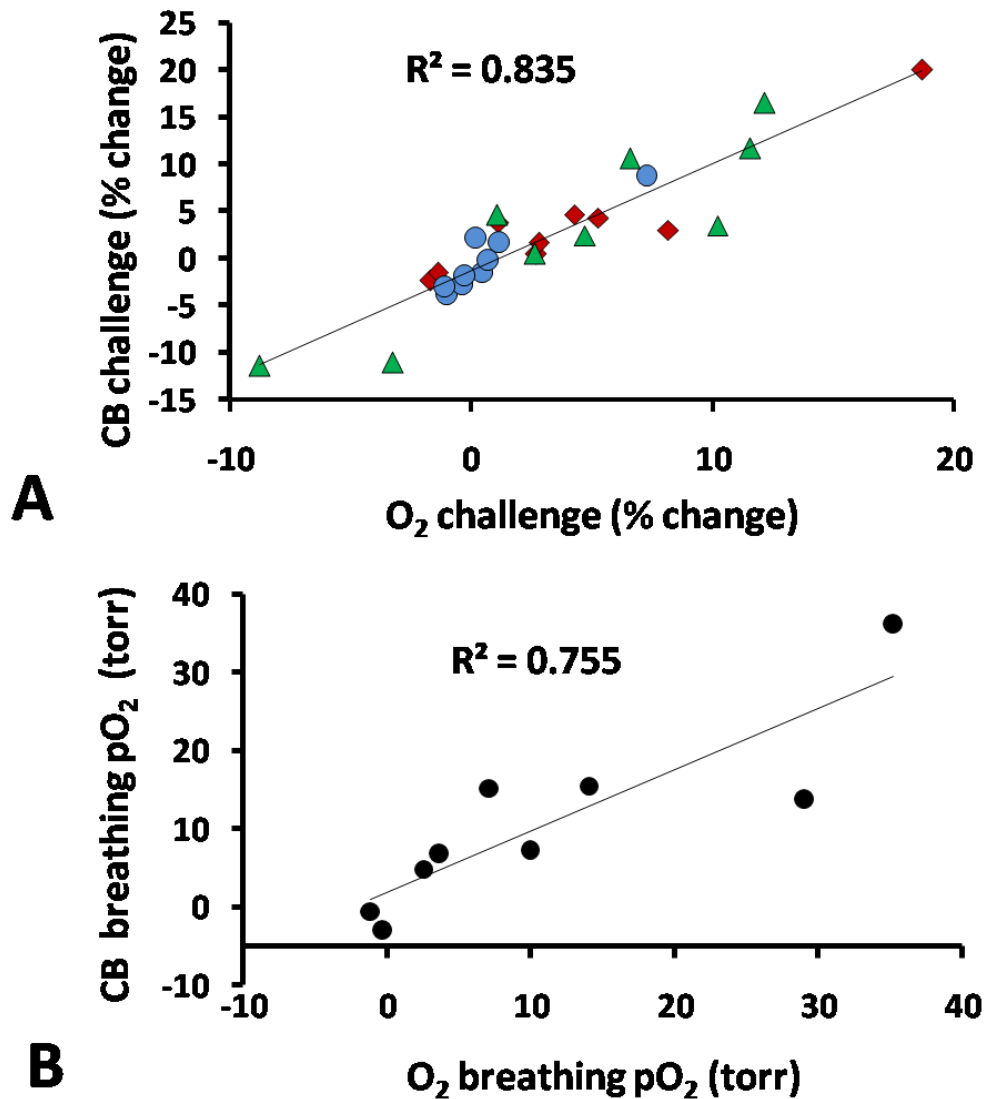


Figure 2-5 Comparison of response to oxygen and carbogen for 9 AT1 tumors. A) Correlation between BOLD (♦), TOLD (●), $\% \Delta T_2^*$ (▲) responses to oxygen and carbogen challenge assessed non-invasively using ^1H MRI. B) Correlation between oxygen and carbogen in modulating tumor pO₂ assessed using ^{19}F MRI relaxometry following direct intratumoral injection of HFB reporter.

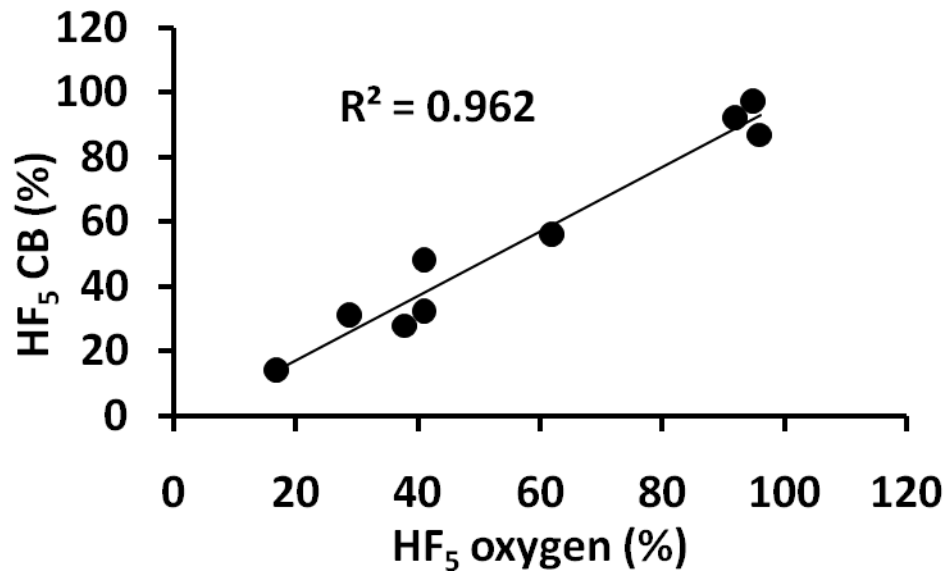


Figure 2-6 Comparison of hypoxic fraction residual to oxygen and carbogen for 9 AT1 tumors. A) Correlation between oxygen and carbogen in modulating tumor hypoxic fraction.

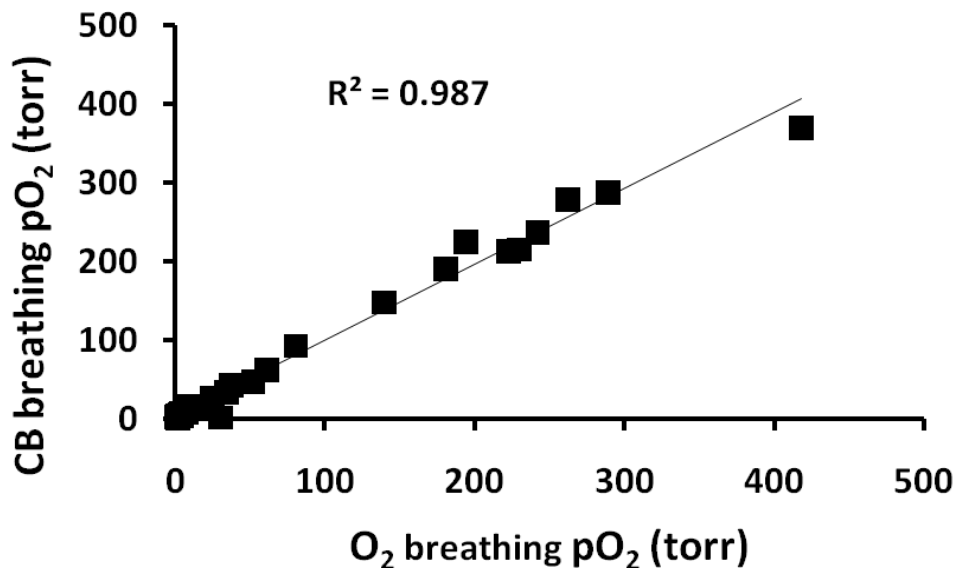


Figure 2-7 Correlations between responses of individual voxels in ¹⁹F MRI oximetry maps of a single tumor. No significant difference was observed in pO₂ in response to oxygen or carbogen breathing (p>0.05).

Tumor response to oxygen challenge was diverse, but the oxygen sensitive MRI parameters were highly consistent, as shown for representative tumors in Figure 2.8. AT1 tumor #4 (0.5 cm^3) showed large BOLD and TOLD responses (Figure 2.8A) with corresponding large increase in pO_2 , whereas AT1 tumor #6 (0.7 cm^3) showed smaller response in each parameter. Rapid BOLD signal increase and T_2^* enhancement were observed followed by slower TOLD response in tumor #4. By comparison baseline $pO_2 = 4.9 \pm 1.0$ torr ($HF_5 = 66\%$) increased to $pO_2 = 40.1 \pm 2.6$ torr ($HF_5 = 29\%$). Meanwhile, tumor #6 showed minimal BOLD and TOLD responses, lower baseline ΔpO_2 : 3.6 ± 1.0 torr, final $HF_5 = 41\%$. The change in T_2^* values and pO_2 during air and oxygen breathing can also be seen in Figure 2.8.

Similarly baseline pO_2 values correlated with response to O_2 challenge based on a pixel by pixel analysis of AT1 tumor #4, Figure 2.9A. The trend shows a linear correlation with a slope of 7.7 indicating a larger increase in response to breathing oxygen for higher baseline pO_2 values ($p < 0.001$). pO_2 values returned to their baseline values after switching the gas to air. The slope is almost unity (~ 1.02) with no significant difference observed between the pO_2 values ($p > 0.05$), Figure 2.9B.

As shown in Figure 2.10 baseline tumor oxygenation is generally heterogeneous, though quite stable. Upon hyperoxic gas breathing challenge the well oxygenated tumor regions responded rapidly and significantly with pO_2

increasing from 38 and 40 torr to 162 and 198 torr, respectively. One initially hypoxic voxel showed significant response increasing from 3 ± 2 to 14 ± 3 torr, while the other hypoxic region showed no change remaining below 2 torr. The changes in pO_2 and T_2^* upon oxygen breathing is emphasized in the histograms showing voxel-wise distribution of response (Figure 2.11).

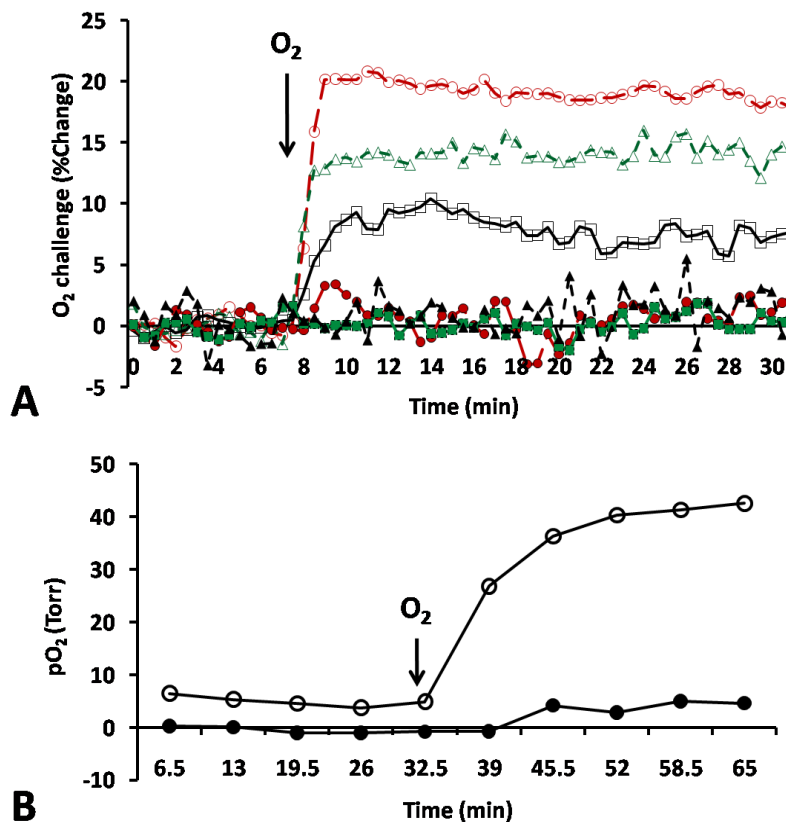


Figure 2-8 Changes in tumor oxygenation in response to oxygen breathing. A) Mean changes in BOLD (red O), TOLD (black □), $\% \Delta T_2^*$ (green Δ) for two tumors exhibiting very different response to oxygen challenge. Tumor #4 (open symbols) and # 6 (solid symbols). B) Corresponding mean changes in pO_2 . The hypoxic tumor showed little response by all measures, whereas the better oxygenated tumor was rapidly responsive.

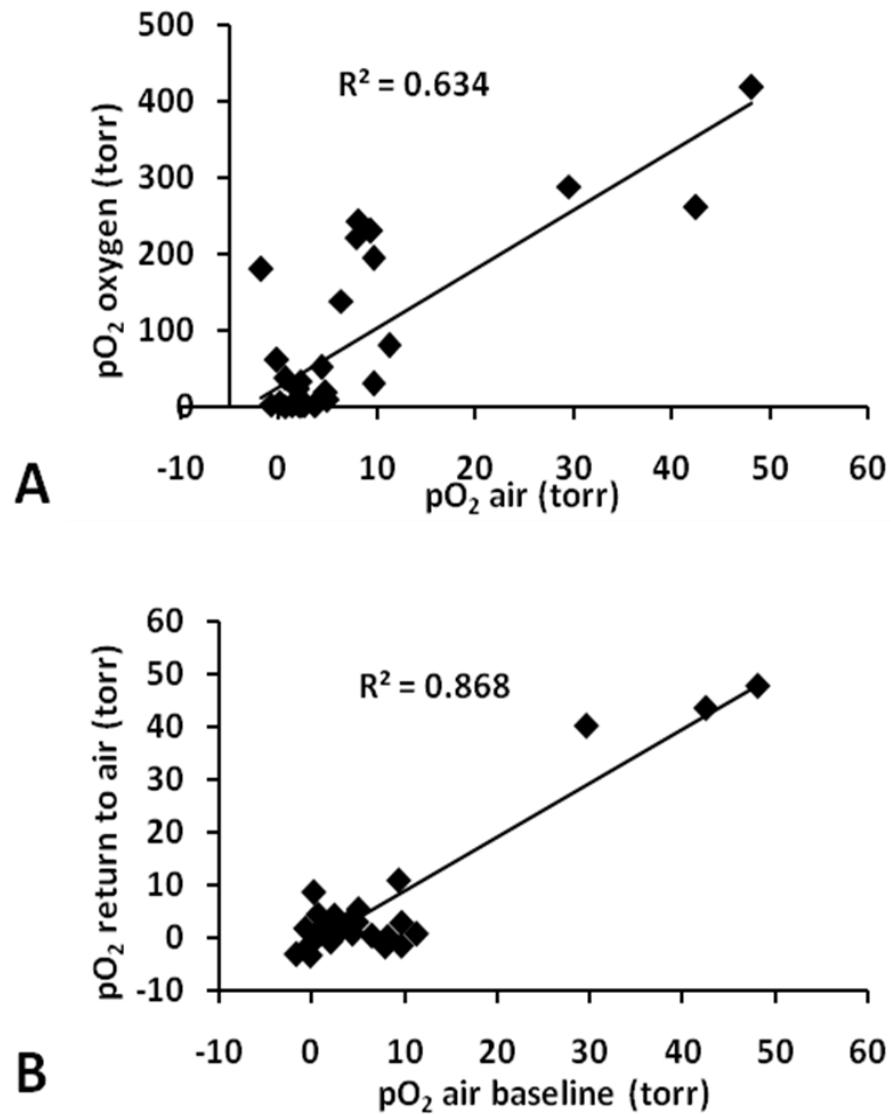


Figure 2-9 Correlations between pO₂ responses of individual voxels in ¹⁹F MRI oximetry maps of a single AT1 tumor. Correlation between pO₂ values during A) air (baseline) and oxygen breathing and B) air (baseline) and return to air.

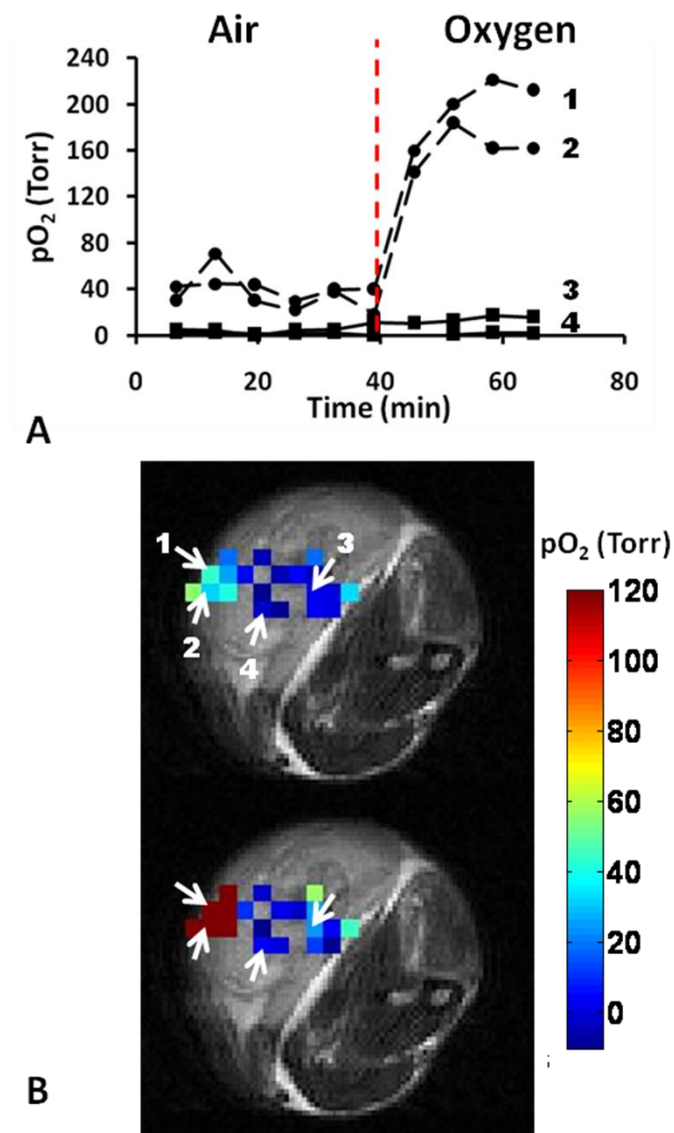


Figure 2-10 Tumor oximetry using ¹⁹F MRI Dunning prostate R3327-AT1 tumor was implanted in rat thigh and allowed to grow to about 9 mm in diameter. Images show pO₂ maps derived using FREDOM while anesthetized rat breathed air followed by 30 mins oxygen. pO₂ maps during air and oxygen breathing overlaid on a high resolution T₂W image (M muscle, B bone marrow, T tumor). A) Shows dynamic changes in pO₂ for four specific voxels (indicated by arrows in B) upon oxygen breathing. The voxels with highest baseline pO₂ show greatest and most rapid response to oxygen breathing challenge. Voxels 3 and 4 show less response although changes were significant for voxels 1-3 (p<0.01).

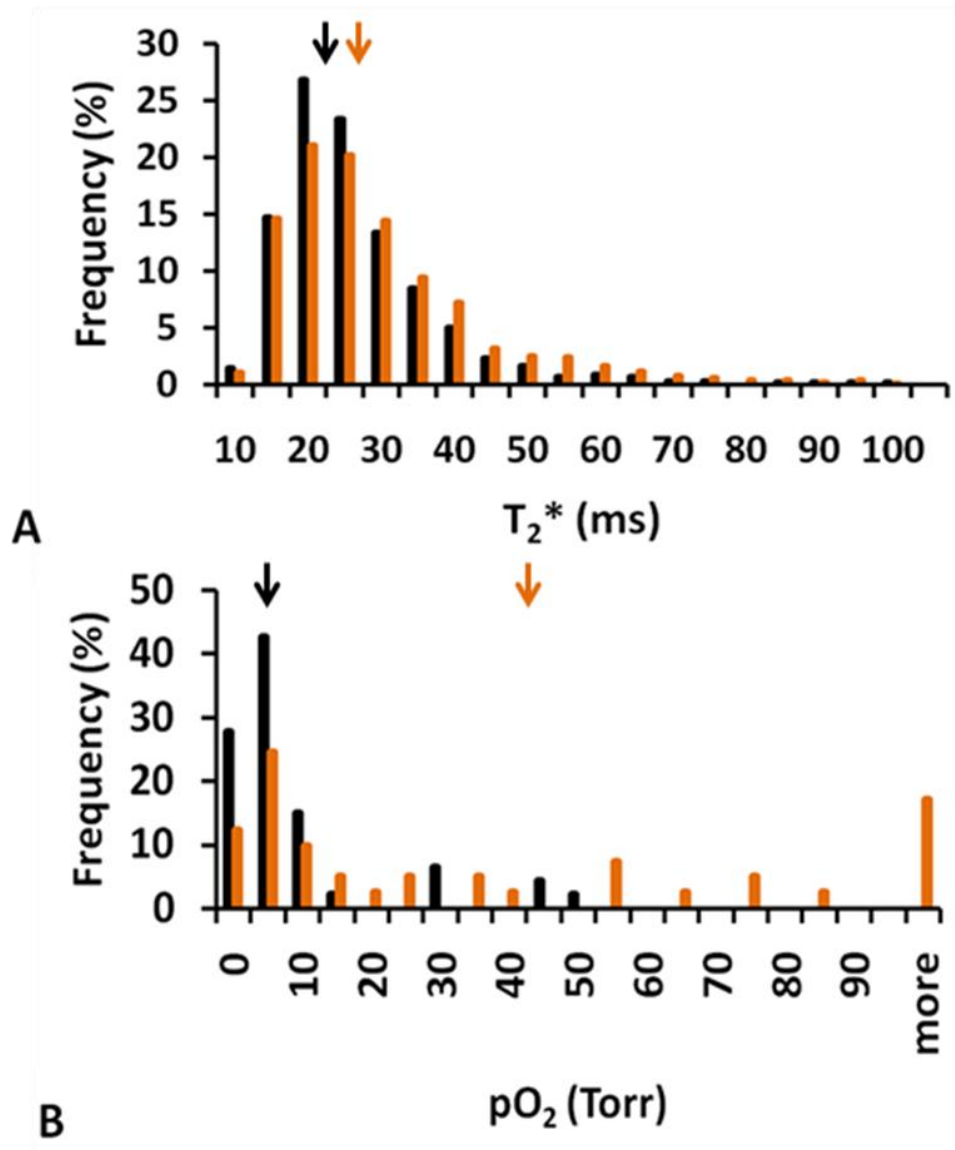


Figure 2-11 Histogram comparing ΔT_2^* and FREDOM. A representative AT1 tumor showing A) T_2^* and B) pO_2 distribution during air (black) and oxygen (orange) breathing. Arrows indicate mean values.

Table 2-1 Transverse relaxation rates and pO₂ of Dunning prostate R3327-AT1 tumors

<i>Rat #</i>	<i>Size (cm³)</i>	<i>R₂[*] (s⁻¹)</i> Air	<i>R₂[*] (s⁻¹)</i> Oxygen	<i>pO₂ (torr)</i> Air	<i>pO₂ (torr)</i> Oxygen
1	0.7	32.7±1.1	30.7±2.0	3.2±1.0	17.3±1.3
2	0.6	34.8±0.6	31.6±1.3	17.9±1.3	46.9±6.0
3	0.6	48.8±0.4	47.6±0.5	7.1±0.5	17.1±2.5
4	0.5	47.4±0.3	42.6±1.4	5.0±1.0	40.1±2.6
5	0.5	40.5±1.2	38.6±0.9	2.0±3.1	9.1±0.3
6	0.7	42.0±0.7	41.5±0.7	0.5±0.6	3.1±2.3
7	3.0	54.3±1.7	61.0±3.7	-0.7±1.6	-1.0±1.6†
8	2.9	36.9±2.7	38.2±2.6	10.1±0.4	12.6±1.1
9	8.8	25.1±0.9	22.4±1.3	0.1±0.3	-1.1±0.4

All R₂^{*} and pO₂ responses were significant (p<0.01) except † (NS). Values indicate mean ± SD

Table 2-2 Transverse relaxation rates and pO₂ of Dunning prostate R3327-HI tumors

<i>Rat #</i>	<i>Size (cm³)</i>	<i>R₂[*] (s⁻¹)</i> Air	<i>R₂[*] (s⁻¹)</i> Oxygen	<i>pO₂ (torr)</i> Air	<i>pO₂ (torr)</i> Oxygen
1	0.6	47.2±0.5	46.4±0.6	-2.9±0.5	-2.3±1.3†
2	1.6	30.0±2.5	32.1±4.5	-1.5±0.5	-0.9±0.6
3	2.0	28.2±2.2	27.4±1.9†	-1.2±0.9	0.2±0.3
4	0.2	71.2±1.3	67.5±1.4	18.5±0.8	166.0±4

All R₂^{*} and pO₂ responses were significant (p<0.01) except † (NS). Values indicate mean ± SD

Table 2-3 Effect of oxygen breathing on BOLD and TOLD MRI of Dunning prostate R3327-AT1 tumors.

<i>Rat #</i>	<i>Size (cm³)</i>	<i>BOLD (%ΔSI)</i>	<i>TOLD (%ΔSI)</i>
1	0.7	2.7±1.2*	-1.0±2.4
2	0.6	8.2±2.9*	-0.4±1.4
3	0.6	5.3±1.8*	0.5±1.1
4	0.5	18.7±5.3*	7.3±2.2*
5	0.5	4.3±1.4*	1.2±1.0*
6	0.7	1.2±2.1	0.2±0.8
7	3.0	-1.7±0.7*	-1.1±0.8*
8	2.9	-1.4±1.1*	-0.3±0.9
9	8.8	2.8±0.8*	0.7±0.5*

Values indicate mean ± SD

2.5 DISCUSSION

This study showed robust correlations between BOLD and TOLD responses and these responses coincided with change in absolute pO₂. Quantitative BOLD and TOLD measurements were readily implemented and gave consistent results.

Overall the smaller tumors (volume <1 cm³) were significantly better oxygenated (p<0.05) than the larger ones (>3 cm³) in accord with previous studies

regarding AT1 tumors [34, 97, 111, 124], although individual tumors showed a wide range of hypoxic fractions. Generally, the smaller tumors showed larger pO_2 changes upon oxygen breathing. Likewise, smaller tumors tended to exhibit larger changes in BOLD ($6.3 \pm 6.3\%$), TOLD ($1.0 \pm 3.7\%$), and T_2^* (1.5 ± 1.1 ms) compared to larger tumors BOLD ($-0.3 \pm 2.0\%$), TOLD ($-0.9 \pm 1.3\%$), and T_2^* (0.7 ± 4.1 ms), although these differences did not reach statistical significance for the groups. Every individual small tumor showed significant increase in T_2^* and pO_2 with oxygen breathing, whereas changes in the large tumors were inconsistent. Tumors with lower baseline pO_2 tended to exhibit smaller pO_2 response to O_2 challenge (Table 2.1) and as a corollary those with greater baseline hypoxic fraction retained a large hypoxic fraction. Indeed, each of the oxygen sensitive parameters behaved quite consistently whereby tumors exhibiting high baseline pO_2 on Day 2 had shown larger BOLD, TOLD and T_2^* response to oxygen challenge on the previous day (Figure 2.8).

Strong correlations were found between both quantitative and semi-quantitative BOLD responses and ΔpO_2 measurements ($R^2 > 0.8$) in line with previous reports for rat mammary tumors 13762NF [53] and R3230AC [66]. Indeed, general correlations between BOLD response (variously assessed as change in signal intensity, change in local linewidth or quantitative T_2^*) and change in pO_2 have been reported in diverse tumors based on various quantitative oximetry techniques (e.g., ESR [64, 65], fiber optic probes [63], electrodes [125])

and ^{19}F MRI [53, 66]). The relationship is often not linear, however, presumably reflecting the O_2 -hemoglobin binding characteristics [51]. Some reports indicate that T_2^* alone may be indicative of hypoxia in tumors [50, 126], though vascular extent can have a strong influence [46, 47]. As such, adding TOLD measurements should help identify hypoxia irrespective of vasculature, since T_1 is directly sensitive to pO_2 .

However, except for one tumor (#4), the HI tumors didn't show the large responses expected from previous studies. Both pO_2 measurements and IBT showed small changes with intervention and tumors were found to grow more rapidly than expected suggesting tumor line drift.

Combining BOLD and TOLD measurements is increasingly utilized for characterizing normal tissues and tumors in patients [119]. Further studies have been reported in rat and rabbit tumors [127, 128]. Noting that BOLD response was generally greater than TOLD prompts the question of the advantage of measuring both parameters. A particular concern with BOLD alone is that it is subject to additional influences such as flow [46], and has been reported to exhibit contradictory behavior with respect to tumor oxygenation in some cases [46, 69]. Noting that BOLD responses preceded TOLD (Figure. 2.7) adds confidence to the oxygen dependence, since enhanced oxygen delivery generates elevated pO_2 . T_1 measurements typically require longer acquisition times and application of sequential pulse sequences, as presented here, may significantly increase study

times, making it impractical for the clinic. In this regard innovative simultaneous measurements are being developed [129, 130].

My results provide further evidence for the utility of oxygen-sensitive MRI for characterizing tumor hypoxia. The T_2^* -weighted measurements coincide with independent oximetry for these tumors, and hence, appear useful as non-invasive surrogate prognostic biomarkers to assess hypoxia, and revealed response to hyperoxic gas breathing interventions. Indeed, in a previous study in rat breast tumors, it was shown that a BOLD signal response exceeding 3% coincided with elimination of hypoxic fraction ($HF_{10} < 5\%$) [53]. However, T_2^* -weighted measurements alone are subject to additional influences and thus adding T_1 -weighted imaging appears valuable. Change in signal intensity alone appears useful, but the magnitude of response depends on R_1 and R_2^* , together with echo (TE) and repetition (TR) times. Moreover, tumor motion precludes effective signal subtraction. Immobilizing tumors in small animals is reasonably straightforward, but in patients, respiratory or cardiac motion, or other movements such as swallowing, bladder filling and bowel peristalsis, may preclude effective signal subtraction. Even if image co-registration isn't perfect, histograms for R_1 and R_2^* distributions may be compared with respect to interventions.

Importantly, oxygen sensitive MRI is non-invasive, simple to implement, highly reproducible and reveals spatial and temporal heterogeneity of oxygen dynamics. It does not quantify pO_2 or hypoxic fraction (potential advantages of

^{19}F oximetry, ESR, or electrodes [19]), but requires no exogenous reporter molecule or needle insertion.

2.6 CONCLUSION

The correlations between BOLD, TOLD and pO_2 measurements provide further impetus for the use of non-invasive proton MRI with respect to a hyperoxic gas challenge as surrogate biomarker for tumor oxygenation emphasizing potential value for clinical applications. Nevertheless, the relationships between observed changes and pO_2 must be investigated further. Tumor stratification (oxic vs. responsive to oxygen breathing vs. hypoxic) may allow therapy to be tailored to characteristics of the tumor. In the future, it will be crucial to compare individual tumors with respect to irradiation and my results provide sound impetus to further evaluate this approach, which can easily and directly be translated to clinic.

CHAPTER THREE

Predicting Radiation Response Using Noninvasive ^1H Imaging

3.1 ABSTRACT

This study examined the potential use of BOLD, TOLD, and DCE contrast MRI as non-invasive techniques to predict tumor response to a single high dose radiation treatment. Oxygen sensitive MRI (proton BOLD and TOLD) and DCE were used to examine response of subcutaneous syngeneic Dunning R3327-AT1 and -HI prostate tumors growing in rats to hyperoxic gas breathing challenge or Gd-DTPA infusion at 4.7T. A subgroup of tumors was irradiated with a single high dose of 30 Gy and growth delay was compared with pre-irradiation BOLD, TOLD and DCE assessments. Tumors showed distinct heterogeneity in terms of baseline T_2^* and T_1 , while breathing air. Irradiation caused a significant tumor growth delay of about 30 days for tumors to quadruple in volume. No obvious correlation was observed between tumor growth delay and BOLD response, but those tumors with larger changes in both TOLD and T_1 values upon oxygen breathing exhibited significantly greater tumor growth delay. Notably, tumor growth delay roughly doubled. These results provide further insight into the relationships between oxygen sensitive MRI parameters and indicate that response to hyperoxic gas challenge is related to radiation response. Studies hitherto have focused on pre-clinical models of prostate cancer, notably in rats.

The data provide rationale for expanding the studies to other tumor sites and progressively patients. Since the method is entirely non-invasive it should permit ready translation to clinical patients.

3.2 INTRODUCTION

It has long been appreciated that hypoxic tumor cells are more resistant to radiotherapy [18]. Indeed, a three fold increase in radio resistance may occur when cells are irradiated under hypoxic conditions compared with $pO_2 > 15$ torr for a given single radiation dose. The clinical significance of hypoxia for radiotherapy was recently illustrated by modeling the radiation response of a heterogeneous cell population [131]. Increasingly, there is evidence that hypoxia also influences angiogenesis, tumor invasion and metastasis [132-135]. Moreover, repeated bouts of intermittent hypoxic stress may be important in stimulating tumor progression [136]. Thus, the ability to assess tumor oxygenation non-invasively, and repeatedly, with respect to acute or chronic interventions becomes increasingly important.

DCE-MRI has been extensively studied by various groups and suggested to be a useful method for evaluating blood perfusion, extracellular volume fraction, and the extent of hypoxia in tumors [137-139]. Several mathematical models, such as the modified Kety model developed by Tofts et al. [79], have been

developed to generate parametric images of k^{trans} and v_e by subjecting DCE-MRI series to pharmacokinetic analysis.

In the present chapter, I evaluated the potential use of three ^1H MR imaging techniques BOLD, TOLD and DCE in predicting the radiation outcome of two tumor sublines of the Dunning prostate R3327: AT1 and HI. A subgroup of tumors was irradiated with a single high dose of 30 Gy and growth delay was compared with pre-irradiation BOLD, TOLD and DCE assessments. Irradiation caused a significant tumor growth delay. No obvious correlation was observed between tumor growth delay and BOLD response, but those tumors with larger changes in both TOLD and T_1 values upon oxygen breathing exhibited significantly increased tumor growth delay. In addition, a correlation was observed between v_e and radiation outcome. These results provide further insight into the relationships between oxygen sensitive MRI parameters and indicate that response to hyperoxic gas challenge is related to radiation response.

3.3 METHODS

3.3.1 Oxygen Sensitive MRI

For Group 2 (the radiation data of the study in Chapter 2, n=13 AT1 tumors, n=8 HI tumors), IBT MRI was acquired in a similar manner to that discussed in

Chapter 2.3, but with only oxygen used as a challenge. In this study, T_1 measurements were additionally acquired using a spin echo sequence (SEMS) before and after IBT during air and oxygen breathing: TE= 20 ms, TR= 0.1, 0.2, 0.3, 0.5, 0.7, 0.9, 1.5, 2.5, 3.5 s, FOV=40 × 40 mm with 64 × 64 acquisition matrix, though this was zero-filled to 128x128 to allow voxel-wise comparison with IBT.

3.3.2 Dynamic Contrast Enhanced MRI (DCE)

Following IBT and T_1 measurements, time course DCE data were acquired continuously using a spin-echo sequence with TR/TE of 100/10 ms pre (acquisition time ~11sec) and up to 30 minutes post-injection of 0.1 mmole/kg body weight Gd-DTPA (Magnevist®) intravenously. Images were acquired with the same spatial resolution as BOLD/TOLD. R_1 maps were acquired before contrast injection in order to facilitate conversion of signal intensity data to contrast agent concentrations.

3.3.3 Radiation Treatment

Radiation was delivered using a dedicated small animal x-ray irradiator (XRAD 225Cx, Precision X-Ray, Inc., North Branford, CT). The XRAD 225Cx

features an x-ray tube mounted to a c-arm gantry, which rotates about a motorized x-y-z (3D) translational stage (Parker 404XE, Parker–Hannifin Corporation, Irwin, PA). Absolute dose calibration was performed in accordance with the recommendations of the AAPM TG-61 protocol [140]. The XRAD 225Cx was operated at 225 kV and 13 mA, producing a dose rate of approximately 3.5 Gy/min. A circular aperture 20 mm in diameter was used to limit the radiation beam only to the tumor. An image guidance system utilizing a digital imaging panel for digital radiography, fluoroscopy, and cone-beam CT (CBCT) was used to ensure accurate localization. Irradiation was performed by Dr. Timothy Solberg's radiation physics group.

Rats were divided into three sub-groups: Group 2a (AT1 n=2; HI n=2) were sham irradiated (control), Group 2b (AT1 n=5; HI n=3) breathed air during irradiation, and Group 2c (AT1 n=6; HI n=3) breathed oxygen 15 minutes before irradiation and during irradiation. Tumor volume (V), measured with calipers, was normalized to the day of irradiation (V₀) and response was evaluated as the time to double (T₂) and to quadruple (T₄). One animal died before T₄ and the day of death was taken as T₄.

3.3.4 Statistical Analysis

DCE data were analyzed using recent models avoiding the need to directly measure the arterial input function (AIF). The Model compares the contrast agent curves in a tissue of interest (tumor) to that of a reference region (muscle) [141]. Using known values for K^{trans}_M (the blood perfusion-vessel permeability product) and v_{eM} (extravascular-extracellular volume fraction) in the muscle, it is possible to extract the K^{trans} and v_e values for the tumor without knowledge of the AIF. In this model, Contrast curve, $C(t)$, in tumor tissue is given by [82]:

$$C(t) = R * CM(t) + R * \left[\frac{K^{trans}_M}{v_{eM}} - \frac{K^{trans}}{v_e} \right] * \int_0^t \left(CM(t') * \exp\left(-\frac{K^{trans}}{v_e} * (t - t')\right) \right) dt'$$

re $R = (K^{trans} / K^{trans}_M)$ and $CM(t)$ is the contrast agent curve in muscle tissue. K^{trans}/v_e is often referred to as k_{ep} .

3.4 RESULTS

For Group 2 (n= 13 AT1 and 8 HI), IBT studies were performed with respect to O_2 only, and quantitative T_1 measurements and DCE MRI were added. Quantitative pO_2 measurements were not included to eliminate the effect of invasive administration of HFB on tumor growth. The data showed good quality and provided good curve fitting ($R^2 > 0.95$), as the raw images and fitting curves

indicate in Figure 3.1 and 3.2. DCE images were acquired with the same spatial resolution as IBT to allow comparison. Representative images of BOLD, TOLD, ΔT_2^* , ΔT_1 , K^{trans} and v_e maps for both AT1 and HI can be seen in Figures 3.3 and 3.4, respectively.

The day following the MR measurements, radiation therapy was performed. Two tumors served as unirradiated controls (Group 2a, mean $V_0=0.4\pm 0.1 \text{ cm}^3$). The other tumors received a 30 Gy irradiation dose, while rats breathed air (n=5; $V_0=0.5\pm 0.3 \text{ cm}^3$) or O_2 (n=6; $V_0=0.5\pm 0.2 \text{ cm}^3$).

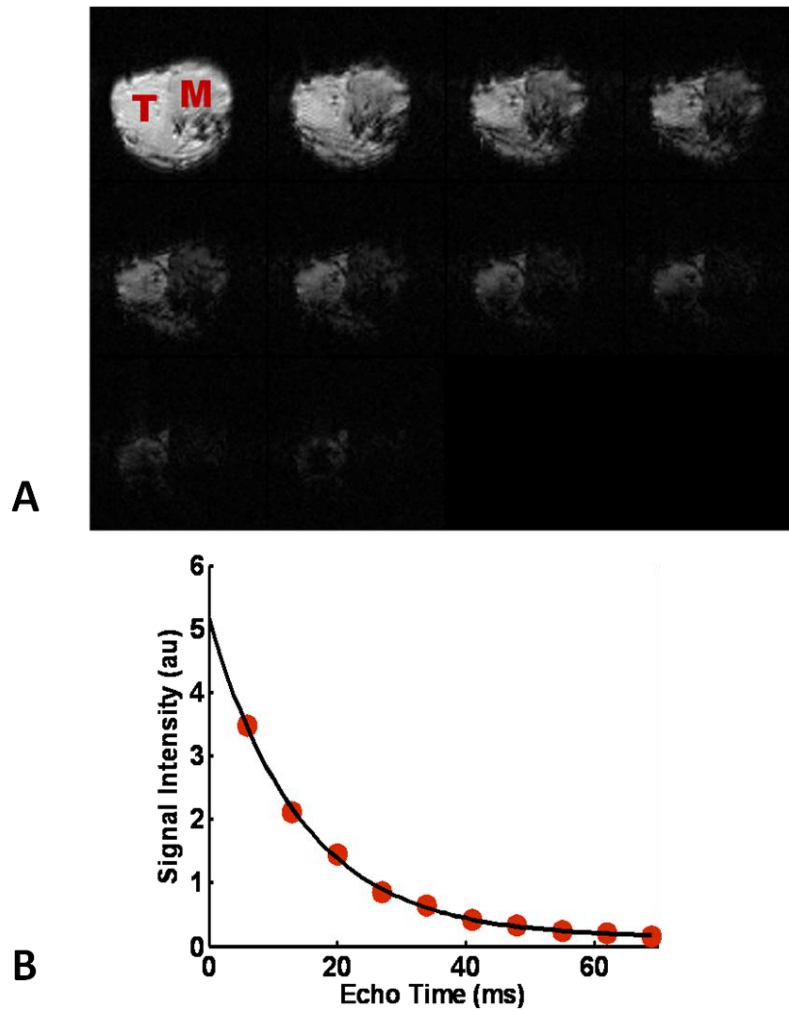


Figure 3-1 Raw T_2^*W images and fitting quality. A) T_2^*W images acquired as a part of the BOLD study indicating the tumor (T) and muscle (M). B. Decay curve of the tumor signal intensity as a function of echo time ($R^2 > 0.95$)

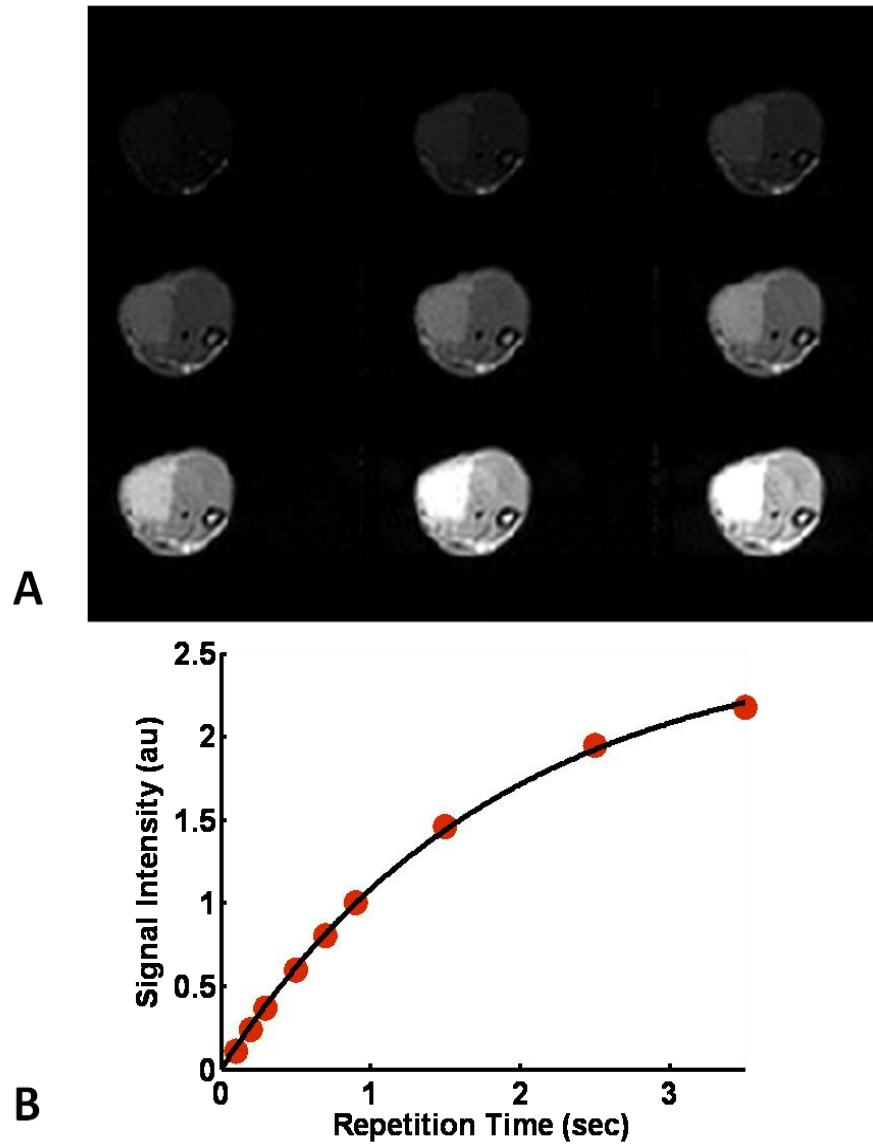


Figure 3-2 Raw T₁W images and fitting quality. A) T₁W images acquired for the same tumor as in 3.1. B) Relaxation curve of the tumor signal intensity as a function of repetition time ($R^2 > 0.95$)

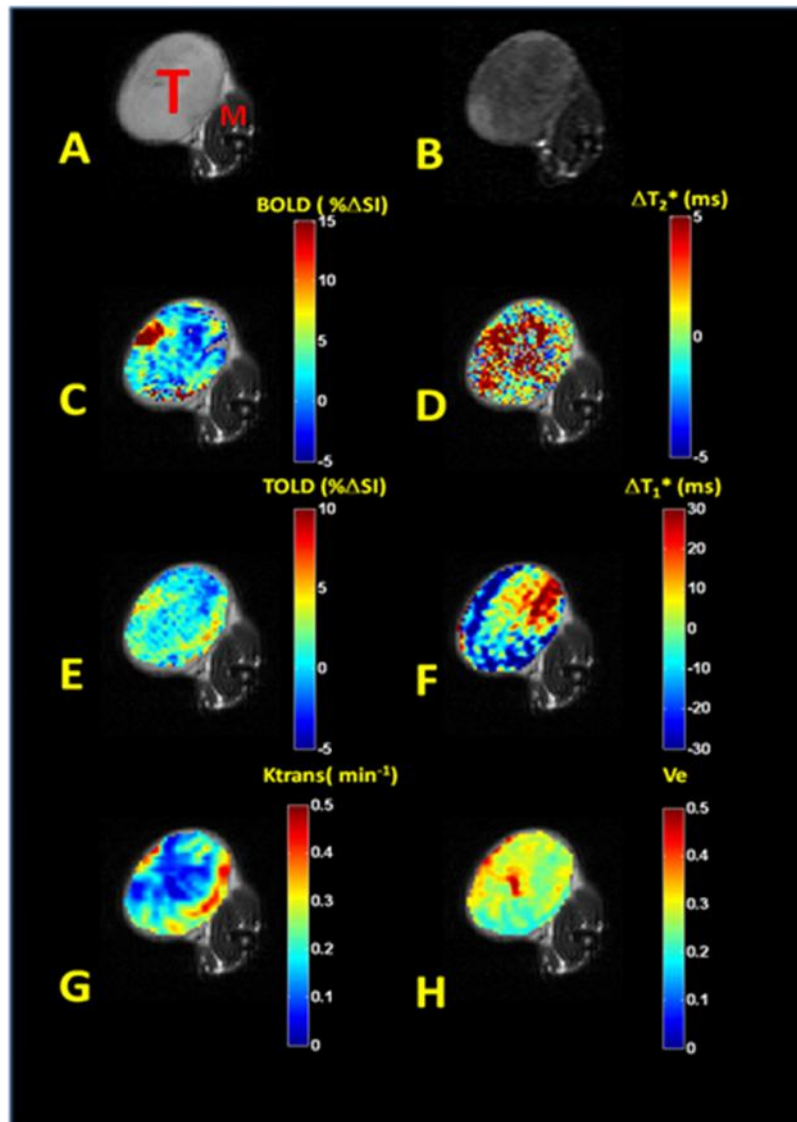


Figure 3-3 Oxygen sensitive MRI. A) High resolution T₂W image showing the tumor (T) and muscle (M). B) Post-contrast (Gd-DTPA) T₁W. C) BOLD, D) T₂^{*}, E) TOLD, F) T₁, G) k^{trans} and H) v_e response maps overlaid on high resolution T₂W image of a small Dunning prostate R3327-AT1 tumor (0.8 cm³) with respect to oxygen challenge or Gd-DTPA infusion.

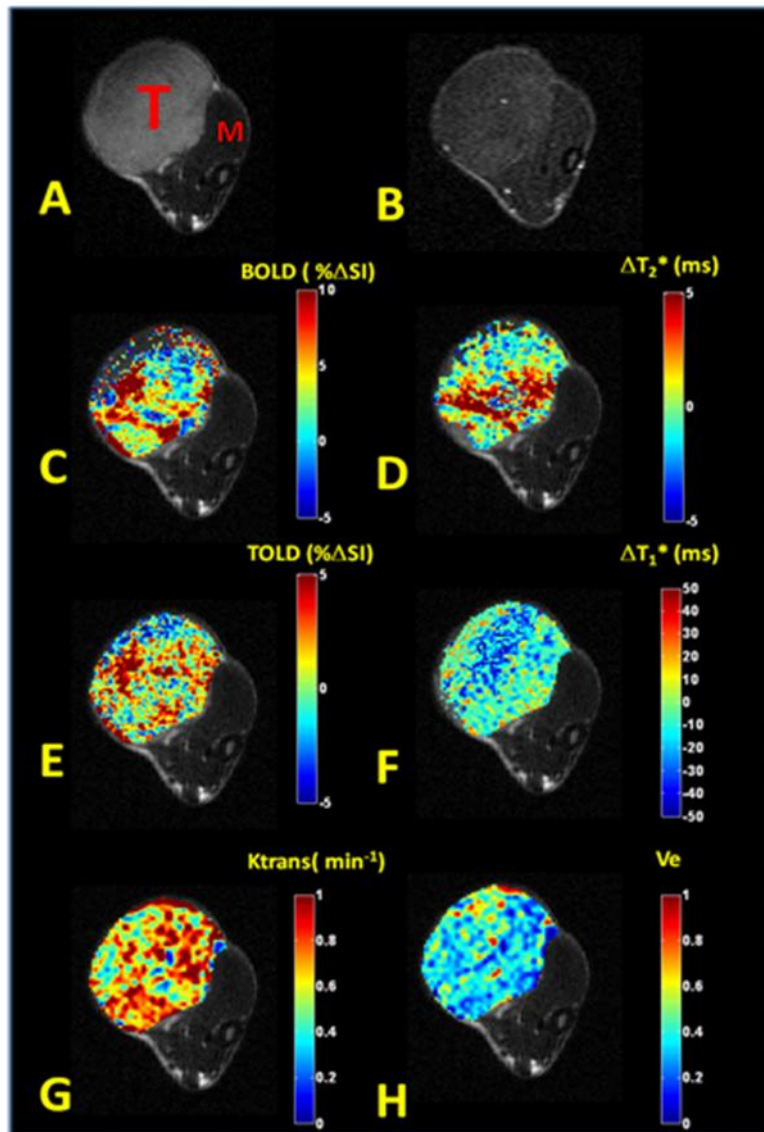


Figure 3-4 Oxygen sensitive MRI. A) High resolution T₂W image showing the tumor (T) and muscle (M). B) Post-contrast (Gd-DTPA) T₁W. C) BOLD, D) T₂*, E) TOLD, F) T₁, G) k^{trans} and H) v_e response maps overlaid on high resolution T₂W image of a Dunning prostate R3327-HI tumor (1.3 cm³) with respect to oxygen challenge or Gd-DTPA infusion.

For the AT1 tumors, growth was measured up to four times the initial tumor size or 80 days (Figure 3.5). One rat died before the tumor reached T_4 and this date was used as T_4 . Untreated controls had the fastest growth rate with a T_4 of 8 ± 1 days (Figure 3.6). The irradiated tumors showed significantly slower growth rates with $T_4 = 39 \pm 11$ days (Group 2b) and 50 ± 18 days (Group 2c).

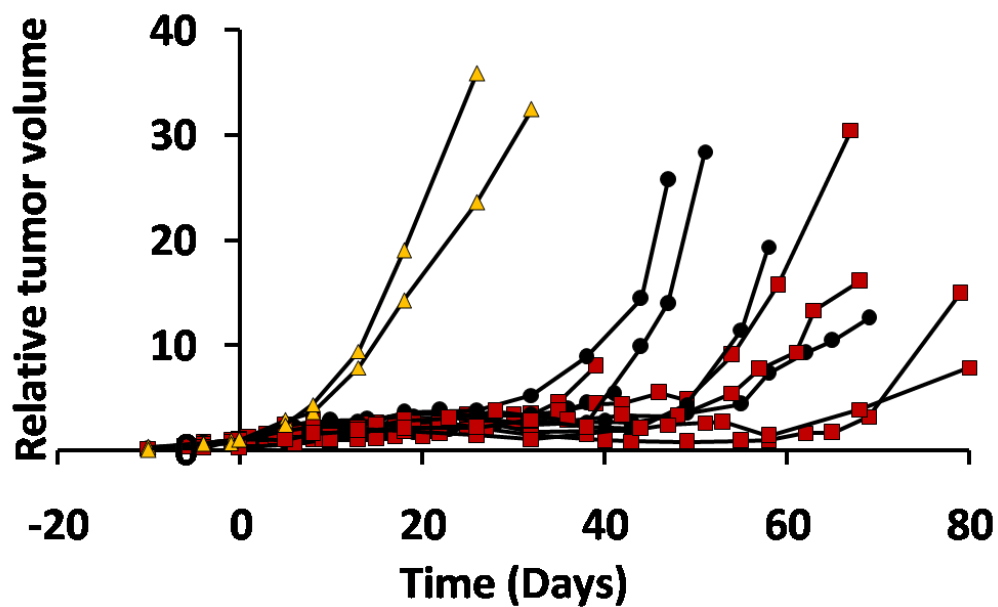


Figure 3-5 Influence of radiation on Dunning prostate R3327-AT1 tumor growth. Growth curves for the 13 individual AT1 tumors: sham-irradiated tumors (Group 2a, $n=2$, yellow filled triangles), and single dose 30 Gy, while rats breathed air (Group 2b, $n=5$, filled circles) or oxygen (Group 2c, $n=6$, red filled squares)

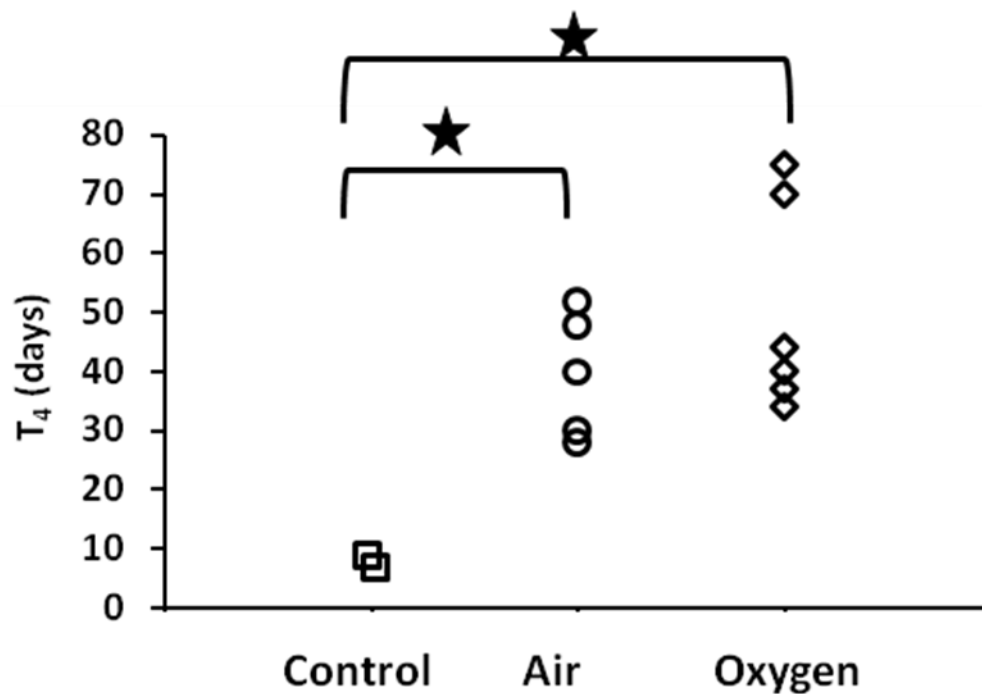


Figure 3-6 Tumor growth delay for 13 AT1 tumors. Effect of air and oxygen breathing on radiation response assessed by time for tumor to quadruple in size (T₄) * p<0.01.

The AT1 tumors showed a correlation between T₄ for the animals breathing O₂ during radiation and pre-irradiation TOLD responses to oxygen challenge (%ΔSI, Figure 3.7A) or T₁ relaxation times (Figure 3.7B): R²> 0.78; p<0.05. Group 2C tumors could also be stratified by magnitude of response where large responders (ΔSI > 1.5%; [T₁(air)-T₁(oxy)] >0.02 s) showed significantly larger T₄ ~70 days vs. 35 days (p< 0.05). No such correlation was seen for semi-quantitative ΔSI BOLD or quantitative R₂* responses. No correlations or stratification were found with respect to volume doubling time (T₂).

Similarly for HI tumors, growth was measured up to four times the initial tumor size or 35 days (Figure 3.8). Untreated controls had the fastest growth rate with a T_4 of 9 ± 5 days (Figure 3.8). The irradiated tumors showed significantly slower growth rates with $T_4 = 17\pm 1$ days (Group 2b) and 25 ± 6 days (Group 2c). In addition, a similar stratification to that seen in the AT1 tumors was found in the HI tumors; i.e. tumors with large TOLD response ($\Delta SI > 1.0\%$; $[T_1(\text{air})-T_1(\text{oxy})] > 0.015$ s) showed significantly larger $T_4 \sim 35$ days vs. 17 days. Contrary to the AT1 tumors, HI tumors also showed correlation between BOLD/ T_2^* and T_4 , although this correlation might be biased by the small number of animals ($n=3$).

AT1 and HI tumors were subjected to DCE to investigate whether K^{trans} and v_e maps can differentiate between responsive and nonresponsive tumors. DCE was successful in 8 out of 11 AT1 tumors and 4 out of 6 HI tumors of those which received radiation. The K^{trans} and v_e maps (Figures 3.2, 3.3 G&H) were heterogeneous with highest values in the periphery. K^{trans} ranged from 0.03 to 0.18 min^{-1} (mean= $0.11\pm 0.05 \text{ min}^{-1}$) in AT1 tumors, while 0.05 to 0.14 (mean= $0.08\pm 0.04 \text{ min}^{-1}$) in HI tumors. On the other hand, v_e ranged from 0.07 to 0.36 (mean 0.19 ± 0.09) in AT1 tumors and 0.23 to 0.38 (mean 0.30 ± 0.06) in HI tumors. The AT1 tumors showed a correlation between T_4 for the animals breathing both air and O_2 during radiation and pre-irradiation v_e measurement (Figure 3.9 $R^2 > 0.72$; $p < 0.05$). No correlation was observed in terms of k^{trans} and T_4 ($R^2 < 0.3$).

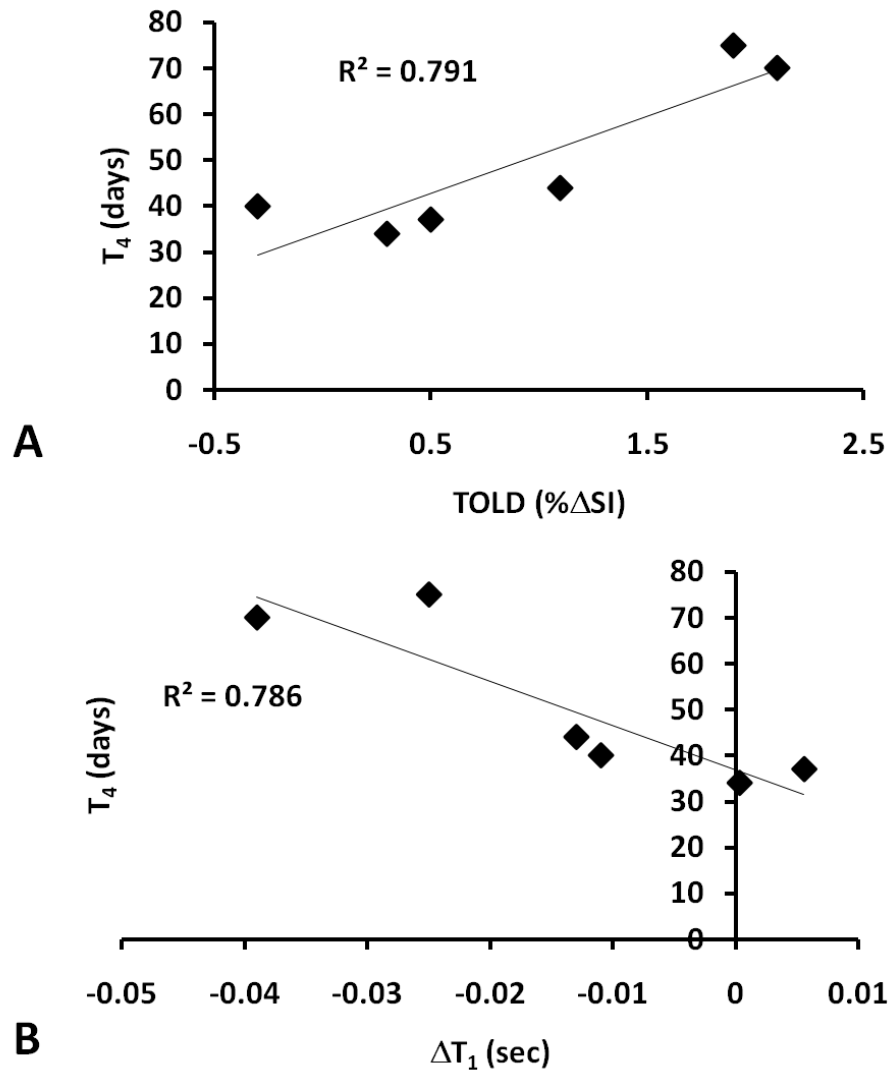


Figure 3-7 Tumor volume quadrupling time (T_4). Correlation between (T_4) and A) TOLD or B) ΔT_1 for those AT1 tumors irradiated during oxygen breathing (n=6).

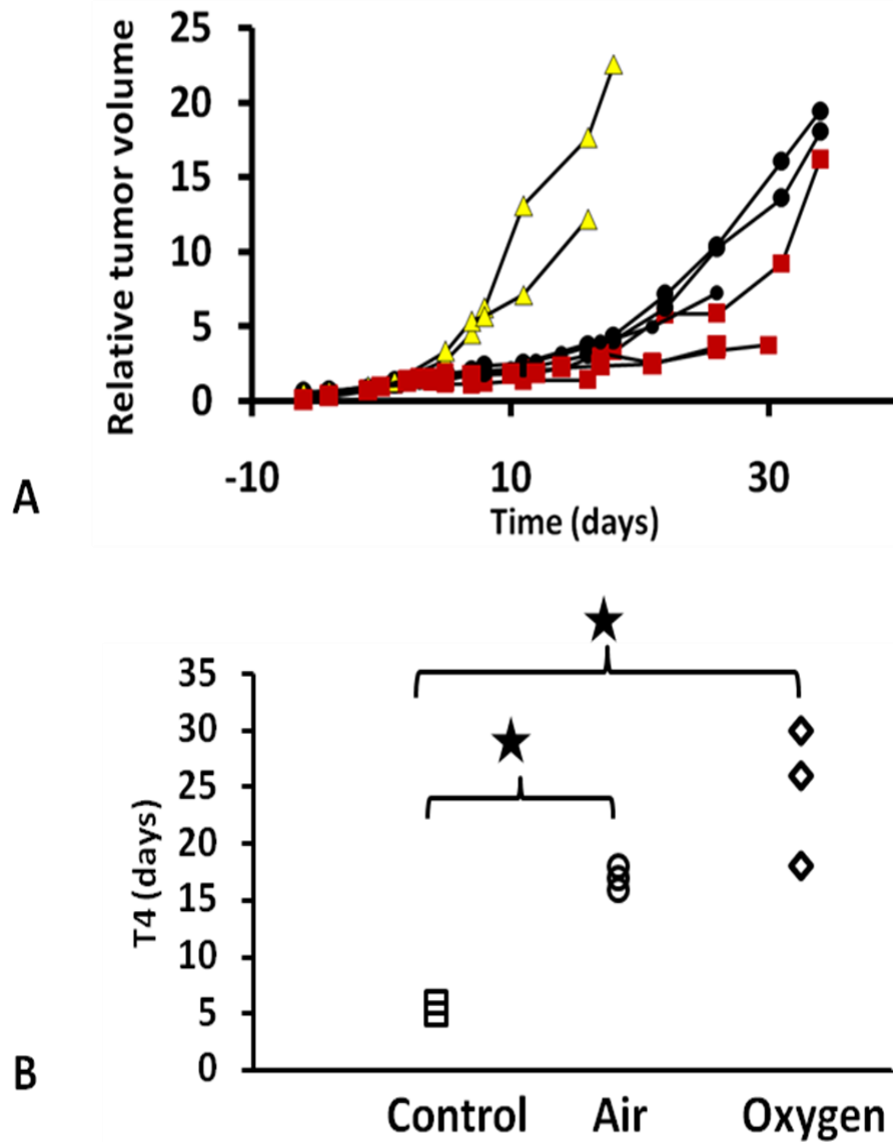


Figure 3-8 Influence of radiation on Dunning prostate R3327-HI tumor growth. A) Growth curves for the 8 individual HI tumors: sham-irradiated tumors (Group 2a, n=2, yellow filled triangles), and single dose 30 Gy, while rats breathed air (Group 2b, n=3, filled circles) or oxygen (Group 2c, n=3, red filled squares). B) Effect of air and oxygen breathing on radiation response assessed by time for tumor to quadruple in size (T4) * $p < 0.05$.

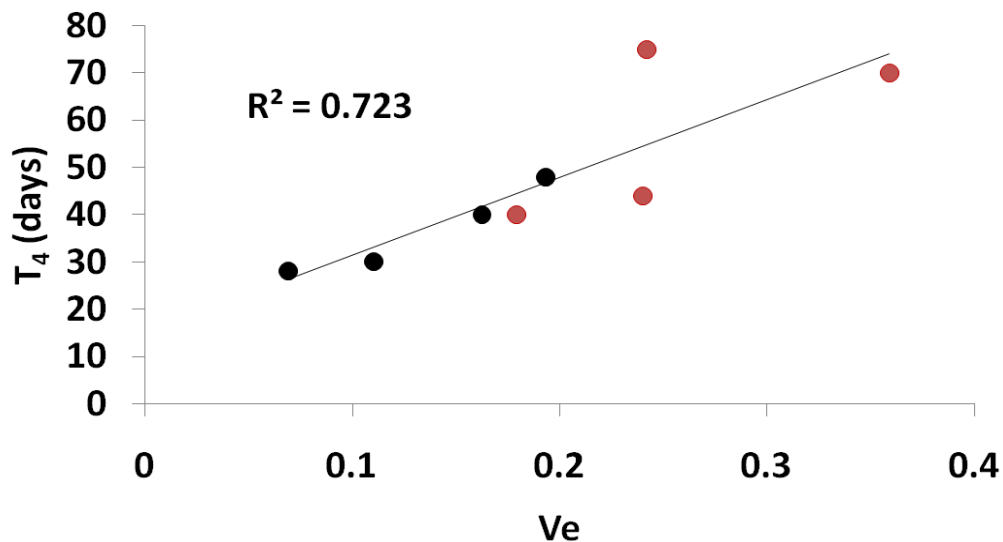


Figure 3-9 Tumor volume quadrupling time (T_4) for AT1 tumors. Correlation between (T_4) and v_e for those tumors irradiated during oxygen (red, $n=4$) and air (black, $n=4$) breathing.

3.5 DISCUSSION

Correlation between oxygen sensitive parameters is of interest, but ultimately the ability to predict therapeutic response is vital. As such the observation that tumors exhibiting significantly greater TOLD response (ΔT_1 and ΔSI) had significantly longer tumor growth delay is promising. Specifically, those tumors showing small TOLD response to oxygen challenge (<1.5 in % ΔSI ; <150 ms reduction in T_1) showed no benefit compared with tumors in air-breathing rats. Binary stratification may be valuable in terms of defining the utility of O_2 -breathing during irradiation. It is also interesting to note the direct linear

relationship between the time to quadruple in size (T4) and $\% \Delta SI$ or ΔT_1 (Figure 3.7A, B). A very similar result was reported in orthotopic C6 gliomas in rats subject to single high dose irradiation [142]. I found no correlation between BOLD response and tumor growth delay in the Dunning prostate R3327-AT1 tumors. A previous report found that GH3 prolactinomas growing in rats showed a significant BOLD response with respect to CB breathing challenge and experienced increased tumor growth delay in response to single dose radiation while breathing CB [68]. By contrast, RIF-1 fibrosarcomas tumors showed minimal BOLD response and no benefit from breathing CB.

A linear correlation was also observed between v_e and T4. Those tumors showing large v_e fraction showed larger delayed growth than those with lower v_e fraction regardless of gas breathing during irradiation. Similar result were reported for various xenografts (R-18, U-25, and V27 melanoma) growing in adult female BALB/c nu/nu mice [143]. A linear correlation was observed between v_e and the survival fraction based on 10 Gy IR (SF10) under air breathing conditions [143]. The correlation between v_e and T4 may be explained by the larger extracellular extravascular space in the tumor, and therefore, less cellular density and oxygen consumption. In fact, TOLD showed a strong correlation with v_e ($n=8$, $R^2>0.54$, $p<0.05$).

Several factors affect the development of hypoxia in tumors including vascularity of the surrounding normal tissue, angiogenic factor secretion and the oxygen consumption of tumor cells [144, 145]. The AT1 tumor line is anaplastic undifferentiated and is moderately responsive to oxygen challenge. On the other hand, the HI includes extensive mucinous acini with rapid large response to modulation. Therefore, the intention behind studying the two tumor sublines (AT1 and HI) was to have significantly different tumor properties to allow comparison. Unfortunately, the HI tumor line appears to have drifted over the years and the results were not as expected. Little to no BOLD response was observed in the HI tumors upon oxygen challenge (Chapters 2 and 3) compared to previous observations in Dr. Mason's lab [146]. In various cases, a large necrotic region was observed in the center of the tumor. In addition, unexpected lung and abdomen metastasis was observed in this tumor line (Figure A1.2). By the end of this study, no further HI tumors could be grown, which is the reason of having smaller number of animals with this tumor line.

Currently most patients receive fractionated radiation therapy (CFRT), but hypofractionated regimens are gaining popularity due to significantly higher tumor response rates, the efficiency of fewer patient visits, opportunity for better treatment planning and development of enhanced targeting. Furthermore in specific tumors SBRT (stereotactic body radiation therapy) has been found to provide significantly enhanced outcome [147]. It is expected that hypoxia may

influence each dose with little opportunity for the progressive reoxygenation thought to accompany CFRT [148]. As such IMRT (intensity modulated radiation therapy) and adjuvant administration of hypoxic cell selective cytotoxins could be considered [149].

There have been many attempts to assess tumor hypoxia and alter tumor hypoxia prior to radiation and chemotherapy to enhance therapeutic efficacy. Approaches, as simple as inhalation of hyperoxic gases, have been successful in preclinical models [97, 111], but translation to the clinic has shown marginal efficacy [19]. It is suggested that the general lack of success has been inability to identify those tumors (patients) that would benefit from modified therapy. Therefore, assessment of tumor hypoxia and the ability to perform *in vivo* imaging should provide useful prognostic information. Stratifying patient tumors based on hypoxia is particularly timely since there are increasing opportunities to tailor therapy to tumor characteristics, potentially enhancing success through personalized medicine. Thus, there is a true need for prognostic biomarkers to identify hypoxia in human tumors and many diverse modalities and reporter molecules are under evaluation [19, 150].

3.6 CONCLUSION

These results provide further insight into the relationships between oxygen sensitive MRI parameters and indicate that response to hyperoxic gas challenge is related to radiation response. Studies hitherto have focused on pre-clinical models of prostate cancer notably in rats. The data provide rationale for expanding the studies to other tumor sites and progressively patients. Since the method is entirely non-invasive it should permit ready translation to clinical patients.

Acknowledgments

Supported in part by grants from the NIH NCI (R01 CA139043) and infrastructure provided by the Southwestern Small Animal Imaging Research Program (SW-SAIRP) supported in part by 1U24 CA126608, Simmons Cancer Center (P30 CA142543) and AIRC (NIH P41 RR02584). The small animal irradiator was purchased with funds from a Shared Instrumentation grant S10 RR028011. Investigations were facilitated by the expert technical assistance of Dr. Peter Peschke and Marisela I. Aguilera.

CHAPTER FOUR

Oxygenation in Cervical Cancer and Normal Uterine Cervix Assessed Using BOLD MRI at 3 T

4.1 ABSTRACT

Hypoxia is reported to be a biomarker for poor prognosis in cervical cancer. However, a practical non-invasive method is needed for routine clinical evaluation of tumor hypoxia. This study examined the potential use of BOLD contrast MRI as a non-invasive technique to assess tumor vascular oxygenation at 3 T. Following IRB-approved informed consent and in compliance with HIPAA successful results were achieved in nine patients with locally advanced cervical cancer (FIGO stage IIA to IVA) and three normal volunteers. In the first four patients, dynamic T_2^* -weighted MRI was performed in the transaxial plane using a multi-shot EPI sequence, while patients breathed room air followed by oxygen (15 dm³/min). Later, a multi-echo gradient echo examination was added to provide quantitative R_2^* measurements. Baseline T_2^* -weighted signal intensity was quite stable, but increased to various extents in tumors upon initiation of oxygen breathing. Signal in normal uterus increased significantly, while iliacus muscle did not change. R_2^* responded significantly in healthy uterus, cervix, and eight cervical tumors. This preliminary study demonstrates that BOLD MRI of

cervical cancer at 3T is feasible. However, more patients must be evaluated and followed clinically before any prognostic value can be determined.

4.2 INTRODUCTION

Routine PAP smears have reduced the incidence of advanced cervical cancer and vaccines promise further long-term benefits, but currently cervical cancer remains a prevalent life-threatening disease. Many patients fail to respond to treatment, especially those who present at advanced stage with large tumor mass. While tumor size can be assessed non-invasively, invasive electrodes have been required to measure oxygenation. Several studies using the Eppendorf Histogram needle electrode system for various disease sites have shown that tumor hypoxia was associated with poor prognosis, notably for head and neck cancer, prostate, and lung [23, 24, 151]. The most extensive studies have been applied to cervical cancer, revealing both extensive hypoxia and more rapid rates of recurrence for large hypoxic tumors in node negative patients [13, 14, 134]. Patients with recurrent cervical cancers experience dismal survival rates, and thus, there is active interest in developing radiologic imaging methods to identify hypoxia. Preliminary studies using PET following the administration of the hypoxia reporter Cu-ATSM indicate correlation between uptake at 1 hour and progression free survival up to two years [152]. Other studies indicate that

pharmacokinetic DCE CT or MRI parameters correlate with hypoxia determined using electrodes in groups of human cervical tumors [84, 153, 154]. Semi quantitative analysis of rat tumors comparing DCE and BOLD in Dr. Mason's lab showed correlation in some individual tumors, but not others [62], and lack of correlation was reported for quantitative analysis of mouse tumors by Baudelet et al. [155].

In this study I examined the feasibility of adding the BOLD contrast imaging sequence to standard MRI examinations of patients with cervical cancer; I describe the evolution of a method that is now both robust and clinically practical.

4.3 EXPERIMENTAL

This study was approved by the Institutional Review Board and complies with the Health Insurance Portability and Accountability Act (HIPAA). Examinations were performed using a 3T MR scanner (Achieva, Philips Medical Systems, Cleveland, OH) following consent. Three healthy volunteers were examined as well as 10 patients: 8 with invasive cervical squamous cell carcinoma (SCC) and 2 with invasive adenocarcinoma (patients 8 and 9). Two of the ten patients were found to have metal clips. Tumor size was estimated from the high resolution MR planning images. The patients' median age was 44 years

(range 36 to 56 years) with FIGO stage IIA to IVA. Hematocrit ranged from 33.2% to 41.1% with no obvious trend with respect to disease extent or BOLD response. For the first volunteer and first four patients data were acquired in the transaxial plane as follows:

- Anatomical high resolution T_2 weighted (T_2W) images: TR/TE = 6,700/130 ms, FA 90° , FOV = 180 mm, matrix size = 340x309, slice thickness= 4 mm.
- Axial T_2^*W images during air breathing and oxygen breathing (30 images in 8 mins.): Multiple-Shot EPI was used with the following parameters: TR/TE = 500/41 ms, FA = 70° , FOV = 220 mm, matrix size = 240x240, slice thickness= 5 mm, EPI factor=7, number of averages=2.

For volunteers two and three and the later patients, the BOLD study was performed in the sagittal plane, instead of axial plane, and included quantitative R_2^* measurements. The data were acquired as follows:

- Anatomical high resolution T_2W images: TR/TE = 6,700/130 ms, FA = 90° , FOV = 180 mm, matrix size = 340x309, slice thickness = 4 mm.
- Sagittal T_2^*W images during air breathing (8 images in 2 mins) and oxygen breathing (22 images in 8 mins): based on Multiple-Echo Gradient Echo (MGRE) sequence: TR = 65 ms, FA = 30° , FOV = 300 mm, matrix size = 240x240, thickness = 5 mm, 1 slice. Echo Time (TE) was arrayed

with 16 echoes using minimum TE = 2 ms and Δ TE = 2.5 ms to generate the R_2^* maps.

Images were acquired using a 6-element SENSE body coil. Patients and volunteers were examined during room air breathing followed by 100% oxygen (15 dm³/min.), which was administered via a face mask (adult oxygen mask, CareFusion, France) that was worn throughout the experiment. Arterial pressure of oxygen (SaO₂) and heart rate were monitored throughout the experiment using a pulse oximeter (*In vivo* 4500 MRI, *In vivo* Research Inc., Orlando, FL).

4.3.1 Data Analysis

BOLD MRI data analysis was performed using programs written by me in Matlab (MathWorks Inc., Natick, MA). Regions of interest (ROIs) were determined by a board certified radiologist with over eight years experience in body-MRI. The dynamic multi-shot EPI sequence allowed the measurement of tumor response to oxygen challenge by calculating changes in signal intensity within the ROI selected for the tumor (ROIs were verified by a board certified radiologist with over 10 years experience in MRI, Dr. Robert D. Sims). Signal intensity change was calculated as in Equation 2.1. In addition, signal change was also evaluated in the iliacus muscle.

Data acquired using a multi-echo GRE sequence allowed R_2^* maps to be generated by fitting the multi-echo T_2^* -W image signal intensity to TE, as a single exponential function on a voxel-by-voxel basis, as in Equation 4.1.

$$SI = S_o \cdot e^{-TE/T_2^*} \quad \text{Equation 4.1}$$

The change of R_2^* due to oxygen challenge was then calculated as in equation 2.3. As a rudimentary comparison with initial studies where only a single echo was acquired, the signal intensity was recorded at the closest time in the multi-echo series (TE = 39 vs. 41 ms earlier) to provide ΔSI . Normal uterine tissue was used as a reference.

4.3.2 Statistical Analysis

The mean SI of the T_2^* -W images during air breathing was calculated for each ROI and compared with mean SI of the T_2^* -W images during oxygen breathing. Initially, the data were segmented into two-minute time increments to assess dynamic changes. The response to challenge was significant within 4 minutes after oxygen breathing in seven out of nine patients. However, it was challenging to determine the steady state region for every patient. Therefore, an average of all data points was used to determine the response to challenge. Student's t-tests were performed to examine changes in signal intensity and R_2^* response to oxygen breathing ($p < 0.05$ was considered significant).

4.4 RESULTS

The ten patients and three normal volunteers tolerated the oxygen breathing challenge without any adverse events. Metal clips adjacent to the cervix of one patient caused severe artifacts and these data were excluded from analysis. In a second patient such artifacts obscured part of the tumor, but the remainder was analyzable. In response to breathing oxygen mean arterial oxygen saturation was found to increase significantly from 97 ± 1 to 99% ($p < 0.05$). Pulse rate ranged from 71 to 99 bpm during baseline air breathing and 64 to 94 with oxygen, which was not significantly different.

Data acquisition was successful in the first volunteer and results are presented for cervix and uterus in Table 1. In the first patient, filling of the bladder displaced the tumor from the selected transaxial imaging plane between the time of initial planning and the oxygen sensitive BOLD contrast study. No further displacement was seen during the BOLD challenge, but the BOLD data were consequently obtained for a slice including only tumor periphery, to which I attribute the particularly large BOLD signal response ($\Delta SI > 21\%$, Table 4.1). Transaxial images obtained using the initial protocol showed well defined anatomy (e.g., Patient #3 in Figure 4.1A), allowing regions of interest to be identified in the multi-shot EPI (Figure 4.1B). T_2^*W signal response (ΔSI) is shown on a voxel-by-voxel basis in the color overlay map (Figure 4.1C),

revealing considerable heterogeneity in response to oxygen breathing. The signal dynamics are shown for muscle and tumor respectively (Figure 4.1D), indicating a significant increase in SI in the tumor upon oxygen challenge ($\Delta SI = 5.4\% \pm 3.1\%$; $p < 0.05$), whereas little change was observed in muscle ($\Delta SI = -0.2 \pm 2.5\%$). The difference is emphasized in the histograms showing voxel-wise distribution of response (Figure 4.1E). A significant increase in T_2^* -weighted signal was seen in the tumors of all patients (#1-4) evaluated using the EPI approach, while only one patient had a significant change in muscle (Table 4.1). Sagittal orientation was used for subsequent investigations to compare BOLD response in both the cervical tumor and uterus, and to avoid interference attributed to bladder filling.

Images obtained in the sagittal orientation are shown for the second volunteer with respect to the oxygen challenge (Figure 4.2). Anatomy is shown in a central slice allowing regions of interest to be selected. Baseline echo planar images were acquired while the subject breathed ambient room air for 2.5 minutes followed by oxygen. ROIs were selected for normal uterus and cervical tissue (Figure 4.2B). Both tissues showed significant signal increase ($p < 0.05$) with a much greater signal response in the uterus ($\Delta SI = 25.4 \pm 3.8\%$) compared to normal cervix ($\Delta SI = 8.6 \pm 2.4\%$) (Figure 4.2 C and D). However, EPI in the sagittal plane failed in volunteer #3, showing considerable artifacts due to tissue interfaces in the bowel regions. To avoid such artifacts an MGRE sequence was tested, found to be successful and adopted for the subsequent patients.

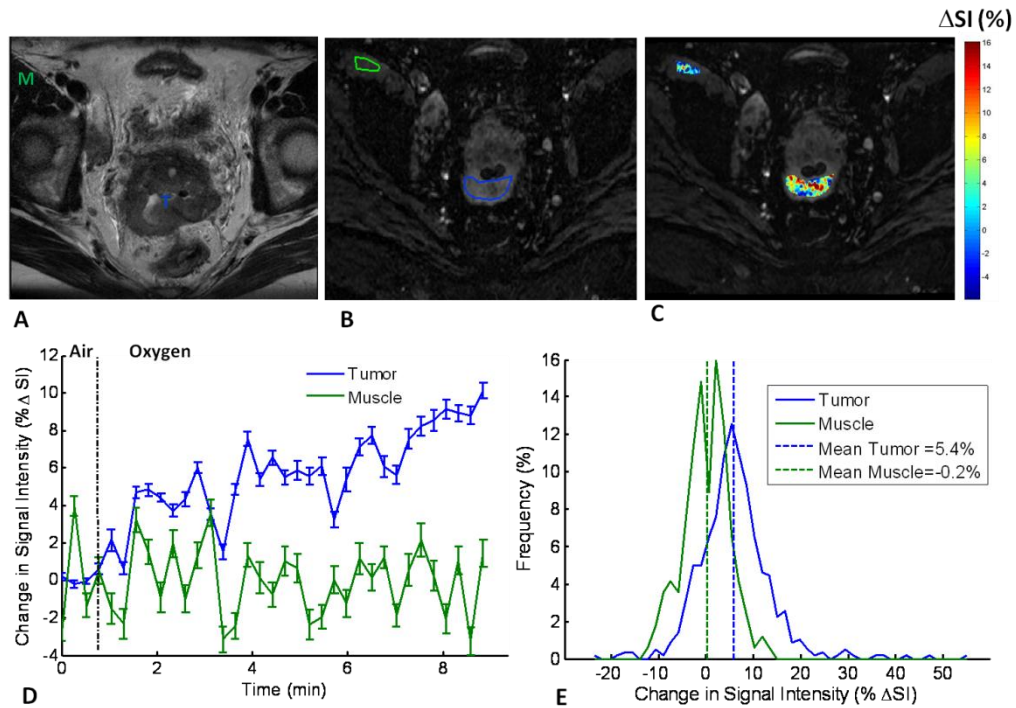


Figure 4-1 Blood oxygen level-dependent (BOLD) MRI of cervical tumor in the axial plane. A) High-resolution T₂ weighted image showing cervical tumor (T) for Patient 3. B) T₂* weighted image obtained using multi-shot echo planar imaging as part of a dynamic dataset with regions of interest for tumor and iliacus muscle outlined in blue and green, respectively. C) Maps of the percentage change in signal intensity (%ΔSI) for the tumor and muscle overlaid on the T₂* weighted image, showing the heterogeneity of response. D) Mean tumor signal response to oxygen breathing challenge (ΔSI= 5.4-3.1%) compared with muscle (ΔSI =-0.2-2.5%); vertical bars represent one standard error (SE) at each time point. E) Distribution of signal changes in tumor (blue) and muscle (green) with oxygen challenge.

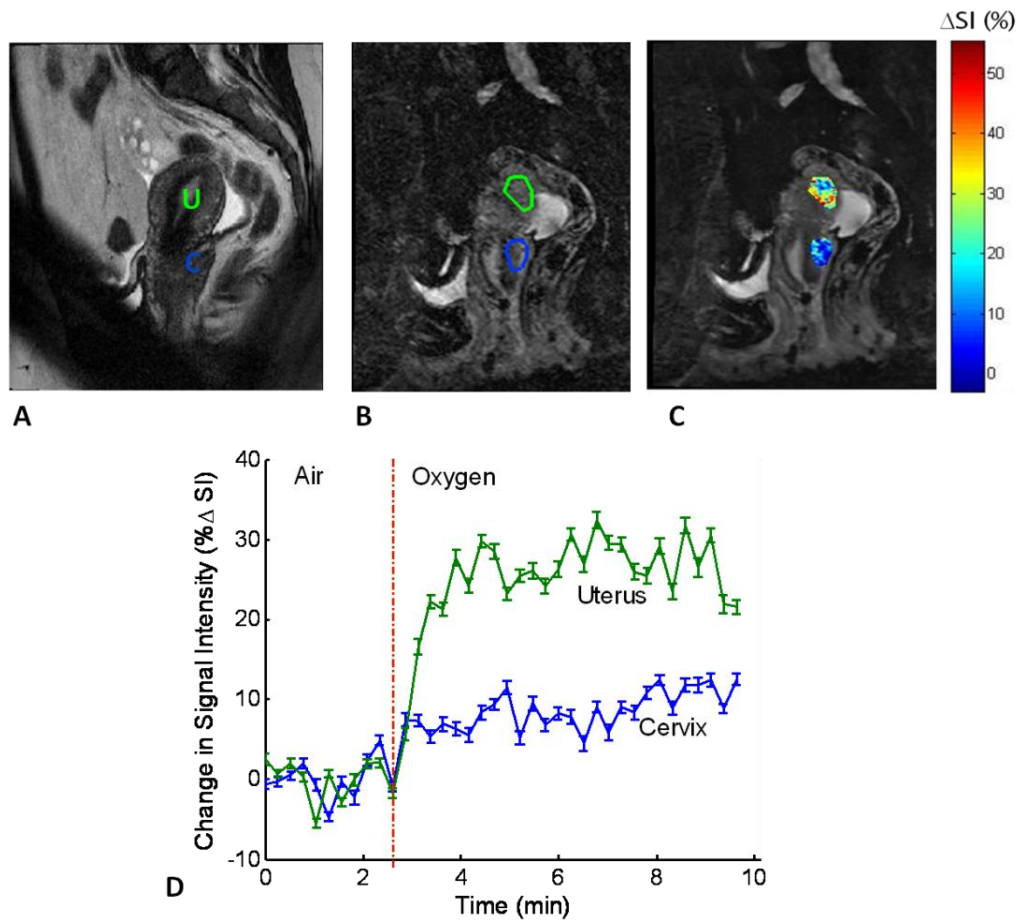


Figure 4-2 Sagittal imaging in a healthy volunteer with respect to oxygen challenge. A) High-resolution T_2W image showing the cervix (C) and vertically oriented uterus (U) for a normal volunteer (TR/TE = 6.7 s/130 ms; flip angle, 90° ; field of view, 180 mm; thickness, 4 mm). B) T_2^*W image obtained as part of a dynamic dataset. Regions of interest for normal cervical and uterine tissue are outlined in blue and green, respectively. Multiple-shot echo planar imaging (EPI) used: TR/TE = 500/41 ms; flip angle, 70° ; field of view, 22 cm; thickness, 5 mm. C) Color maps of the percentage change in signal intensity ($\% \Delta SI$) in the cervix and uterus overlaid on the T_2^*W image. D) Rapid significant signal response to oxygen breathing was observed in the uterus ($\Delta SI = 25.4 \pm 3.8\%$) and cervix ($\Delta SI = 8.6 \pm 2.4\%$). Each point represents the mean value \pm standard error (SE).

Substantial decreases in R_2^* rates were found with oxygen breathing in the third healthy volunteer (Figure 4.3). Mean signal intensity with respect to successive echoes at different TE values indicated highly consistent data allowing good curve fits to a mono-exponential function ($R^2 > 0.997$, typically) during air and oxygen breathing for both the cervix and uterus (Figure 4.3C). Each tissue showed a considerable range of R_2^* rates (10 to 50 s^{-1}) and a significant change with oxygen challenge ($R_2^* = 28.38 \pm 1.1$ decreased to 24.91 ± 0.8 or $\Delta R_2^* = -12.2\%$ in uterus, and $R_2^* = 29.47 \pm 1.2$ decreased to 26.65 ± 0.9 or $\Delta R_2^* = -9.6\%$ in cervix).

The multi echo gradient echo sequence was successfully applied to the subsequent five patients and representative data are shown for patient #8 (Figure 4.4). Individual voxels showed R_2^* ranging from 10 s^{-1} to 154 s^{-1} with a standard deviation ranging from 3 to 16 in an individual map of R_2^* at a single time point during air breathing. Repeated measurements during air breathing showed little variation in mean R_2^* rates for individual tumors with standard errors ranging from 0.1 to 0.4 s^{-1} and 0.2 to 0.3 s^{-1} for uterus. Rapid significant increase in signal was observed in both uterus ($\Delta SI = 8.3 \pm 1.3\%$) and in tumor ($\Delta SI = 1.1 \pm 1.7\%$; Figure 4.4G), although the response was considerably smaller in tumor. Corresponding R_2^* maps and fitted curves for the same ROIs showed that ΔR_2^* was faster in uterus ($\Delta R_2^* = -7.1\%$) than in tumor ($\Delta R_2^* = -1.1\%$; Figure 4.4H).

In this patient, muscle showed a small signal response to breathing oxygen ($\Delta R_2^* = 1.2\%$) with rates of $R_2^* = 40.32 \text{ s}^{-1}$ (air) and 42.84 s^{-1} (oxygen).

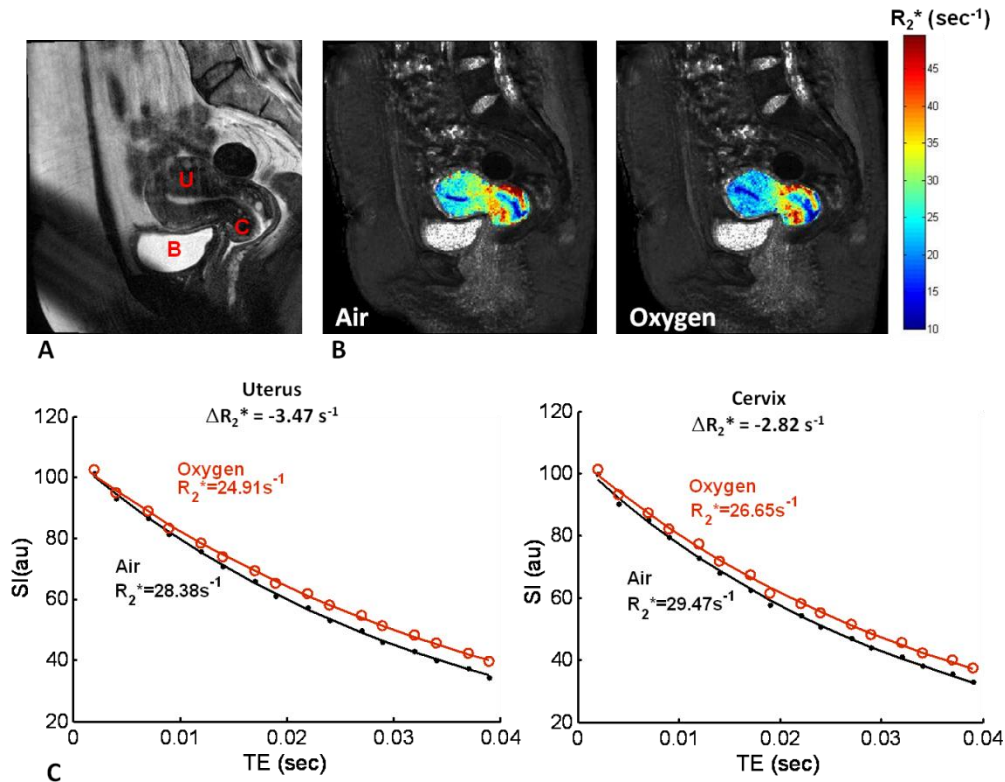


Figure 4-3 Changes in R_2^* in a healthy volunteer. A) High-resolution T₂W image (sagittal) showing the cervix (C) and normally positioned uterus (U) and bladder (B) for a normal volunteer (Volunteer 3) acquired using the same parameters as in Figure 4. 2a. B) R_2^* maps of the uterus and cervix overlaid on the T₂*W gradient echo image during room air and oxygen breathing, showing heterogeneity. C) Variation in the mean T₂*W signal intensity with TE values and mono-exponential fitted curves during air and oxygen breathing for both the cervix and uterus. Normal uterus showed a larger change in R_2^* compared with normal cervix with oxygen challenge (quantified as ΔR_2^*).

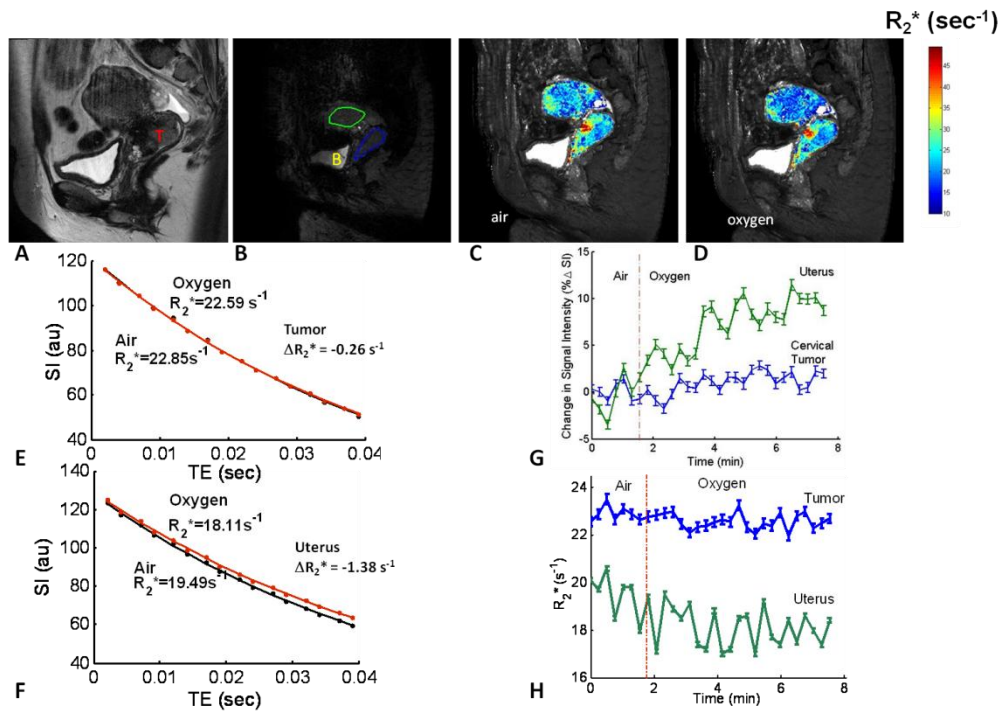


Figure 4-4 BOLD response to oxygen challenge based on changes in signal intensity (SI) and R_2^* . A) High-resolution T_2W image (sagittal) showing cervical tumor (T) in Patient 8. B) T_2^*W image obtained as part of a dynamic dataset with multiple-echo gradient echo (MGRE) imaging. Regions of interest (ROIs) are shown for tumor (blue) and normal uterus (green); B marks the bladder. C,D) R_2^* maps of the tumor and uterus overlaid on the T_2^*W image during room air and oxygen breathing. E,F) ROI-based T_2^* weighted signal decay measurements and fitted curves for tumor and uterus whilst the patient breathed air (black) and oxygen (red). Normal uterus showed a faster rate than tumor in mean R_2^* ($\Delta R_2^* = -1.38 s^{-1}$ versus $\Delta R_2^* = -0.26 s^{-1}$). G) Variation in mean relative signal response [\pm standard error (SE)] obtained from images at TE = 39 ms in MGRE for ROIs identified in (b) with respect to oxygen breathing challenge. Uterus (green) showed a larger mean signal response to oxygen breathing ($\Delta SI = 8.3 \pm 1.3\%$) relative to tumor (blue; $\Delta SI = 1.1 \pm 1.7\%$). H) Corresponding R_2^* (\pm SE) for cervical tumor (blue) and uterus (green) with respect to oxygen breathing challenge.

Several past investigations of BOLD response to hyperoxic gas challenge have reported changes in signal intensity only, and thus I compared the semi-quantitative ΔSI with R_2^* . Relative change in SI was closely related to relative change in R_2^* ($R^2 > 0.88$, $p < 0.0002$; Figure 4.5A) irrespective of tissue. Meanwhile change in R_2^* ($\% \Delta R_2^*$) was related to baseline R_2^* for tumor ($R^2 > 0.53$) (Figure 4.5B), but not uterus ($R^2 \sim 0.3$). Using the MGRE sequence, I was able to calculate the fitted constant (S_0) using $SI = S_0 \cdot e^{-TE/T_2^*}$. Change in S_0 ranged from -1% to 0.3% in the tumors and -0.2% to 1.4% in the uterus. Two of the negative tumor S_0 measurements were significant, as well as two positive S_0 changes in the uterus ($p < 0.05$).

Noting the progressive dynamic variation in signal and R_2^* for tissue, I conducted further analyses based on 2-minute time increments of oxygen challenge. Three tumors showed a significant response within the first two minutes of oxygen breathing; six of eight were significant by 4 minutes and 7 of 8 by 6 or 8 minutes. Since the kinetics were somewhat different, I showed mean values for the whole oxygen challenge breathing period in Tables 1 and 2.

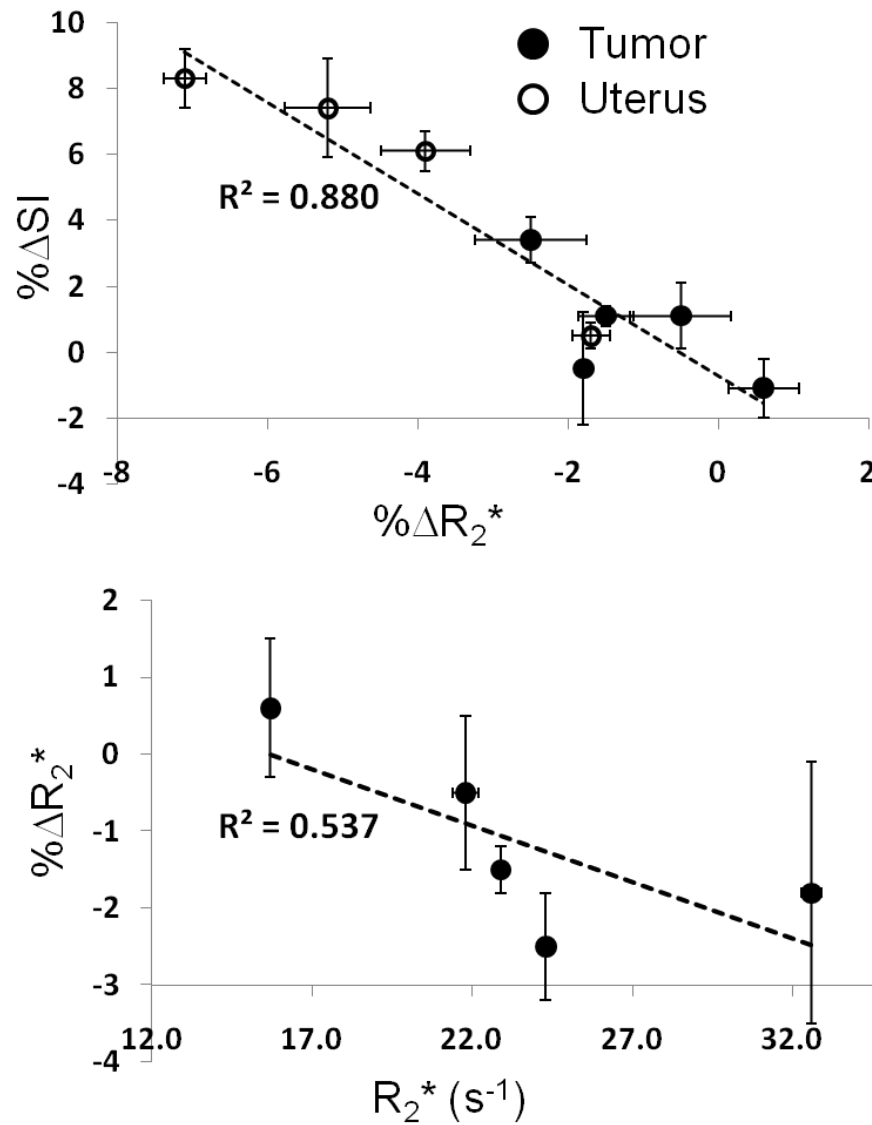


Figure 4-5 Comparison of semi-quantitative and quantitative BOLD response measurements. A) Relative change in signal intensity (SI) accompanying oxygen breathing challenge was closely related to the change in R_2^* irrespective of tissue [\circ , uterus (n=4); \bullet , cervical tumor (n=5); $R^2 > 0.88$, $p < 0.0002$). Data points represent mean \pm standard error (SE) for the whole oxygen challenge period. B) Change in R_2^* (% ΔR_2^*) was related to baseline R_2^* for the same five tumors shown as \bullet in (a) ($R^2 > 0.53$). Data points represent mean \pm SE for the whole oxygen challenge period versus baseline R_2^* .

4.5 DISCUSSION

BOLD contrast MRI was successfully accomplished in 9 of 10 patients with cervical cancer and three normal volunteers. The oxygen breathing paradigm was well tolerated and the only imaging failure was due to metal seeds implanted in the cervix for purposes of treatment planning.

Initial images were acquired in the transaxial plane since this has been traditionally favored as the primary imaging plane for cross-sectional diagnostic imaging of cervical cancer. Transaxial images generally allow for high resolution imaging to reveal parametrial tumor extension, and they also allow concurrent assessment of nodal involvement. For the BOLD response to oxygen challenge, a single plane was imaged through a central part of the tumor, as identified by the radiologist during the scanning procedure, so that both central and peripheral regions could be observed. Comparison of the high resolution diagnostic scans with BOLD provided anatomical identification, and muscle tissue was chosen as a reference standard. The iliacus muscle signal was quite stable both during baseline air breathing and in response to oxygen challenge (e.g., Figure 4. 1d). This coincides with previous reports in humans at 1.5 T, where oxygen breathing generated no response in R_2^* in muscle (or liver and spleen), while carbogen elicited a significant response in all three organs [119]. Likewise Winter et al. [156] reported a lack of response in rabbit paraspinal muscle at 1.5 T with respect

to oxygen challenge, though again carbogen induced a change. The differential response to these two hyperoxic gases is often attributed to vasoactivity of carbogen, and has been explored extensively with respect to tumor- and wound-induced skin angiogenesis [52]. The mature vasculature of well perfused muscle may show little response to oxygen. Meanwhile a large response has been reported accompanying the hyperemia in human muscle following constriction and ischemia [157].

Tumor showed distinct heterogeneity, but a significant mean increase in all four patients (Table 1). Three Patients showed quite similar signal response (2.7 to 5.4%), whereas Patient #1 showed a much larger change. It became clear that the tumor in Patient #1 had become displaced from the original imaging planning location. The tumor showed negligible displacement during the oxygen challenge, but the image plane now coincided with the tumor periphery instead of center due to bladder filling. The larger increase in BOLD response in this patient compared to the other three in this group is likely attributable to more extensive vasculature in the periphery as compared to the center. This artifact prompted us to alter the imaging acquisition plane for the later patients.

To date relatively few R_2^* tissue rates have been reported at 3 T. Cervical tumor and normal uterus showed quite similar rates around $R_2^* = 24 \text{ s}^{-1}$ (c.f. $T_2^* = 42 \text{ ms}$) (Table 2). By comparison human kidney is reported to have $T_2^* = 47 \text{ ms}$ with a significant response to oxygen breathing ($\Delta T_2^* \sim 1\text{-}2 \text{ ms}$ [158]), as seen in

the tissues here. Human skeletal muscle has been reported to have T_2^* around 27 ms at 1.5 T when subjects breathed air (unchanged with oxygen) [119]. A range of rates has been reported previously at 3 T, e.g., $T_2^* = 20 - 30$ ms in human tibialis anterior muscle and soleus muscle [159], which is very similar to the measurement in the paraspinal muscle ($T_2^*=24.8$ ms) here, though a value of $T_2^* = 19$ ms was reported for calf muscle [157].

Imaging in the sagittal plane avoids issues of displacement due to bladder filling and clearly shows the relationship of normal cervix or cervical tumor to the uterus and vagina. The well-vascularized endometrium provides a useful positive control, which is highly responsive to oxygen challenge (Figure 4.2). Echo planar imaging was less satisfactory in the sagittal plane due to signal losses from extensive susceptibility variations in the bowel regions.

For the later patients (#5-10), the multi-echo gradient echo sequence provided R_2^* , as opposed to sampling signal intensity changes alone. This should provide further insurance against artifacts, since R_2^* distribution may be compared irrespective of motion artifacts, which otherwise could compromise effective signal subtraction. R_2^* maps show heterogeneity in both the uterus and normal cervix (e.g., in Figure 4.3) with significant decrease in R_2^* upon breathing oxygen.

Two patients presented with surgical metal clips. Artifact from the metal clips obscured most of the tumor in Patient #7, which made it hard to analyze

(data excluded). Patient 5 also had a metal clip artifact that obscured part of the tumor. Nonetheless, a significant drop in R_2^* was observed upon breathing oxygen.

The motivation for developing oxygen sensitive MRI of human cervical cancer is provided by strong evidence that hypoxia influences tumor aggressiveness, notably angiogenesis and metastasis, as well as poor response to therapy and shorter recurrence free intervals. Specifically, in cancer of the cervix, several studies based on the Eppendorf Histogram polarographic electrode system, indicated that patients with hypoxic tumors (variously defined as $HF_5 > 50\%$ or median pO_2 less than the population mean) had a poorer clinical outcome. In 1998, Fyles, et al. [17], reported that cervical cancer patients with larger tumors (>5 cm diameter) had significantly poorer disease-free survival (DFS), if the fraction of pO_2 measurements less than 5 torr (~ 670 Pa) was greater than 50%, in a study of 74 patients (DFS 12% vs. 65% at 2 years, $P = 0.0001$). An extended study of 106 patients published in 2002 noted that the predictive value applied only to node negative patients [13] and a follow-up report indicates that stratification based on hypoxia is less relevant after 10 years [160]. Nonetheless, hypoxia was clearly associated with short-term disease free survival and this measurement could become a common and useful clinical tool, if accomplished with a simple non-invasive method.

In addition to assessing tumor hypoxia the dynamic response to an intervention may be important. Electrodes are highly invasive and do not conveniently allow repeat dynamic maps, although Aquino-Parsons et al. [161] did examine a group of women with respect to hyperoxic gas breathing challenge, comparing the influence of breathing oxygen or carbogen on cervical tumor pO_2 . Results indicated that carbogen was more effective at eliminating hypoxia than oxygen, but carbogen is noted to be quite stressful and thus oxygen breathing challenge was applied here. It has been reported that carbogen-light (98% O_2 /2% CO_2) causes less stress, while retaining the hemodynamic attributes of carbogen [162-164], and this appears worthy of future investigation for BOLD studies. Warming and humidifying the inhaled gas might be helpful.

BOLD MRI indicates changes in vascular oxygenation, but may be further influenced by flow, vascular volume, pH, R_1 changes, and hematocrit [46, 51]. I tested two pulse sequences to acquire BOLD images. Semi-quantitative approaches based on simple changes in T_2 -weighted signal intensity are particularly sensitive to flow [46], although this has been applied to many pre-clinical and clinical investigation [37, 51, 62, 65, 70]. Use of MGRE to assess R_2^* is relatively insensitive to inflow [46], although it has been favored in more recent studies [53, 55, 67, 68]. It is noteworthy that a strong correlation was observed between changes in SI and R_2^* (Figure 4.5A) suggesting that inflow and R_1 changes are not a major factor in response. Nonetheless, significant changes in S_0

were observed for two tumors and two uteri with respect to oxygen challenge. The S_0 changes may have been caused by changes in R_1 or vascular volume. A correlation was also found between ΔR_2^* and baseline R_2^* (Figure 4.5B), in line with a previous report for chemically induced spontaneous rat breast tumors [67].

Rates of tissue response may also provide useful insight into tumor perfusion and oxygenation. Tumors in Patients #3 and #8, shown in Figures 4.1 and 4.4 respectively, showed considerable increase, albeit with minor hiccups, in signal over the whole 8-minute oxygen challenge. Other tumors reached a plateau or maximum at an earlier time.

The EPI sequence is sensitive to susceptibility differences, which result in signal loss, limited spatial resolution, and image distortion. Indeed, EPI failed in volunteer # 3 and subsequent studies were performed using MGRE. This has the added bonus of providing both relative signal intensity changes and R_2^* . Relative SI changes were larger on the EPI sequence compared to the MGRE. Since different MRI parameters were in both sequences, a direct comparison between relative SI is not feasible.

BOLD response is sensitive to tumor vascular oxygenation as well as the extent of vasculature [46, 47]. Measurements of tissue R_1 therefore may be relevant, since they are directly sensitive to changes in pO_2 [74, 114]. While there is a small R_1 response to deoxyhemoglobin [165, 166], it will ultimately be useful to implement and evaluate interleaved BOLD and TOLD measurements. Indeed,

preliminary reports of well defined rat prostate tumors, as well as my studies in Chapters 2 and 3, indicate differential temporal response to T_1 - and T_2^* -weighted signal, presumably reflecting alteration in vascular oxygenation followed by diffusion of oxygen into the tumor tissues [127]. A preliminary report did show significant response in T_1 of cervical squamous carcinoma in response to oxygen breathing at 1.5T [119]. Further development of oxygen sensitive MRI of the cervix may usefully compare different gases, e.g., carbogen [52, 58, 61, 119], implementation of alternative oxygen delivery approaches and masks [167], and various pulse sequences [130, 168]. Dynamic contrast enhanced (DCE) MRI following infusion of paramagnetic contrast agents has also been reported to provide insight into tumor hypoxia [84, 153, 154]. Likewise, histological correlates could provide further insight into the nature of tumor hypoxia and perfusion [169]. In the initial protocol described here, emphasis was on optimizing the BOLD study, but including additional methods should be straightforward in the future.

4.6 CONCLUSION

Despite several decades of significant treatment advances for cervical cancer, it remains a prevalent life-threatening disease. As such development of accurate prognostic biomarkers will almost certainly improve and eventually

optimize and personalize therapy. This preliminary study demonstrates that BOLD MRI at 3-tesla is feasible for examining the potentially valuable biomarker of oxygenation seen in cervical cancer. It remains to be seen whether baseline R_2^* , signal response to hyperoxic gas breathing or a multi parametric comparison including additional parameters such as tumor size, and stage will be most useful. Further parameters such as vascular perfusion and permeability based on DCE, cellularity based on diffusion, and TOLD response to oxygen challenge may also be readily incorporated into a dynamic evaluation. More patients must be evaluated and followed clinically before the prognostic value of this non-invasive technique is determined.

Acknowledgments

This research was supported in part by The Mary Kay Ash Foundation and Harold C. Simmons Cancer Center through 1 P30 CA142543.

Table 4-1 BOLD response of cervical tumor, uterus, and iliacus muscle observed in EPI images based on T₂*-weighted signal response to breathing oxygen

	<i>FIGO</i>	<i>Age</i>	<i>Tumor size</i>	<i>BOLD response (%ΔSI ± SD)</i>		
	<i>Stage</i>	<i>(years)</i>	<i>(cm³)</i>	Tumor	Uterus	Muscle
Patient 1	IIIB	47	6.4*5.5*5.4	21.2% ± 9.7%† *		0.1% ± 1.9%
Patient 2	IIB	54	7.2*6.9*6.5	3.4% ± 1.7% *		0.1% ± 2.6%
Patient 3	IIIB	41	6.0*4.7*4.6	5.4% ± 3.1% *		-0.2% ± 2.5%
Patient 4	IVA	38	11.6*10.2*8.9	2.7% ± 2.4% *		1.7% ± 5.0% *
Mean		45		8.1±8.8%		0.4 ± 0.9%
Normal Volunteer				Cervix	Uterus	Muscle
1		NA		8.2%±2.1% *		-0.5%±1.4%
2**				8.6%±2.4% *	25.4%±3.8% *	

† signal from tumor periphery

*p <0.05 indicating significant change in signal.

** acquired in the sagittal plane

Table 4-2 BOLD response of cervical tumor, normal cervix, and uterus observed in the sagittal GRE images based on R_2^* and T_2^* -weighted signal response to breathing oxygen

	FIGO Stage	Age years	Tumor Diameter cm	BOLD response (% Δ SI \pm SD)		$R_2^* \pm$ SD (s^{-1}) (air/oxygen)		% $\Delta R_2^* \pm$ SD	
				Tumor	Uterus	Tumor	Uterus	Tumor	Uterus
Patient 5‡	IIA	48	5.7	-0.5 \pm 0.5	0.5 \pm 1.3*	32.6 / 32.0	24.3/ 23.9	-1.8 \pm 8.7*	-1.7 \pm 2.2*
Patient 6	IIB	40	8.6	-1.1 \pm 2.2*	N/A	15.7/ 15.8	N/A	0.6 \pm 4.0*	N/A
Patient 8	IIB	42	3.6	1.1 \pm 1.7*	8.3 \pm 1.3*	22.9 / 22.6	19.5/ 18.1	-1.5 \pm 1.5*	-7.1 \pm 4.1*
Patient 9	IIB	36	6.1	1.1 \pm 2.6*	7.4 \pm 2.2*	21.8/ 21.6	25.8/ 24.5	-0.5 \pm 3.9	-5.2 \pm 5.8*
Patient 10	IIB	56	7.5	3.4 \pm 3.5*	6.1 \pm 2.8*	24.3/ 23.7	28.2/ 27.1	-2.5 \pm 3.5*	-3.9 \pm 2.7*
Mean		44		0.8\pm1.6	5.6\pm3.0	23.5/ 23.1	24.5/ 23.4	-1.1 \pm1.1	-4.5 \pm2.0
Normal 3		NA		Cervix	Uterus	Cervix	Uterus	Cervix	Uterus
				5.7 \pm 1.6	7.6 \pm 2.4	29.5/26	28.4/24.9	-9.6 \pm 3.3	-12.2 \pm 4.2

‡ Patient #5 had a metal clip preventing effective analysis of long echo time (TE) images: therefore, the BOLD signal comparison was performed at 17 ms for this patient.

* $p < 0.05$.

N/A: the uterus was poorly recognizable in T_2^* -W images of this patient

CHAPTER FIVE: Extended Applications- Preliminary Studies of Oxygenation in Head and Neck, Lung, and Prostate Cancers Assessed Using BOLD MRI

5.1 INTRODUCTION

In preclinical investigations, I demonstrated the feasibility of oxygen sensitive MRI and in Chapter 4, I demonstrated application to human cervical cancer. However, for new disease site, feasibility and logistic preparation are vital. In this chapter, I will discuss the challenges of application of BOLD MRI in head and neck (H&N), lung and prostate tumors.

5.1.1 Head and Neck (H&N) Cancer

MRI of H&N tumors is challenging for several reasons: i) the air-tissue interface may lead to susceptibility artifacts, ii) swallowing creates motion and potential misalignment for image subtraction. Nevertheless, I have shown the feasibility of achieving good anatomical detail in the neck at 3T. A 16 channel SENSE NeuroVascular (NV) coil provided effective images. However, the coil fits snugly precluding use of traditional emergency room face masks and thus I needed an alternate solution. A cannula was feasible, but tests indicated it was quite uncomfortable due to the direct gas flow into the nasal cavity, especially at

high flow rates. The long pediatric face mask (Pediatric Elongated Oxygen Mask, Part #1042, Temecula, CA USA) is very slim and was comfortable on an adult face in the coil. Since it is open to the laboratory air, patients can initially simply breathe air. In a control study in the normal brain, it appeared that 4 dm³/min did not always elicit a response; whereas 8 dm³/min and 15 dm³/min gave consistent signal increases.

To date the European ARCON trial has been unique in identifying patients with hypoxic H&N tumors and evaluating the influence of hypoxia on therapeutic outcome [170]. It showed that patients with hypoxic tumors identified by measuring pimonidazole accumulation in tissue samples had poorer outcome with a traditional radiation protocol. However, better response was noted with the addition of nicotinamide and carbogen breathing during irradiation.

In this study, successful BOLD contrast MRI was performed in 10 patients (example Figure 5.1A). Significant signal response was seen in this tumor upon breathing oxygen (Figure 5.1B). I performed BOLD MRI studies using an oxygen challenge, whereas previous studies of H&N have used carbogen (95%O₂+5%CO₂) [171]. They also examined quantitative changes in R₂^{*}, as well as the changes in relative signal intensity presented here. They reported global response functions (GRF) with signal changes in the range 5 to 15% with considerable variability between patients.

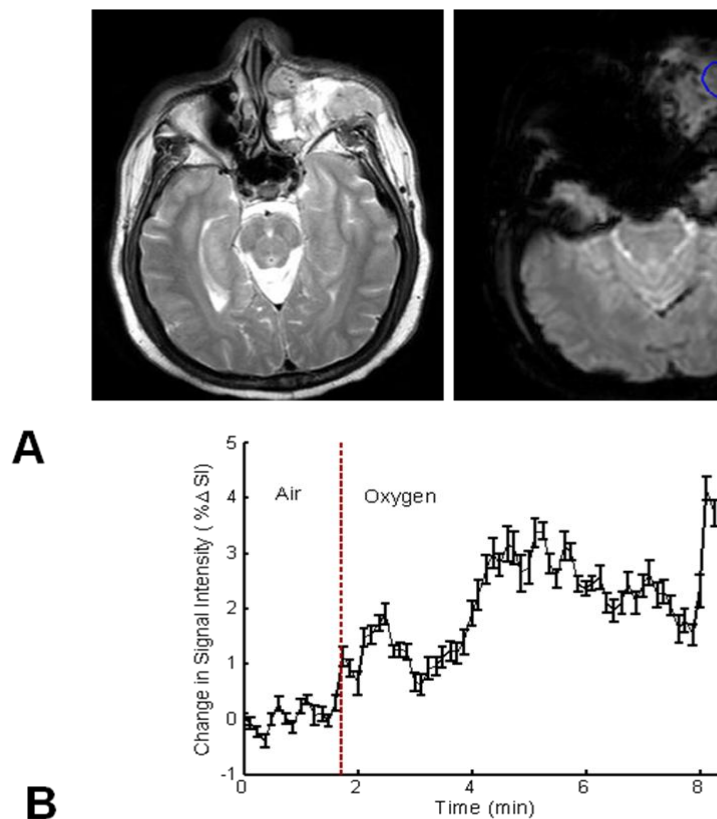


Figure 5-1 H&N cancer patient. A) Left: High resolution T₂-weighted image showing a large tumor near the maxillary sinuses region. Right: T₂*-weighted image (transaxial) obtained as part of a dynamic data set. B) Tumor showed significant BOLD response ($2.1\% \pm 0.9$) upon oxygen breathing.

5.1.2 Non-Small Cell Lung Cancer (NSCLC)

Significant progress has been made in early detection and therapy for non-small cell lung cancer (NSCLC). However, lung cancer remains the leading cause of cancer death. Better characterization of lung tumors will allow for individualized therapy. BOLD imaging of lung tumors is challenging due to

potential artifacts caused by blood flow, respiratory and cardiac motion, and the susceptibility effects of the surrounding lung tissue.

In this study, three patients with a biopsy proven non-small cell lung cancer were consented to participate. All studies were conducted with a 6-element SENSE cardiac coil on a 3T MR scanner (Achieva, Philips Medical Systems, Cleveland, USA). Patients wore a face mask for delivery of room air and oxygen at the beginning of the study. Respiratory-gated high-resolution T_2 weighted anatomical images were acquired during expiration to locate the tumor. Multi-echo gradient-echo technique with the same respiratory gate delay and gate width as anatomical scans was then used in BOLD study (16 echoes, minimum TE = 1.9 ms, Δ TE = 2.5 ms, TR = 65 ms, FOV = 24 cm, acquisition pixel size = 1x1 mm, slice thickness = 6 mm, 1 sagittal slice through the tumor). Dynamic T_2^* W BOLD images were obtained when patients breathed room air, then while breathing 100% oxygen at 8 L/min via the face mask (~ 1 min per dynamic scan, 3-4 dynamics during air-breathing, 6-8 dynamics during oxygen-breathing).

Figure 5.2 shows representative T_2 W and T_2^* W sagittal images obtained from a lung cancer patient. Voxel-by-voxel analysis demonstrates heterogeneous signal intensity change within tumor ROI between breathing air and oxygen (Figure 5.3A). ROI-based tumor BOLD kinetics in lung tumor in response to oxygen challenge is demonstrated in Figure 5.3B. In this patient, four T_2^* maps were acquired during air-breathing (~ 4 min), followed by six T_2^* maps acquired

during oxygen-breathing (~ 6 min). Figure 5.4 shows representative T_2^* maps during breathing air and oxygen.

The conventional EPI-based imaging technique used in cervical BOLD study in Chapter 4 did not yield good quality BOLD images of lung tumor, due to the artifacts from respiratory and cardiac/blood motion, and susceptibility effects of the surrounding lung tissue. Therefore, a multi-echo gradient-echo sequence was used to measure the BOLD response in this study. Breath-hold imaging was attempted in an effort to immobilize the lung tumor during imaging. However, difficulty was encountered due to variation in diaphragm/lung position during different breath-holds, as well as the fact that most of the lung cancer patients could not tolerate longer breath-hold attempts. Respiratory-gating was thus used to acquire images during expiration throughout the MRI exam to ensure the same anatomy was imaged, whereas sacrificing temporal resolution in the dynamic BOLD study.

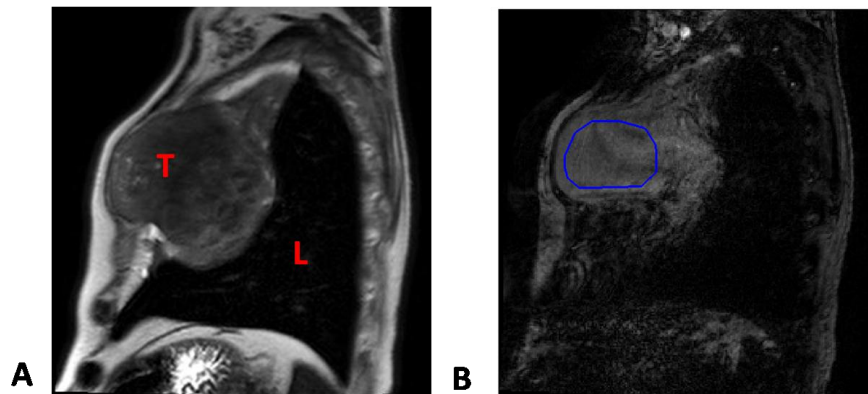


Figure 5-2 MRI of patient with large lung tumor. (A) T₂-weighted sagittal MR image of patient showing the lung (L) and large tumor (T). TR/TE = 3000/136 ms, FOV = 240 mm. (B) Sagittal T₂*-weighted dynamic image for the same patient showing the selected region of interest for the lung tumor. TR/TE = 65/22 ms FOV=240 mm Flip angle 30°.

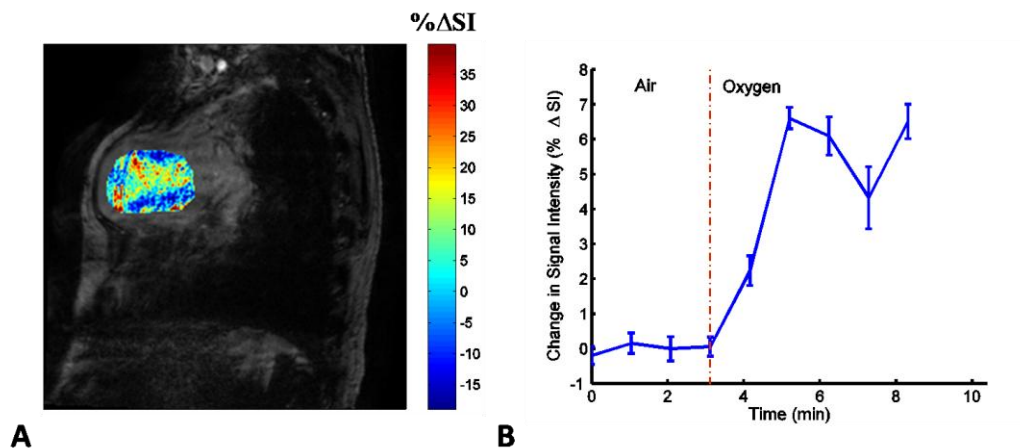


Figure 5-3 BOLD kinetics in lung tumor from the same patient in Figure 1. (A) Color map showing the absolute signal intensity change after breathing 100% oxygen. (B) Relative signal intensity change (%ΔSI) of tumor responded to patient breathing 100% O₂.

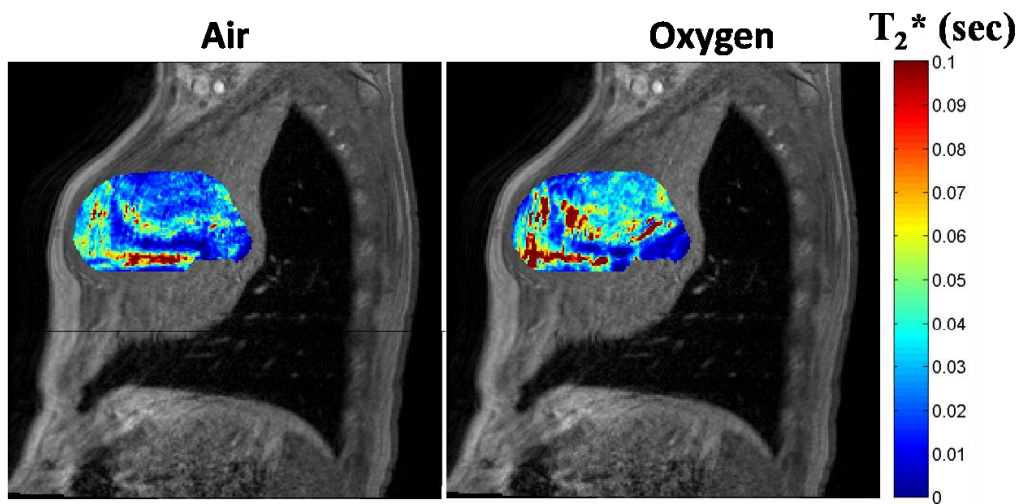


Figure 5-4 T_2^* maps of tumor ROI. T_2^* color maps show the heterogeneous T_2^* value within tumor ROI while breathing air (left) and oxygen (right).

5.1.3 Prostate cancer

Prostate cancer remains the most common malignant tumor in men. Previous BOLD MRI studies have evaluated oxygenation of prostate cancer using carbogen [50, 55], which is not very well tolerated by patients. I report the first known study evaluating the changes in oxygenation of human prostate cancer in patients by oxygen breathing challenge using BOLD MRI.

In this study, 10 patients with biopsy confirmed prostate cancer and mean age of 59 years underwent BOLD MRI as part of their preoperative workup. The mean prostate-specific antigen (PSA) level was 6.9 ng/mL and Gleason score ranged from 6 to 9. Following IRB approval, patients underwent preoperative

scanning using a 3T MR scanner. Images were acquired using a 6-element SENSE body transmit coil and endorectal coil, which helps to improve the signal-to-noise ratio in the area of the prostate and hence the image quality compared to the whole-body coil alone. Dynamic T_2^* maps were acquired using a multi echo sequence, while subjects breathed air for 2 minutes followed by oxygen (15 l/min). Within 3 weeks following MRI, patients underwent robotic assisted laparoscopic prostatectomy.

All patients tolerated BOLD MRI with oxygen challenge. T_2^* values ranged from 14.7 ms to 44.5 ms. Bold MRI revealed vastly different T_2^* values between patients' prostates. The T_2^* values of tumors were remarkably similar to the values of the surrounding normal prostate stroma. By contrast surrounding muscle T_2^* values were very similar for all patients, indicating that heterogeneous values were specific to each patient's prostate. Figure 5.5 shows a representative study of changes in T_2^* measurement from a patient with a Gleason score of 9.

5.1.4 Conclusion

These studies indicate that each disease site presents different challenges, but by adopting appropriate pulse sequences, oxygen sensitive MRI is feasible in human patients.

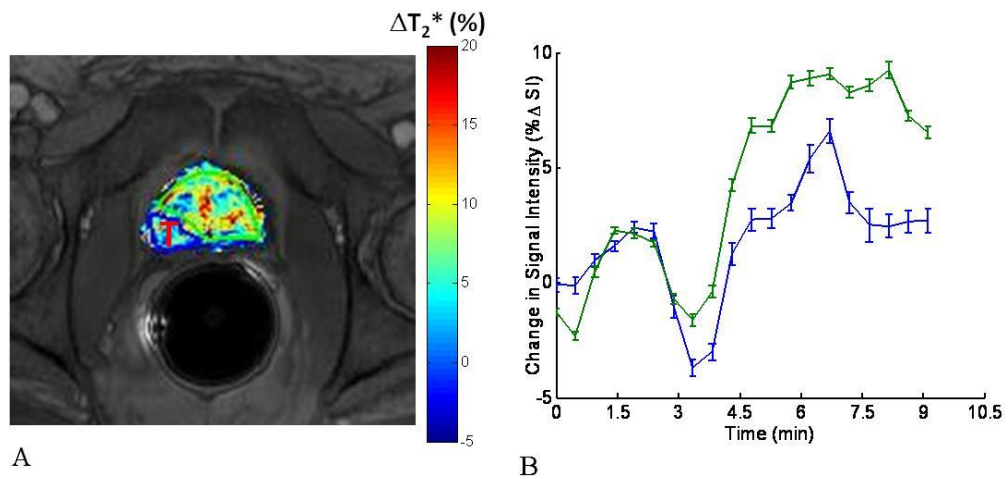


Figure 5-5 Quantitative BOLD in human prostate cancer with a Gleason score 9. A) ΔT_2^* maps of the tumor and normal prostate stroma overlaid on the T_2^*W image indicated the heterogeneous response to oxygen breathing. B) $\% \Delta T_2^*$ in T_2^* values for prostate tumor (blue) and prostate stroma (green) with respect to oxygen breathing challenge.

CHAPTER SIX

Conclusions and Recommendations

The paradox of hypoxia and radiation is that one would expect that more oxygen would result in better outcomes because radiation injury depends on free radical production requiring oxygen. However, countless attempts to clinically improve outcomes with oxygen breathing, carbogen breathing and even briefly hyperbaric oxygen chambers have been fruitless. The reasons are complex but have to do with the presence or absence of radical scavengers, heterogeneity and hypoxia cycling. Therefore, there is a need for noninvasive clinical assessment of tumor hypoxia prior to radiation therapy that aids in prognosis. The purpose of this study was to evaluate and validate the feasibility of measurements of interleaved T_2^* - and T_1 -weighted oxygen sensitive MRI, as well as R_2^* and R_1 maps of rat tumors and assess the relative sensitivity to changes in oxygenation. In addition, a feasibility study of BOLD MRI was performed on patients with cervical cancer.

A total of 34 rats were successfully imaged using ^1H and/or ^{19}F MRI. In the first part of my studies, I showed that there is a significant linear correlation between BOLD MRI and quantitative $p\text{O}_2$ measurements using FREDOM. A weaker, yet significant, correlation was observed between TOLD and $p\text{O}_2$. In comparing oxygen and carbogen as modulators of tumor hypoxia, I noticed that both gases elicited similar response in all techniques BOLD, TOLD and

FREDOM. In addition, hypoxic tumors showed significantly smaller and more sluggish response to hyperoxic gas breathing challenge in terms of pO_2 , T_2^* , BOLD and TOLD responses.

These results prompted me to investigate whether the noninvasive 1H MR measurements would predict the tumor response to therapy. In Chapter 3, I conducted the same 1H measurements as in Chapter 2 and added quantitative T_1 measurements before and after intervention. Based on the results from Chapter 2, only oxygen was used to modulate tumor hypoxia since it can be less stressful for patients than carbogen. DCE MRI was added after the BOLD and TOLD measurements by introducing 0.1mM/kg Gd-DTPA intravenously. Quantitative k^{trans} and v_e measurements were obtained based on Yankeelov modified model. The day after the MR data acquisition, the tumors received one of the following: sham radiation, 30 Gy during air breathing, or 30 Gy during oxygen breathing. Irradiation caused a significant tumor growth delay. No obvious correlation was observed between tumor growth delay and BOLD response, but those tumors with larger changes in both TOLD and T_1 values upon oxygen breathing exhibited significantly increased tumor growth delay. In addition, tumors with large v_e fraction had significantly slower growth rates regardless of the gas breathed during radiation. Notably, tumor growth delay was about double.

Since the ultimate goal of my study is to benefit patients undergoing therapy, I conducted BOLD MRI studies on 10 women with cervical cancer. In

this study, Chapter 4, successful results were achieved in nine patients with locally advanced cervical cancer (FIGO stage IIA to IVA) and three normal volunteers. Two sequences were tested in this study: a multi-shot EPI sequence and a multi-echo gradient echo while patients breathed room air followed by oxygen (15 dm³/min). Baseline T₂*-weighted signal intensity was quite stable, but increased to various extents in tumors upon initiation of oxygen breathing. These changes were compared with normal tissue including normal uterus and iliacus muscle. The highly vascularized uterus showed large increase in T₂*W SI and R₂* rates. To the contrary, iliacus muscle had minimal change. This preliminary study demonstrates that BOLD MRI of cervical cancer at 3T is feasible. Although no correlation was observed between BOLD MRI and treatment outcome, more patients must be evaluated and followed clinically before any prognostic value can be determined.

It is well known that the tumor microenvironment plays a role in tumor progression. Future preclinical studies should focus on evaluating BOLD, TOLD and DCE on orthotopic tumors. These tumor models will better mimic a clinical scenario and can provide a side to side comparison of the tumor response to intervention with its contralateral normal part. It is also crucial to conduct ¹H MRI experiments before and during tumor growth. This can provide important information on the effect of microenvironment on tumor growth, and allow tumor oxygenation assessment during angiogenesis. Since FREDOM cannot be used in

this process, a future one to one comparison study using ^{18}F -MISO-PET could enhance the MR clinical translatability.

In my studies, I showed that TOLD MRI may provide a clinically relevant tool for predicting tumor response to radiation therapy. However, several other treatments are often used in the clinic, such as chemotherapy or combined therapies. Since chemotherapeutic drugs require well perfused tumor vasculature to allow drug delivery, it is important to evaluate whether DCE or BOLD MRI have important prognostic values on such therapy. Also, it is recommended to add R_1 or TOLD measurements to future clinical studies.

BIBLIOGRAPHY

1. Hanahan, D. and R.A. Weinberg, *The Hallmarks of Cancer*. Cell, 2000. **100**(1): p. 57-70.
2. Weinberg, R.A., *The biology of cancer*. 2007: Garland Science.
3. Hanahan, D. and Robert A. Weinberg, *Hallmarks of Cancer: The Next Generation*. Cell, 2011. **144**(5): p. 646-674.
4. Avni, R., B. Cohen, and M. Neeman, *Hypoxic stress and cancer: imaging the axis of evil in tumor metastasis*. NMR in Biomedicine, 2011. **24**(6): p. 569-581.
5. Folkman, J., *Tumor Angiogenesis: Therapeutic Implications*. New England Journal of Medicine, 1971. **285**(21): p. 1182-1186.
6. O'Connor, J.P.B., A. Jackson, G.J.M. Parker, and G.C. Jayson, *DCE-MRI biomarkers in the clinical evaluation of antiangiogenic and vascular disrupting agents*. Br J Cancer, 2007. **96**(2): p. 189-195.
7. Vaupel, P., F. Kallinowski, and P. Okunieff, *Blood Flow, Oxygen and Nutrient Supply, and Metabolic Microenvironment of Human Tumors: A Review*. Cancer Research, 1989. **49**(23): p. 6449-6465.
8. Höckel, M. and P. Vaupel, *Tumor Hypoxia: Definitions and Current Clinical, Biologic, and Molecular Aspects*. Journal of the National Cancer Institute, 2001. **93**(4): p. 266-276.
9. Vaupel, P., D.K. Kelleher, and M. Höckel, *Oxygenation status of malignant tumors: Pathogenesis of hypoxia and significance for tumor therapy*. Seminars in Oncology, 2001. **28**, **Supplement 8**(0): p. 29-35.
10. Konerding, M.A., C. Ackern, E. Fait, F. Steinberg, and C. Streffer, *Morphological Aspects of Tumor Angiogenesis and Microcirculation*. Blood Perfusion and Microenvironment of Human Tumors, ed. M. Molls and P. Vaupel. 2002, New York: Springer.
11. Hall, E. and A.J. Giaccia, *Radiobiology for the radiologist*. 6th ed. 2006, Philadelphia, PA: Lippincott, Williams and Wilkins,.

12. Hellwig-Burgel, T., *Review : hypoxia-inducible factor-1 (HIF-1) : a novel transcription factor in immune reactions*. J Interferon Cytokine Res, 2005. **25**: p. 297-310.
13. Fyles, A., M. Milosevic, D. Hedley, M. Pintilie, W. Levin, L. Manchul, and R.P. Hill, *Tumor Hypoxia Has Independent Predictor Impact Only in Patients With Node-Negative Cervix Cancer*. J Clin Oncol, 2002. **20**(3): p. 680-687.
14. Hockel, M., K. Schlenger, B. Aral, M. Mitze, U. Schaffer, and P. Vaupel, *Association between Tumor Hypoxia and Malignant Progression in Advanced Cancer of the Uterine Cervix*. Cancer Res, 1996. **56**(19): p. 4509-4515.
15. Morgan, W.F. and M.B. Sowa, *Effects of ionizing radiation in nonirradiated cells*. Proceedings of the National Academy of Sciences of the United States of America, 2005. **102**(40): p. 14127-14128.
16. Mettler, F.A., D. Brenner, C.N. Coleman, J.M. Kaminski, A.R. Kennedy, and L.K. Wagner, *Can Radiation Risks to Patients Be Reduced Without Reducing Radiation Exposure? The Status of Chemical Radioprotectants*. American Journal of Roentgenology, 2011. **196**(3): p. 616-618.
17. Fyles, A.W., M. Milosevic, R. Wong, M.-C. Kavanagh, M. Pintilie, A. Sun, W. Chapman, W. Levin, L. Manchul, T.J. Keane, and R.P. Hill, *Oxygenation predicts radiation response and survival in patients with cervix cancer*. Radiotherapy and Oncology, 1998. **48**(2): p. 149-156.
18. Gray, L.H., A.D. Conger, M. Ebert, S. Hornsey, and O.C.A. Scott, *The Concentration of Oxygen Dissolved in Tissues at the Time of Irradiation as a Factor in Radiotherapy*. Br J Radiol, 1953. **26**(312): p. 638-648.
19. Tatum, J.L., *Hypoxia: Importance in tumor biology, noninvasive measurement by imaging, and value of its measurement in the management of cancer therapy*. International Journal of Radiation Biology, 2006. **82**(10): p. 699-757.
20. William A, D., *The role of hypoxia-activated prodrugs in cancer therapy*. The Lancet Oncology, 2000. **1**(1): p. 25-29.
21. Payen, E., M. Bettan, A. Henri, E. Tomkiewitcz, A. Houque, I. Kuzniak, J. Zuber, D. Scherman, and Y. Beuzard, *Oxygen tension and a*

- pharmacological switch in the regulation of transgene expression for gene therapy.* The Journal of Gene Medicine, 2001. **3**(5): p. 498-504.
22. Brizel, D.M., S.P. Scully, J.M. Harrelson, L.J. Layfield, J.M. Bean, L.R. Prosnitz, and M.W. Dewhirst, *Tumor Oxygenation Predicts for the Likelihood of Distant Metastases in Human Soft Tissue Sarcoma.* Cancer Res, 1996. **56**(5): p. 941-943.
 23. Le, Q.-T., E. Chen, A. Salim, H. Cao, C.S. Kong, R. Whyte, J. Donington, W. Cannon, H. Wakelee, R. Tibshirani, J.D. Mitchell, D. Richardson, K.J. O'Byrne, A.C. Koong, and A.J. Giaccia, *An Evaluation of Tumor Oxygenation and Gene Expression in Patients with Early Stage Non-Small Cell Lung Cancers.* Clinical Cancer Research, 2006. **12**(5): p. 1507-1514.
 24. Movsas, B., J.D. Chapman, A.L. Hanlon, E.M. Horwitz, R.E. Greenberg, C. Stobbe, G.E. Hanks, and A. Pollack, *Hypoxic prostate/muscle po2 ratio predicts for biochemical failure in patients with prostate cancer: preliminary findings.* Urology, 2002. **60**(4): p. 634-639.
 25. Krohn, K.A., J.M. Link, and R.P. Mason, *Molecular Imaging of Hypoxia.* Journal of Nuclear Medicine, 2008. **49**(Suppl 2): p. 129S-148S.
 26. Rasey, J.S., Z. Grunbaum, S. Magee, N.J. Nelson, P.L. Olive, R.E. Durand, and K.A. Krohn, *Characterization of Radiolabeled Fluoromisonidazole as a Probe for Hypoxic Cells.* Radiation research, 1987. **111**(2): p. 292-304.
 27. O'Donoghue, J.A., P. Zanzonico, A. Pugachev, B. Wen, P. Smith-Jones, S. Cai, E. Burnazi, R.D. Finn, P. Burgman, S. Ruan, J.S. Lewis, M.J. Welch, C.C. Ling, and J.L. Humm, *Assessment of regional tumor hypoxia using 18F-fluoromisonidazole and 64Cu(II)-diacetyl-bis(N4-methylthiosemicarbazone) positron emission tomography: Comparative study featuring microPET imaging, Po2 probe measurement, autoradiography, and fluorescent microscopy in the R3327-AT and FaDu rat tumor models.* International Journal of Radiation Oncology*Biophysics, 2005. **61**(5): p. 1493-1502.
 28. Mason, R.P., D. Zhao, J. Pacheco-Torres, W. Cui, V.D. Kodibagkar, P.K. Gulaka, G. Hao, P. Thorpe, E.W. Hahn, and P. Peschke, *Multimodality imaging of hypoxia in preclinical settings.* Journal of Nuclear Medicine Molecular Imaging, 2011. **25**(3): p. 259-280.

29. Krishna, M.C., S. English, K. Yamada, J. Yoo, R. Murugesan, N. Devasahayam, J.A. Cook, K. Golman, J.H. Ardenkjaer-Larsen, S. Subramanian, and J.B. Mitchell, *Overhauser enhanced magnetic resonance imaging for tumor oximetry: Coregistration of tumor anatomy and tissue oxygen concentration*. Proceedings of the National Academy of Sciences, 2002. **99**(4): p. 2216-2221.
30. Mason, R.P., P.P. Antich, E.E. Babcock, J.L. Gerberich, and R.L. Nunnally, *Perfluorocarbon imaging in vivo: A ¹⁹F MRI study in tumor-bearing mice*. Magnetic Resonance Imaging, 1989. **7**(5): p. 475-485.
31. Kodibagkar, V., X. Wang, and R. Mason, *Physical principles of quantitative nuclear magnetic resonance oximetry*. Front Biosci, 2008. **13**: p. 1371-1384.
32. Blackstock, A.W., H. Lightfoot, L.D. Case, J.E. Tepper, S.K. Mukherji, B.S. Mitchell, S.G. Swarts, and S.M. Hess, *Tumor Uptake and Elimination of 2',2'-Difluoro-2'-deoxycytidine (Gemcitabine) after Deoxycytidine Kinase Gene Transfer*. Clinical Cancer Research, 2001. **7**(10): p. 3263-3268.
33. Zhao, D., L. Jiang, and R. P. Mason, *Measuring Changes in Tumor Oxygenation*. Methods in Enzymology, 2004. **386**: p. 378-418.
34. Procissi, D., F. Claus, P. Burgman, J. Koziorowski, J.D. Chapman, S.B. Thakur, C. Matei, C.C. Ling, and J.A. Koutcher, *In vivo ¹⁹F Magnetic Resonance Spectroscopy and Chemical Shift Imaging of Tri-Fluoro-Nitroimidazole as a Potential Hypoxia Reporter in Solid Tumors*. Clinical Cancer Research, 2007. **13**(12): p. 3738-3747.
35. Robinson, S.P. and J.R. Griffiths, *Current issues in the utility of ¹⁹F nuclear magnetic resonance methodologies for the assessment of tumour hypoxia*. Philosophical Transactions of the Royal Society of London. Series B: Biological Sciences, 2004. **359**(1446): p. 987-996.
36. Seddon, B.M., G.S. Payne, L. Simmons, R. Ruddle, R. Grimshaw, S. Tan, A. Turner, F. Raynaud, G. Halbert, M.O. Leach, I. Judson, and P. Workman, *A Phase I Study of SR-4554 via Intravenous Administration for Noninvasive Investigation of Tumor Hypoxia by Magnetic Resonance Spectroscopy in Patients with Malignancy*. Clinical Cancer Research, 2003. **9**(14): p. 5101-5112.

37. Taylor, N.J., H. Baddeley, K.A. Goodchild, M.E.B. Powell, M. Thoumine, L.A. Culver, J.J. Stirling, M.I. Saunders, P.J. Hoskin, H. Phillips, A.R. Padhani, and J.R. Griffiths, *BOLD MRI of human tumor oxygenation during carbogen breathing*. Journal of Magnetic Resonance Imaging, 2001. **14**(2): p. 156-163.
38. Ogawa, S., T.M. Lee, A.R. Kay, and D.W. Tank, *Brain magnetic resonance imaging with contrast dependent on blood oxygenation*. Proceedings of the National Academy of Sciences, 1990. **87**(24): p. 9868-9872.
39. Thulborn, K.R., J.C. Waterton, P.M. Matthews, and G.K. Radda, *Oxygenation dependence of the transverse relaxation time of water protons in whole blood at high field*. Biochimica et Biophysica Acta (BBA) - General Subjects, 1982. **714**(2): p. 265-270.
40. Padhani, A., K. Krohn, J. Lewis, and M. Alber, *Imaging oxygenation of human tumours*. European Radiology, 2007. **17**(4): p. 861-872.
41. Huettle, S., A. Song, and G. McCarthy, *Functional Magnetic Resonance Imaging 2003*, Sunderland, MA: Sinauer.
42. Weishaupt, D., V. Kochli, and B. Marincek, *How Does Mri Work?: An Introduction to the Physics And Function of Magnetic Resonance Imaging*. 2006: Springer.
43. Stanisz, G.J., E.E. Odrobina, J. Pun, M. Escaravage, S.J. Graham, M.J. Bronskill, and R.M. Henkelman, *T1, T2 relaxation and magnetization transfer in tissue at 3T*. Magnetic Resonance in Medicine, 2005. **54**(3): p. 507-512.
44. Kuperman, V.Y.U., J.N. River, M.Z. Lewis, L.M. Lubich, and G.S. Karczmar, *Changes in T2*-Weighted Images During Hyperoxia Differentiate Tumors from Normal Tissue*. Magnetic Resonance in Medicine, 1995. **33**(3): p. 318-325.
45. Robinson, S.P., F.A. Howe, and J.R. Griffiths, *Noninvasive monitoring of carbogen-induced changes in tumor blood flow and oxygenation by functional magnetic resonance imaging*. International Journal of Radiation Oncology*Biophysics, 1995. **33**(4): p. 855-859.

46. Howe, F.A., S.P. Robinson, D.J.O. McIntyre, M. Stubbs, and J.R. Griffiths, *Issues in flow and oxygenation dependent contrast (FLOOD) imaging of tumours*. NMR in Biomedicine, 2001. **14**(7-8): p. 497-506.
47. Robinson, S.P., P.F.J.W. Rijken, F.A. Howe, P.M.J. McSheehy, B.P.J. van der Sanden, A. Heerschap, M. Stubbs, A.J. van der Kogel, and J.R. Griffiths, *Tumor vascular architecture and function evaluated by non-invasive susceptibility MRI methods and immunohistochemistry*. Journal of Magnetic Resonance Imaging, 2003. **17**(4): p. 445-454.
48. Chavhan, G.B., P.S. Babyn, B. Thomas, M.M. Shroff, and E.M. Haacke, *Principles, Techniques, and Applications of T2*-based MR Imaging and Its Special Applications*. Radiographics, 2009. **29**(5): p. 1433-1449.
49. Fernández-Seara, M.A. and F.W. Wehrli, *Postprocessing technique to correct for background gradients in image-based R*2 measurements*. Magnetic Resonance in Medicine, 2000. **44**(3): p. 358-366.
50. Padhani, A., *Science to Practice: What Does MR Oxygenation Imaging Tell Us about Human Breast Cancer Hypoxia?* Radiology, 2010. **254**(1): p. 1-3.
51. Baudelet, C. and B. Gallez, *Current Issues in the Utility of Blood Oxygen Level Dependent MRI for the Assessment of Modulations in Tumor Oxygenation*. Current Medical Imaging Reviews, 2005. **1**(3): p. 229-243.
52. Neeman, M., H. Dafni, O. Bukhari, R.D. Braun, and M.W. Dewhirst, *In vivo BOLD contrast MRI mapping of subcutaneous vascular function and maturation: Validation by intravital microscopy*. Magnetic Resonance in Medicine, 2001. **45**(5): p. 887-898.
53. Zhao, D., L. Jiang, E.W. Hahn, and R.P. Mason, *Comparison of ¹H blood oxygen level-dependent (BOLD) and ¹⁹F MRI to investigate tumor oxygenation*. Magnetic Resonance in Medicine, 2009. **62**(2): p. 357-364.
54. Al-Hallaq, H.A., X. Fan, M. Zamora, J.N. River, J.E. Moulder, and G.S. Karczmar, *Spectrally inhomogeneous BOLD contrast changes detected in rodent tumors with high spectral and spatial resolution MRI*. NMR in Biomedicine, 2002. **15**(1): p. 28-36.
55. Alonzi, R., A.R. Padhani, R.J. Maxwell, N.J. Taylor, J.J. Stirling, J.I. Wilson, J.A. d'Arcy, D.J. Collins, M.I. Saunders, and P.J. Hoskin,

- Carbogen breathing increases prostate cancer oxygenation: a translational MRI study in murine xenografts and humans.* Br J Cancer, 2009. **100**(4): p. 644-648.
56. Chopra, S., W.D. Foltz, M.F. Milosevic, A. Toi, R.G. Bristow, C. Ménard, and M. A. Haider, *Comparing oxygen-sensitive MRI (BOLD R2*) with oxygen electrode measurements: A pilot study in men with prostate cancer.* International Journal of Radiation Biology, 2009. **85**(9): p. 805 - 813.
 57. Diergarten, T., P. Martirosian, R. Kottke, U. Vogel, A. Stenzl, C.D. Claussen, and H.-P. Schlemmer, *Functional Characterization of Prostate Cancer by Integrated Magnetic Resonance Imaging and Oxygenation Changes During Carbogen Breathing.* Investigative Radiology, 2005. **40**(2): p. 102-109.
 58. Rijpkema, M., J.H.A.M. Kaanders, F.B.M. Joosten, A.J. van der Kogel, and A. Heerschap, *Effects of breathing a hyperoxic hypercapnic gas mixture on blood oxygenation and vascularity of head-and-neck tumors as measured by magnetic resonance imaging.* International Journal of Radiation Oncology*Biophysics, 2002. **53**(5): p. 1185-1191.
 59. Müller, A., S. Remmele, I. Wenningmann, H. Clusmann, F. Träber, S. Flacke, R. König, J. Gieseke, W. Willinek, H. Schild, and P. Mürtz, *Analysing the response in R2* relaxation rate of intracranial tumours to hyperoxic and hypercapnic respiratory challenges: initial results.* European Radiology, 2011. **21**(4): p. 786-798.
 60. Müller, A., S. Remmele, I. Wenningmann, H. Clusmann, F. Träber, S. Flacke, R. König, J. Gieseke, W.A. Willinek, H.H. Schild, and P. Mürtz, *Intracranial tumor response to respiratory challenges at 3.0 T: Impact of different methods to quantify changes in the MR relaxation rate R2*.* Journal of Magnetic Resonance Imaging, 2010. **32**(1): p. 17-23.
 61. Rakow-Penner, R., B. Daniel, and G.H. Glover, *Detecting blood oxygen level-dependent (BOLD) contrast in the breast.* Journal of Magnetic Resonance Imaging, 2010. **32**(1): p. 120-129.
 62. Jiang, L., D. Zhao, A. Constantinescu, and R.P. Mason, *Comparison of BOLD contrast and Gd-DTPA dynamic contrast-enhanced imaging in rat prostate tumor.* Magnetic Resonance in Medicine, 2004. **51**(5): p. 953-960.

63. Baudelet, C. and B. Gallez, *How does blood oxygen level-dependent (BOLD) contrast correlate with oxygen partial pressure (pO₂) inside tumors?* Magnetic Resonance in Medicine, 2002. **48**(6): p. 980-986.
64. Dunn, J.F., J.A. O'Hara, Y. Zaim-Wadghiri, H. Lei, M.E. Meyerand, O.Y. Grinberg, H. Hou, P.J. Hoopes, E. Demidenko, and H.M. Swartz, *Changes in oxygenation of intracranial tumors with carbogen: A BOLD MRI and EPR oximetry study.* Journal of Magnetic Resonance Imaging, 2002. **16**(5): p. 511-521.
65. Elas, M., B.B. Williams, A. Parasca, C. Mailer, C.A. Pelizzari, M.A. Lewis, J.N. River, G.S. Karczmar, E.D. Barth, and H.J. Halpern, *Quantitative tumor oxymetric images from 4D electron paramagnetic resonance imaging (EPRI): Methodology and comparison with blood oxygen level-dependent (BOLD) MRI.* Magnetic Resonance in Medicine, 2003. **49**(4): p. 682-691.
66. Fan, X., J.N. River, M. Zamora, H.A. Al-Hallaq, and G.S. Karczmar, *Effect of carbogen on tumor oxygenation: combined fluorine-19 and proton MRI measurements.* International Journal of Radiation Oncology*Biophysics, 2002. **54**(4): p. 1202-1209.
67. McPhail, L.D. and S.P. Robinson, *Intrinsic Susceptibility MR Imaging of Chemically Induced Rat Mammary Tumors: Relationship to Histologic Assessment of Hypoxia and Fibrosis1.* Radiology, 2010. **254**(1): p. 110-118.
68. Rodrigues, L., F. Howe, J. Griffiths, and S. Robinson, *Tumor R₂* is a prognostic indicator of acute radiotherapeutic response in rodent tumors.* Journal of Magnetic Resonance Imaging, 2004. **19**(4): p. 482-488.
69. Jordan, B.F., N. Crockart, C. Baudelet, G.O. Cron, R. Ansiaux, and B. Gallez, *Complex relationship between changes in oxygenation status and changes in R₂*: The case of insulin and NS-398, two inhibitors of oxygen consumption.* Magnetic Resonance in Medicine, 2006. **56**(3): p. 637-643.
70. Thomas, C.D., E. Chenu, C. Walczak, M.-J. Plessis, F. Perin, and A. Volk, *Morphological and carbogen-based functional MRI of a chemically induced liver tumor model in mice.* Magnetic Resonance in Medicine, 2003. **50**(3): p. 522-530.

71. Barth, M. and B.A. Poser, *Advances in High-Field BOLD fMRI*. Materials, 2011. **4**(11): p. 1941-1955.
72. Gizewski, E.R., A. de Greiff, S. Maderwald, D. Timmann, M. Forsting, and M.E. Ladd, *fMRI at 7 T: Whole-brain coverage and signal advantages even infratentorially?* NeuroImage, 2007. **37**(3): p. 761-768.
73. Gruetter, R., *Automatic, localized in Vivo adjustment of all first-and second-order shim coils*. Magnetic Resonance in Medicine, 1993. **29**(6): p. 804-811.
74. Matsumoto, K.-i., M. Bernardo, S. Subramanian, P. Choyke, J.B. Mitchell, M.C. Krishna, and M.J. Lizak, *MR assessment of changes of tumor in response to hyperbaric oxygen treatment*. Magnetic Resonance in Medicine, 2006. **56**(2): p. 240-246.
75. Howe, F.A., S.P. Robinson, L.M. Rodrigues, and J.R. Griffiths, *Flow and oxygenation dependent (FLOOD) contrast MR imaging to monitor the response of rat tumors to carbogen breathing*. Magnetic Resonance Imaging, 1999. **17**(9): p. 1307-1318.
76. Foxley, S., X. Fan, D. Mustafi, C. Haney, M. Zamora, E. Markiewicz, M. Medved, A.M. Wood, and G.S. Karczmar, *Sensitivity to tumor microvasculature without contrast agents in high spectral and spatial resolution MR images*. Magnetic Resonance in Medicine, 2009. **61**(2): p. 291-298.
77. Alonzi, R., A.R. Padhani, and C. Allen, *Dynamic contrast enhanced MRI in prostate cancer*. European Journal of Radiology, 2007. **63**(3): p. 335-350.
78. Evelhoch, J.L., *Key factors in the acquisition of contrast kinetic data for oncology*. Journal of Magnetic Resonance Imaging, 1999. **10**(3): p. 254-259.
79. Tofts, P.S., G. Brix, D.L. Buckley, J.L. Evelhoch, E. Henderson, M.V. Knopp, H.B.W. Larsson, T.-Y. Lee, N.A. Mayr, G.J.M. Parker, R.E. Port, J. Taylor, and R.M. Weisskoff, *Estimating kinetic parameters from dynamic contrast-enhanced T1-weighted MRI of a diffusable tracer: Standardized quantities and symbols*. Journal of Magnetic Resonance Imaging, 1999. **10**(3): p. 223-232.

80. Eyal, E. and H. Degani, *Model-based and model-free parametric analysis of breast dynamic-contrast-enhanced MRI*. NMR in Biomedicine, 2009. **22**(1): p. 40-53.
81. Tofts, P.S., *Modeling tracer kinetics in dynamic Gd-DTPA MR imaging*. Journal of Magnetic Resonance Imaging, 1997. **7**(1): p. 91-101.
82. Yankeelov, T.E., J.J. Luci, M. Lepage, R. Li, L. Debusk, P.C. Lin, R.R. Price, and J.C. Gore, *Quantitative pharmacokinetic analysis of DCE-MRI data without an arterial input function: a reference region model*. Magnetic Resonance Imaging, 2005. **23**(4): p. 519-529.
83. Ceelen, W., P. Smeets, W. Backes, N. Van Damme, T. Boterberg, P. Demetter, I. Bouckennooghe, M. De Visschere, M. Peeters, and P. Pattyn, *Noninvasive monitoring of radiotherapy-induced microvascular changes using dynamic contrast enhanced magnetic resonance imaging (DCE-MRI) in a colorectal tumor model*. International Journal of Radiation Oncology*Biography*Physics, 2006. **64**(4): p. 1188-1196.
84. Lyng, H., A.O. Vorren, K. Sundfjør, I. Taksdal, H.H. Lien, O. Kaalhus, and E.K. Rofstad, *Assessment of tumor oxygenation in human cervical carcinoma by use of dynamic Gd-DTPA-enhanced MR imaging*. Journal of Magnetic Resonance Imaging, 2001. **14**(6): p. 750-756.
85. Wang, Z., M.Y. Su, and O. Nalcioglu, *Applications of dynamic contrast enhanced MRI in oncology: measurement of tumor oxygen tension*. Technology in cancer research & treatment, 2002. **1**(1): p. 29-38.
86. Benjaminsen, I.C., K.G. Brurberg, E.-B.M. Ruud, and E.K. Rofstad, *Assessment of extravascular extracellular space fraction in human melanoma xenografts by DCE-MRI and kinetic modeling*. Magnetic Resonance Imaging, 2008. **26**(2): p. 160-170.
87. Rijpkema, M., J. Schuurings, P.L. Bernsen, H.J. Bernsen, J.H.A.M. Kaanders, A.J. van der Kogel, and A. Heerschap, *BOLD MRI response to hypercapnic hyperoxia in patients with meningiomas: correlation with Gadolinium-DTPA uptake rate*. Magnetic Resonance Imaging, 2004. **22**(6): p. 761-767.
88. Franiel, T., L. Lüdemann, B. Rudolph, H. Rehbein, C. Stephan, M. Taupitz, and D. Beyersdorff, *Prostate MR Imaging: Tissue Characterization with Pharmacokinetic Volume and Blood Flow*

- Parameters and Correlation with Histologic Parameters I.* Radiology, 2009. **252**(1): p. 101-108.
89. Faithfull, N.S., *Mechanisms and Efficacy of Fluorochemical Oxygen Transport and Delivery.* Artificial Cells, Blood Substitutes and Biotechnology, 1994. **22**(2): p. 181-197.
90. Riess, J.G., *Fluorocarbon-Based in vivo Oxygen Transport and Delivery Systems.* Vox Sanguinis, 1991. **61**(4): p. 225-239.
91. Zuck, T.F., J.G. Riess, and G.P. Biro, *Current Status of Injectable Oxygen Carriers.* Critical Reviews in Clinical Laboratory Sciences, 1994. **31**(4): p. 295-324.
92. Kucejova, B., N.E. Sunny, A.D. Nguyen, R. Hallac, X. Fu, S. Pena-Llopis, R.P. Mason, R.J. DeBerardinis, X.J. Xie, R. DeBose-Boyd, V.D. Kodibagkar, S.C. Burgess, and J. Brugarolas, *Uncoupling hypoxia signaling from oxygen sensing in the liver results in hypoketotic hypoglycemic death.* Oncogene, 2011. **30**(18): p. 2147-2160.
93. Spence, R.K., *Perfluorocarbons in the Twenty-First Century: Clinical Applications as Transfusion Alternatives.* Artificial Cells, Blood Substitutes and Biotechnology, 1995. **23**(3): p. 367-380.
94. Kodibagkar, V., R.R. Hallac, D. Zhao, J.-X. Yu, and R.P. Mason, *¹⁹F NMR: Clinical and Molecular Imaging Applications Fluorine in Pharmaceutical and Medicinal Chemistry From Biophysical Aspects to Clinical Applications* ed. V. Gouverneur and K. Müller. Vol. 6. 2012: World Scientific.
95. Marwick, C., *MOre than a trickle of interest in blood substitutes.* JAMA: The Journal of the American Medical Association, 1994. **271**(12): p. 895-895.
96. Smith, D.J. and T.A. Lane, *Effect of a High Concentration PERFLUOCARBON Emulsion on Platelet Function.* Artificial Cells, Blood Substitutes and Biotechnology, 1992. **20**(2-4): p. 1045-1049.
97. Zhao, D., S. Ran, A. Constantinescu, E.W. Hahn, and R.P. Mason, *Tumor oxygen dynamics: correlation of in vivo MRI with histological findings.* Neoplasia (New York, N.Y.), 2003. **5**(4): p. 308-318.

98. Eidelberg, D., G. Johnson, D. Barnes, P.S. Tofts, D. Delpy, D. Plummer, and W.I. McDonald, *19F NMR imaging of blood oxygenation in the brain*. Magnetic Resonance in Medicine, 1988. **6**(3): p. 344-352.
99. Lai, C.-S., S.J. Stair, H. Mizioroko, and J.S. Hyde, *Effect of oxygen and the lipid spin label TEMPO-laurate on fluorine-19 and proton relaxation rates of the perfluorochemical blood substitute, FC-43 emulsion*. Journal of Magnetic Resonance (1969), 1984. **57**(3): p. 447-452.
100. Mason, R.P., H. Shukla, and P.P. Antich, *In vivo oxygen tension and temperature: Simultaneous determination using 19F NMR spectroscopy of perfluorocarbon*. Magnetic Resonance in Medicine, 1993. **29**(3): p. 296-302.
101. Mason, R.P., W. Rodbumrung, and P.P. Antich, *Hexafluorobenzene: a Sensitive 19F NMR Indicator of Tumor Oxygenation*. NMR in Biomedicine, 1996. **9**(3): p. 125-134.
102. Shukla, H.P., R.P. Mason, D.E. Woessner, and P.P. Antich, *A Comparison of Three Commercial Perfluorocarbon Emulsions as High-Field 19F NMR Probes of Oxygen Tension and Temperature*. Journal of Magnetic Resonance, Series B, 1995. **106**(2): p. 131-141.
103. Mason, R.P., H. Shukla, and P.P. Antich, *Oxygent™: A Novel Probe of Tissue Oxygen Tension*. Artificial Cells, Blood Substitutes and Biotechnology, 1992. **20**(2-4): p. 929-932.
104. Dardzinski, B.J. and C.H. Sotak, *Rapid tissue oxygen tension mapping using 19F inversion-recovery echo-planar imaging of P erfluoro-15 - crown-5-ether*. Magnetic Resonance in Medicine, 1994. **32**(1): p. 88-97.
105. Berkowitz, B.A., C.A. Wilson, and D.L. Hatchell, *Oxygen kinetics in the vitreous substitute perfluorotributylamine: a 19F NMR study in vivo*. Investigative Ophthalmology & Visual Science, 1991. **32**(8): p. 2382-7.
106. Wilson, C.A., B.A. Berkowitz, and D.L. Hatchell, *Oxygen kinetics in preretinal perfluorotributylamine*. Experimental Eye Research, 1992. **55**(1): p. 119-126.
107. Zhang, W., Y. Ito, E. Berlin, R. Roberts, and B.A. Berkowitz, *Role of Hypoxia during Normal Retinal Vessel Development and in Experimental*

- Retinopathy of Prematurity*. Investigative Ophthalmology & Visual Science, 2003. **44**(7): p. 3119-3123.
108. Duong, T.Q., C. Iadecola, and S.-G. Kim, *Effect of hyperoxia, hypercapnia, and hypoxia on cerebral interstitial oxygen tension and cerebral blood flow*. Magnetic Resonance in Medicine, 2001. **45**(1): p. 61-70.
 109. Kodibagkar, V.D., X. Wang, J. Pacheco-Torres, P. Gulaka, and R.P. Mason, *Proton imaging of siloxanes to map tissue oxygenation levels (PISTOL): a tool for quantitative tissue oximetry*. NMR in Biomedicine, 2008. **21**(8): p. 899-907.
 110. Liu, S., S.J. Shah, L.J. Wilmes, J. Feiner, V.D. Kodibagkar, M.F. Wendland, R.P. Mason, N. Hylton, H.W. Hopf, and M.D. Rollins, *Quantitative tissue oxygen measurement in multiple organs using ¹⁹F MRI in a rat model*. Magnetic Resonance in Medicine, 2011. **66**(6): p. 1722-1730.
 111. Bourke, V.A., D. Zhao, J. Gilio, C.-H. Chang, L. Jiang, E.W. Hahn, and R.P. Mason, *Correlation of radiation response with tumor oxygenation in the Dunning prostate R3327-AT1 tumor*. International Journal of Radiation Oncology*Biology*Physics, 2007. **67**(4): p. 1179-1186.
 112. Hunjan, S., D. Zhao, A. Constantinescu, E.W. Hahn, P.P. Antich, and R.P. Mason, *Tumor oximetry: demonstration of an enhanced dynamic mapping procedure using fluorine-19 echo planar magnetic resonance imaging in the Dunning prostate R3327-AT1 rat tumor*. International Journal of Radiation Oncology*Biology*Physics, 2001. **49**(4): p. 1097-1108.
 113. Zhao, D., A. Constantinescu, L. Jiang, E.W. Hahn, and R.P. Mason, *Prognostic Radiology: Quantitative Assessment of Tumor Oxygen Dynamics by MRI*. American Journal of Clinical Oncology, 2001. **24**(5): p. 462-466.
 114. O'Connor, J.P.B., J.H. Naish, G.J.M. Parker, J.C. Waterton, Y. Watson, G.C. Jayson, G.A. Buonaccorsi, S. Cheung, D.L. Buckley, D.M. McGrath, C.M.L. West, S.E. Davidson, C. Roberts, S.J. Mills, C.L. Mitchell, L. Hope, N.C. Ton, and A. Jackson, *Preliminary Study of Oxygen-Enhanced Longitudinal Relaxation in MRI: A Potential Novel Biomarker of Oxygenation Changes in Solid Tumors*. International Journal of Radiation Oncology*Biology*Physics, 2009. **75**(4): p. 1209-1215.

115. Hallac, R.R., Y. Ding, Q. Yuan, R.W. McColl, J. Lea, R.D. Sims, P.T. Weatherall, and R.P. Mason, *Oxygenation in cervical cancer and normal uterine cervix assessed using blood oxygenation level-dependent (BOLD) MRI at 3T*. NMR in Biomedicine, 2012.
116. McPhail, L.D. and S.P. Robinson, *Intrinsic Susceptibility MR Imaging of Chemically Induced Rat Mammary Tumors: Relationship to Histologic Assessment of Hypoxia and Fibrosis*. Radiology, 2010. **254**(1): p. 110-118.
117. Robinson, S.P., F.A. Howe, L.M. Rodrigues, M. Stubbs, and J.R. Griffiths, *Magnetic resonance imaging techniques for monitoring changes in tumor oxygenation and blood flow*. Seminars in Radiation Oncology, 1998. **8**(3): p. 197-207.
118. Young, I., G. Clarke, D. Bailes, J. Pennock, F. Doyle, and G. Bydder, *Enhancement of relaxation rate with paramagnetic contrast agents in NMR imaging*. The Journal of Computed Tomography, 1981. **5**(6): p. 543-547.
119. O'Connor, J.P.B., J.H. Naish, A. Jackson, J.C. Waterton, Y. Watson, S. Cheung, D.L. Buckley, D.M. McGrath, G.A. Buonaccorsi, S.J. Mills, C. Roberts, G.C. Jayson, and G.J.M. Parker, *Comparison of normal tissue R1 and R*2 modulation by oxygen and carbogen*. Magnetic Resonance in Medicine, 2009. **61**(1): p. 75-83.
120. Baete, S., J. Vandecasteele, L. Colman, W. De Neve, and Y. De Deene, *An oxygen-consuming phantom simulating perfused tissue to explore oxygen dynamics and ^{19}F MRI oximetry*. Magnetic Resonance Materials in Physics, Biology and Medicine, 2010. **23**(4): p. 217-226.
121. Magat, J., B. Jordan, G. Cron, and B. Gallez, *Noninvasive mapping of spontaneous fluctuations in tumor oxygenation using ^{19}F MRI*. Medical Physics, 2010. **37**(10): p. 5434-5441.
122. Peschke, P., E.W. Hahn, F. Wenz, F. Lohr, F. Braunschweig, G. Wolber, I. Zuna, and M. Wannemacher, *Differential Sensitivity of Three Sublines of the Rat Dunning Prostate Tumor System R3327 to Radiation and/or Local Tumor Hyperthermia*. Radiation research, 1998. **150**(4): p. 423-430.
123. Peschke, P., C.P. Karger, M. Scholz, J. Debus, and P.E. Huber, *Relative Biological Effectiveness of Carbon Ions for Local Tumor Control of a*

- Radioresistant Prostate Carcinoma in the Rat*. International Journal of Radiation Oncology*Biology*Physics, 2011. **79**(1): p. 239-246.
124. Mason, R.P., A. Constantinescu, S. Hunjan, D. Le, E.W. Hahn, P.P. Antich, C. Blum, and P. Peschke, *Regional tumor oxygenation and measurement of dynamic changes*. Radiation research, 1999. **152**(3): p. 239-249.
 125. Al-Hallaq, H.A., J.N. River, M. Zamora, H. Oikawa, and G.S. Karczmar, *Correlation of Magnetic Resonance and Oxygen Microelectrode Measurements of Carbogen-Induced Changes in Tumor Oxygenation*. International Journal of Radiation Oncology*Biology*Physics, 1998. **41**(1): p. 151-159.
 126. Christen, T., B. Lemasson, N. Pannetier, R. Farion, C. Remy, G. Zaharchuk, and E.L. Barbier, *Is T2* Enough to Assess Oxygenation? Quantitative Blood Oxygen Level-Dependent Analysis in Brain Tumor*. Radiology, 2012. **262**(2): p. 495-502.
 127. Pacheco-Torres, J., D. Zhao, A. Contero, P. Peschke, and R.P. Mason. *DOCENT-Dynamic Oxygen Challenge Evaluated by NMR T1 and T2* of Tumors*. in *16th ISMRM*. 2008. Toronto, Canad.
 128. Winter, J.D., M.K. Akens, and H.L. Cheng, *Quantitative MRI assessment of VX2 tumour oxygenation changes in response to hyperoxia and hypercapnia*. Physics in medicine and biology, 2011. **56**(5): p. 1225-1242.
 129. Ding, Y., R.P. Mason, Q. Yuan, R.R. Hallac, R. McColl, R. Sims, and P. Weatherall. *Interleaved T1- and T2*-weighted Imaging Can Evaluate Dynamic Oxygen Challenge: A Feasibility Study*. in *ISMRM 2010*. Stockholm, Sweden.
 130. Remmele, S., T. Voigt, J. Keupp, C. Stehning, and J. S negas. *Simultaneous $\Delta R1$ and $\Delta R2^*$ Quantification in 5s to Monitor Blood and Tissue Oxygenation with Dynamic (C)O2 Enhanced MRI*. in *ISMRM*. 2010. Stockholm, Sweden.
 131. Gulliksrud, K., K.M.  vreb , B. Mathiesen, and E.K. Rofstad, *Differentiation between hypoxic and non-hypoxic experimental tumors by dynamic contrast-enhanced magnetic resonance imaging*. Radiotherapy and Oncology, 2011. **98**(3): p. 360-364.

132. Knowles, H. and A. Harris, *Hypoxia and oxidative stress in breast cancer: Hypoxia and tumorigenesis*. Breast Cancer Res, 2001. **3**(5): p. 318 - 322.
133. Hockel, M. and P. Vaupel, *Tumor Hypoxia: Definitions and Current Clinical, Biologic, and Molecular Aspects*. Journal of the National Cancer Institute, 2001. **93**(4): p. 266-276.
134. Rofstad, E.K., K. Sundfor, H. Lyng, and C.G. Trope, *Hypoxia-induced treatment failure in advanced squamous cell carcinoma of the uterine cervix is primarily due to hypoxia-induced radiation resistance rather than hypoxia-induced metastasis*. British Journal of Cancer, 2000. **83**(3): p. 354-359.
135. Jaeger, K.D., M.C. Kavanagh, and R.P. Hill, *Relationship of hypoxia to metastatic ability in rodent tumours*, Nature Publishing Group.
136. Cairns, R.A., T. Kalliomaki, and R.P. Hill, *Acute (Cyclic) Hypoxia Enhances Spontaneous Metastasis of KHT Murine Tumors*. Cancer Research, 2001. **61**(24): p. 8903-8908.
137. Egeland, T.A.M., J.-V. Gaustad, I.K. Vestvik, I.C. Benjaminsen, B. Mathiesen, and E.K. Rofstad, *Assessment of fraction of radiobiologically hypoxic cells in human melanoma xenografts by dynamic contrast-enhanced MRI*. Magnetic Resonance in Medicine, 2006. **55**(4): p. 874-882.
138. Egeland, T.A.M., T.G. Simonsen, J.-V. Gaustad, K. Gulliksrud, C. Ellingsen, and E.K. Rofstad, *Dynamic Contrast-Enhanced Magnetic Resonance Imaging of Tumors: Preclinical Validation of Parametric Images*. Radiation research, 2009. **172**(3): p. 339-347.
139. Vestvik, I.K., T.A.M. Egeland, J.-V. Gaustad, B. Mathiesen, and E.K. Rofstad, *Assessment of microvascular density, extracellular volume fraction, and radiobiological hypoxia in human melanoma xenografts by dynamic contrast-enhanced MRI*. Journal of Magnetic Resonance Imaging, 2007. **26**(4): p. 1033-1042.
140. Ma, C., C. Coffey, L. DeWerd, C. Liu, R. Nath, S. Seltzer, and J. Seuntjens, *AAPM protocol for 40-300 kV x-ray beam dosimetry in radiotherapy and radiobiology*. Medical Physics, 2001. **28**: p. 868-893.

141. Faranesh, A.Z. and T.E. Yankeelov, *Incorporating a vascular term into a reference region model for the analysis of DCE-MRI data: a simulation study*. *Physics in medicine and biology*, 2008. **53**(10): p. 2617-2631.
142. Arias, N., J. Pacheco-Torres, and P. López-Larrubia. *Predicting response to hyperbaric oxygen radiotherapy treatment in high grade gliomas using Magnetic Resonance Imaging techniques*. in *ISMRM*. 2012. Melbourne, Australia.
143. Øvrebø, K.M., T. Hompland, B. Mathiesen, and E.K. Rofstad, *Assessment of hypoxia and radiation response in intramuscular experimental tumors by dynamic contrast-enhanced magnetic resonance imaging*. *Radiotherapy and Oncology*, 2012. **102**(3): p. 429-435.
144. Moulder, J.E. and S. Rockwell, *Hypoxic fractions of solid tumors: Experimental techniques, methods of analysis, and a survey of existing data*. *International Journal of Radiation Oncology*Biology*Physics*, 1984. **10**(5): p. 695-712.
145. Gullledge, C.J. and M.W. Dewhirst, *Tumor oxygenation: a matter of supply and demand*. *Anticancer research*, 1996. **16**(2): p. 741-749.
146. Zhao, D., A. Constantinescu, E.W. Hahn, and R.P. Mason, *Tumor Oxygen Dynamics with Respect to Growth and Respiratory Challenge: Investigation of the Dunning Prostate R3327-HI Tumor*. *Radiation research*, 2001. **156**(5): p. 510-520.
147. Timmerman R, P.R.G.J. and et al., *STereotactic body radiation therapy for inoperable early stage lung cancer*. *JAMA: The Journal of the American Medical Association*, 2010. **303**(11): p. 1070-1076.
148. Carlson, D.J., P.J. Keall, B.W. Loo Jr, Z.J. Chen, and J.M. Brown, *Hypofractionation Results in Reduced Tumor Cell Kill Compared to Conventional Fractionation for Tumors With Regions of Hypoxia*. *International Journal of Radiation Oncology*Biology*Physics*, 2011. **79**(4): p. 1188-1195.
149. Brown, J.M., M. Diehn, and B.W. Loo Jr, *Stereotactic Ablative Radiotherapy Should Be Combined With a Hypoxic Cell Radiosensitizer*. *International Journal of Radiation Oncology*Biology*Physics*, 2010. **78**(2): p. 323-327.

150. Mason, R.P., D. Zhao, J. Pacheco-Torres, W. Cui, V.D. Kodibagkar, P.K. Gulaka, G. Hao, P. Thorpe, E.W. Hahn, and P. Peschke, *Multimodality imaging of hypoxia in preclinical settings*. The quarterly journal of nuclear medicine and molecular imaging, 2010. **54**(3): p. 259-280.
151. Brizel, D.M., G.S. Sibley, L.R. Prosnitz, R.L. Scher, and M.W. Dewhirst, *Tumor hypoxia adversely affects the prognosis of carcinoma of the head and neck*. International Journal of Radiation Oncology*Biology*Physics, 1997. **38**(2): p. 285-289.
152. Dehdashti, F., P.W. Grigsby, M.A. Mintun, J.S. Lewis, B.A. Siegel, and M.J. Welch, *Assessing tumor hypoxia in cervical cancer by positron emission tomography with ⁶⁰Cu-ATSM: Relationship to therapeutic response--a preliminary report*. International Journal of Radiation Oncology*Biology*Physics, 2003. **55**(5): p. 1233-1238.
153. Haider, M.A., M. Milosevic, A. Fyles, I. Sitartchouk, I. Yeung, E. Henderson, G. Lockwood, T.Y. Lee, and T.P.L. Roberts, *Assessment of the tumor microenvironment in cervix cancer using dynamic contrast enhanced CT, interstitial fluid pressure and oxygen measurements*. International Journal of Radiation Oncology*Biology*Physics, 2005. **62**(4): p. 1100-1107.
154. Loncaster, J.A., B.M. Carrington, J.R. Sykes, A.P. Jones, S.M. Todd, R. Cooper, D.L. Buckley, S.E. Davidson, J.P. Logue, R.D. Hunter, and C.M.L. West, *Prediction of radiotherapy outcome using dynamic contrast enhanced MRI of carcinoma of the cervix*. International Journal of Radiation Oncology*Biology*Physics, 2002. **54**(3): p. 759-767.
155. Baudalet, C., G.O. Cron, and B. Gallez, *Determination of the maturity and functionality of tumor vasculature by MRI: Correlation between BOLD-MRI and DCE-MRI using P792 in experimental fibrosarcoma tumors*. Magnetic Resonance in Medicine, 2006. **56**(5): p. 1041-1049.
156. Winter, J.D., M. Estrada, and H.-L.M. Cheng, *Normal Tissue Quantitative T1 and T2* MRI Relaxation Time Responses to Hypercapnic and Hyperoxic Gases*. Academic Radiology, 2011. **18**(9): p. 1159-1167.
157. Lebon, V., P.G. Carlier, C. Brillault-Salvat, and A. Leroy-Willig, *Simultaneous measurement of perfusion and oxygenation changes using a multiple gradient-echo sequence: application to human muscle study*. Magnetic Resonance Imaging, 1998. **16**(7): p. 721-729.

158. Boss, A., P. Martirosian, M.C. Jehs, K. Dietz, M. Alber, C. Rossi, C.D. Claussen, and F. Schick, *Influence of oxygen and carbogen breathing on renal oxygenation measured by T2*-weighted imaging at 3.0T*. NMR in Biomedicine, 2009. **22**(6): p. 638-645.
159. Schwenger, N.F., P. Martirosian, J. Machann, C. Schraml, G. Steidle, C.D. Claussen, and F. Schick, *Aging effects on human calf muscle properties assessed by MRI at 3 Tesla*. Journal of Magnetic Resonance Imaging, 2009. **29**(6): p. 1346-1354.
160. Fyles, A., M. Milosevic, M. Pintilie, A. Syed, W. Levin, L. Manchul, and R.P. Hill, *Long-term performance of interstitial fluid pressure and hypoxia as prognostic factors in cervix cancer*. Radiotherapy and Oncology, 2006. **80**(2): p. 132-137.
161. Aquino-Parsons, C., A. Green, and A.I. Minchinton, *Oxygen tension in primary gynaecological tumours: the influence of carbon dioxide concentration*. Radiotherapy and Oncology, 2000. **57**(1): p. 45-51.
162. Powell, M.E.B., D.R. Collingridge, M.I. Saunders, P.J. Hoskin, S.A. Hill, and D.J. Chaplin, *Improvement in human tumour oxygenation with carbogen of varying carbon dioxide concentrations*. Radiotherapy and Oncology, 1999. **50**(2): p. 167-171.
163. Baddeley, H., P.M. Brodrick, N.J. Taylor, M.O. Abdelatti, L.C. Jordan, A.S. Vasudevan, H. Phillips, M.I. Saunders, and P.J. Hoskin, *Gas exchange parameters in radiotherapy patients during breathing of 2%, 3.5% and 5% carbogen gas mixtures*. British Journal of Radiology, 2000. **73**(874): p. 1100-4.
164. van der Sanden, B.P.J., A. Heerschap, L. Hoofd, A.W. Simonetti, K. Nicolay, A. van der Toorn, W.N.J.M. Colier, and A.J. van der Kogel, *Effect of carbogen breathing on the physiological profile of human glioma xenografts*. Magnetic Resonance in Medicine, 1999. **42**(3): p. 490-499.
165. d'Othée, B.J., G. Rachmuth, J. Munasinghe, and E.V. Lang, *The effect of hyperoxygenation on T1 relaxation time in vitro*. Academic Radiology, 2003. **10**(8): p. 854-860.
166. Kershaw, L.E., J.H. Naish, D.M. McGrath, J.C. Waterton, and G.J.M. Parker, *Measurement of arterial plasma oxygenation in dynamic oxygen-*

- enhanced MRI*. *Magnetic Resonance in Medicine*, 2010. **64**(6): p. 1838-1842.
167. Prisman, E., M. Slessarev, T. Azami, D. Nayot, M. Milosevic, and J. Fisher, *Modified oxygen mask to induce target levels of hyperoxia and hypercarbia during radiotherapy: A more effective alternative to carbogen*. *International Journal of Radiation Biology*, 2007. **83**(7): p. 457-462.
168. Mürtz, P., S. Flacke, A. Müller, M. Soehle, I. Wenningmann, A. Kovacs, F. Träber, W.A. Willinek, J. Gieseke, H.H. Schild, and S. Remmele, *Changes in the MR relaxation rate $R2^*$ induced by respiratory challenges at 3.0 T: a comparison of two quantification methods*. *NMR in Biomedicine*, 2010. **23**(9): p. 1053-1060.
169. Padhani, A.R. and K.A. Miles, *Multiparametric Imaging of Tumor Response to Therapy I*. *Radiology*, 2010. **256**(2): p. 348-364.
170. Kaanders, J.H.A.M., J. Bussink, and A.J. van der Kogel, *ARCON: a novel biology-based approach in radiotherapy*. *The Lancet Oncology*, 2002. **3**(12): p. 728-737.
171. Remmele, S., H. Dahnke, S. Flacke, M. Soehle, I. Wenningmann, A. Kovacs, F. Träber, A. Müller, W.A. Willinek, R. König, H. Clusmann, J. Gieseke, H.H. Schild, and P. Mürtz, *Quantification of the magnetic resonance signal response to dynamic (C)O₂-enhanced imaging in the brain at 3 T: R^*2 BOLD vs. balanced SSFP*. *Journal of Magnetic Resonance Imaging*, 2010. **31**(6): p. 1300-1310.